12-2020

Stability Analysis and Control of Nonlinear Power System Oscillations

Xin Xu
University of Tennessee, Knoxville, xxu30@vols.utk.edu

To the Graduate Council:

I am submitting herewith a dissertation written by Xin Xu entitled "Stability Analysis and Control of Nonlinear Power System Oscillations." I have examined the final electronic copy of this dissertation for form and content and recommend that it be accepted in partial fulfillment of the requirements for the degree of Doctor of Philosophy, with a major in Electrical Engineering.

Kai Sun, Major Professor

We have read this dissertation and recommend its acceptance:

Fangxing Li, Xiaopeng Zhao, Hector A. Pulgar

Accepted for the Council:

Dixie L. Thompson

Vice Provost and Dean of the Graduate School

(Original signatures are on file with official student records.)

Stability Analysis and Control of Nonlinear Power System Oscillations

A Dissertation Presented for the

Doctor of Philosophy

Degree

The University of Tennessee, Knoxville

Xin Xu

December 2020

ACKNOWLEDGEMENTS

I would like to thank Dr. Kai Sun for his excellent guidance in writing this dissertation and for his continuous encouragement, support and valuable discussions throughout my entire research at the University of Tennessee, Knoxville. Appreciation is also extended to the members of my Ph.D. committee, Dr. Fangxing Li, Dr. Xiaopeng Zhao, and Dr. Hector Pulgar, for their valuable discussions and suggestions.

I also appreciate the helpful discussions with fellow graduate students, Dr. Bin Wang, Dr. Nan Duan, Dr. Wenyun Ju, Dr. Yongli Zhu, Dr. Denis Osipov, Dr. Weihong Huang, Yang Liu, and Tianwei Xia, and visiting scholars, Dr. Yichen Guo and Dr. Guoqiang Zu, and postdoctoral researchers, Dr. Chengxi Liu, and Dr. Rui Yao.

I want to thank my family for their priceless patience and support during my graduate studies. Thank you, Shanshan, for being by my side on the Ph.D. journey.

At the end of my master's program, I summarized my creed to the academics by "Nothing is true. Everything is permitted". Now, at the end of my Ph.D. program, and also the start of the next career, I would like to add one more sentence:

Nothing is true. Everything is permitted. All are dynamic.

This work was supported in part by the National Science Foundation under Grant No. ECCS-1553863 and in part by the Engineering Research Center Program of the National Science Foundation and the Department of Energy under Grant No. EEC-1041877.

ABSTRACT

This work investigates the nonlinear oscillatory behaviors of multi-machine power systems. New model-based and measurement-based approaches are proposed for stability analysis and control of nonlinear oscillations.

For stability analysis, a recently proposed model-based nonlinear oscillation analysis method, nonlinear modal decoupling (NMD), is investigated on its ability in capturing the stability information of a multi-machine power system. From the differential-equation model of the power system, the NMD inversely constructs a set of 1-degree-of-freedom nonlinear oscillators, referred to as decoupled oscillators or subsystems, with each one corresponding to an oscillation mode of the original system. It is shown that retaining high order polynomial terms in the differential equation of each decoupled oscillator can make it more accurately represent the nonlinear modal dynamics and conditions of stability regarding the corresponding oscillation mode. For power system analysis, keeping the polynomial terms up to the 3^{rd}-order during the decoupling is acceptable for the purpose of approximating assessment for transient stability. A transient stability analysis approach is proposed to apply the NMD for early warning of transient instability caused by inter-area oscillations. This new approach simplifies the real-time monitoring of the whole power system to the monitoring of only a few critical modes by checking the dynamics of the corresponding decoupled oscillators and their stability boundaries. Thus, when a critical oscillation mode is going to evolve into a mode of instability, this approach can provide early warning to the power system operator.

For stability control, a direct damping feedback control method is proposed to control the damping ratio of a target dominant mode to closely follow a pre-set value by utilizing power converter-interfaced energy resources, e.g. battery-based energy storage devices. The direct damping feedback controller is designed to consist of a proportional-integral controller, a low-pass filter and a power system module that includes a reduced single-oscillator power system equivalent on the target oscillation mode and its measurement-based damping estimation algorithm. The parameters of the PI controller are optimized by considering the trade-off between the requirements of robustness and control performance. The power system module is represented by a transfer function based on the "zeroth-order" parametric resonance phenomenon. By identifying a nonlinear oscillator to fit dynamics of the target mode under both small and large disturbances, the measurement-based real-time damping estimation algorithm provides a feedback signal to the direct damping feedback controller. Numerical studies on the 48-machine Northeast Power Coordinating Council system validate the effectiveness of the proposed damping control method.

Keywords: Nonlinear oscillation, nonlinear modal decoupling, damping estimation, damping control, power systems.

TABLE OF CONTENTS

LIST OF TABLES

LIST OF FIGURES

CHAPTER 1

INTRODUCTION

1.1 Background and Motivation

Modern power systems are sometime operated close to their stability limits. Care must be taken in such operating conditions to avoid driving the system to cross any limit; otherwise, equipment failures or protective actions can be triggered to cause power outages or even a catastrophic blackout. In fact, a real-life event of power system instability is often developed from some critical oscillation modes. For instance, before the occurrence of the August 10, 1996 Western Interconnection Blackout, poorly-damped sustained oscillations around 0.26Hz were observed, which later triggered system protections and islanding of the interconnection and led to interruption of the electricity service with more than 7 million customers [1]. Similarly, in the August 14, 2003 Blackout, a lack of adequate real-time situational awareness resulted in inadequate reliability tools and backup capabilities and many oscillation events accelerated the spread of the blackout [2].

To this end, many tools have been proposed to signal an early warning of instability and provide mitigation strategies to the system operator. Numerical time-domain simulation on “what-if” scenarios is a widely-adopted approach by power industry for identification of potential transient instabilities, whose results are accurate but model- and contingency-dependent. On the other hand, finding an analytical solution, even approximately, for a high-dimensional nonlinear multi-oscillator system like a multi-machine power system has been a significant challenge [3]. When simulating a

large-scale power system having generators coupled through a complex network and interacting with each other nonlinearly, numerical methods can be very time-consuming in finding a qualitative stable or unstable judgment and may not provide much margin information, which is however critical for determining a control action [4].

Many high-performance computing approaches have been proposed to speed up power system transient stability simulation, but currently they are not yet ready for control room applications [5]. Hybrid approaches using both PMU measurements and system dynamical models to online monitor system dynamics and generate an early warning signal based on the information gathered online or prepared offline [6]-[10]. In addition, eigenvalues calculated from a linearized dynamical model were used to identify the potential cause of instability in real time [11]. Each inter-area oscillation model is associated with a cut set that partitions generators of the system into two oscillating groups, which can be told from the shape of the mode and might become out of step to lose transient stability under a large disturbance [12].

The nonlinear modal decoupling (NMD) method, which inherits the basic idea of the normal form theory, provides a new paradigm for stability analysis of multi-oscillator systems [13]. The traditional normal form methods try to generate a formally linear system of the original system by changing the coordinates of the state space [14], [15]. Comparatively, the NMD aims at a decoupled nonlinear system consisting of a desired number of independent 2^{nd}-order nonlinear oscillators, each of which is essentially a 1-degree-of-freedom (DOF) system, to approximate the dynamics of a given coupled complex multi-oscillator system. Each decoupled oscillator is corresponding to a

nonlinear oscillation mode about which the system dynamics are retained. Henceforth, the analysis on the original system is broken down into the analysis on individual, decoupled oscillators or nonlinear modes, which is much easier than the analysis on the original system. For instance, for a power grid connecting many generators, the modal dynamics with respect to different electromechanical modes may have relatively weak couplings or interferences unless significant resonances occur between some modes. Thus, the oscillators on modes are naturally decoupled in a certain space, and the NMD is applied to find the coordinate transformation from the original state space to such a new space, so that modal and stability analyses can be conducted more easily.

To make such implementation successful, it is necessary to verify the consistency between the stability analysis on the original system and on the decoupled system by the NMD. Under a small disturbance, i.e. when the system state slightly deviates from its stable equilibrium point (SEP) and the system's dynamic behavior is almost linear, it is natural to consider whether the decoupled system after an NMD transformation can generate the same trajectory from the given initial state as the original system, and NMD has been tested to be more accurate than normal form-based method in terms of assessment on transient stability of the original system [13]. However, under a large disturbance, especially when the system state is close to its stability boundary, i.e. the boundary of the region of attraction (ROA) of its SEP, and nonlinear dynamics become significant, the validity of NMD depends on the mathematical expression and its order used for the decoupled system. To determine if the state after a large disturbance is still within the ROA, it is crucial to accurately approximate its boundary or those unstable

equilibrium points (UEPs) on the boundary. Hence, the consistency between the ROAs from the original system and from the decoupled system by the NMD needs to be investigated to verify the validity of the NMD under large disturbances. Then, for the application in power systems, the dynamics of the original system subject to a large disturbance can be analyzed and visualized with respect to only a few selected critical modes through the NMD (note that only very few oscillation modes, e.g. mostly six or fewer, are obviously excited by any single contingency even for large-scale power systems [16]). If system operators have some knowledge on which modes the instability may be developed from, they can intentionally monitor the system dynamics on those critical modes and oscillating generators that participate in the modes and take preventive or remedial control actions to avoid instability.

Besides monitoring and early warning of system instability, an early control action can reduce the risk of loss of synchronism among the generators after disturbances. Real-time damping control is to improve the damping of a weakly-damped target mode. Without any control actions, a weakly-damped mode could easily induce instability under an additional disturbance.

Fast identification of a sustained oscillation from the measurement is a priori for the preventive control of oscillation-induced instability. The mainstream small-signal analysis methods for measurement-based modal analysis are based on linear system and signal processing theories by assuming a small disturbance, such as the widely-used Prony's method [17]. Thus, a measured system response can be decomposed into exponentially damped/undamped sinusoids with different phases, or equivalently

speaking, the main task is to identify eigenvalues and eigenvector-related properties of the target modes. Then, damping estimation is basically the calculation of eigenvalues of interests. One type of methods conducts analysis on ambient measurements caused by random small variations of the system, e.g. in loads. The main task is to extract oscillation modes from ambient noises in measurements. This can be done by reconstructing a linear system from the ambient data while mitigates the impact of the noise, like the autoregressive (AR) type model in [18], whose coefficients are solved by the recursive least square (RLS) type algorithm. Another type of methods, e.g. Prony's method [17], [19], the Eigenvalue realization algorithm [20], and Matrix Pencil method [21], can analyze ring-down measurements following a disturbance such as a line or generator trip. They find the best fitting into the measurements of a window by a sum of sinusoids or by a response from a reconstructed equivalent linear system. Some methods perform time-frequency analysis using the Fourier transform or continuous wavelet transform for better damping estimation [22], [23].

However, the assumption of linear system does not always hold true for the damping estimation of a dominant inter-area mode using ring-down measurements following a fault. A real-life fault can hardly be treated as a small disturbance especially for areas not too far from the fault location. If the fault excites any critical oscillation mode, nonlinear waveforms often manifest in power system measurements. Thus, in this case, damping estimation using the linear analysis based methods like the Prony's method are often unreliable, since during the early transient period the damping estimation results can be sensitive to the length and starting point of the time window as

illustrated by Figure 1. A measure commonly used by many commercialized modal analysis tools is to ignore the first several or several tens of seconds of the ring-down portion containing transient measurements until the system response recovers to be close enough to a linear system response. This handling may discard important information on potential angular instability. Under some conditions, available measurements are too limited, e.g. capturing only first few swings for the critical mode, to afford the discarding of any data. Thus, there is a need for a robust damping estimation tool that is applicable to large-amplitude swings and insensitive to the length and starting point of the measuring window.

Some modal analysis methods have tried to accommodate some nonlinear dynamics. One representative is the Hilbert-Huang transformation (HHT) method [24], in which each mode is interpreted as a sinusoidal signal with time-varying parameters, i.e. a mode with changing frequency and damping. It first extracts so-called intrinsic mode functions (IMF) from measurements by empirical mode decomposition. Each IMF is expected to represent one oscillation mode and interpreted by HHT to estimate time-varying modal parameters. However, these methods are still on the basis of linear system theory and interpret an oscillation mode as a damped/undamped sinusoidal function with time-varying parameters. The resulting damping estimation is still sensitive to the length and starting point of the measuring window.

Recently, some recent studies on understanding and formulation of nonlinear electromechanical oscillations discover that the frequency of an oscillation mode decays with the amplitude of oscillation [25], [26] according an “F-A curve”. Furthermore,

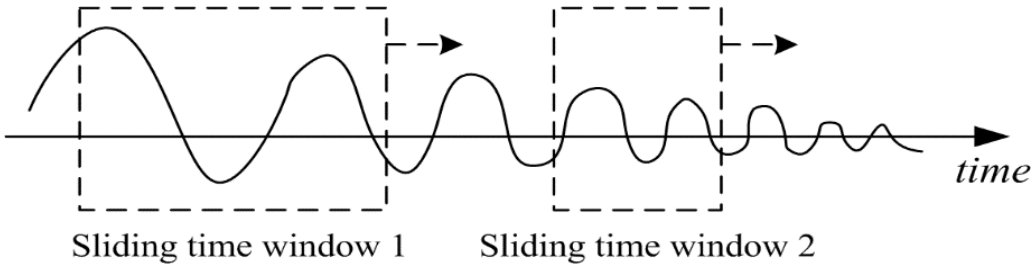

Figure 1. Schematic diagram of sliding time window.

according to the NMD method, the nonlinear dynamics of a multi-machine system in an extended neighborhood of the equilibrium can be decomposed into dynamics of as many fictitious nonlinear oscillators of 1-DOF as its oscillation modes. Thus, the dynamics and stability of the original system regarding each mode can be studied using the corresponding 1-DOF oscillator. Hence, for more robust estimation of oscillation damping, it is worthwhile to incorporate the idea of NMD, i.e. interpreting each mode as a nonlinear oscillator, into the estimation method such that the post-disturbance measurements can be taken full use of and the result is insensitive to the length and starting point of measuring window.

An advanced design of damping controller relies on not only fast damping estimation, but also the ability of fast electrical power control which can directly impact the damping torque on the generator rotors. In this sense, the increasing use of power converter based devices could enable new ways for fast damping control. Power converter interfaces the distributed energy resources (DERs) to the power grid, and thus, serves an important role in the increasing penetration of the DERs. Since the dynamics of the power electronics devices are much faster than the dynamics of the electromechanical oscillations in a conventional synchronous generator based grid, power converters could serve as a promising measure for direct and fast power flow control as well as damping control. Typical power converter based devices include flexible AC transmission system (FACTS) devices [27]-[29], wind generators [30], [31], solar plant [32], [33], battery energy storage system (BESS) [34], etc.

Many researches activities have investigated the use of power converter based devices for damping control due to its flexibility and fastness. [35] and [36] consider BESS for controlling damping ratio. The configuration of the BESS is set to bring the damping ratio back to an expected value. [37] considers the superconducting magnetic energy storage and design a close-loop control system to tune the eigenvalues of the target modes. [38] uses a two-machine system to investigates the impact of the voltage-source-converters in terms of location and real/reactive power modulation. [39] proposed a particle swarm optimization based and a heuristic dynamic programming based methods to adaptively control the energy storage devices in order to stabilize the oscillation between two interconnected power systems.

Most of the existing methods aim at increasing the damping for a target mode to stabilize the oscillation. An off-line model representing a typical scenario is commonly used for configuring the structure and the parameters of the controller, and then, the designed controller is implemented online without much modification considering the model inaccuracy or model change. Consequently, the effectiveness of the controller would be subject to the model inaccuracy and model change. The controller could perform as expected when a practical scenario is close to the offline model, but the effectiveness would be in doubt under a different scenario. For instance, if we set the damping ratio of the target mode to be 3% as the expected value, it could be difficult for the controller to reach the expected value when the system undergoes a permanent change like line trip, and the controller might be less effective if no additional modification is taken. On the other hand, with fast and accurate damping estimation

method and fast power control ability of power converters, it could be possible to directly design a feedback control system to eliminate the damping ratio deviation of a target mode by using the measured damping ratio as a feedback and controlling the power converters accordingly. Such a feedback control method would be more robust against any model change.

1.2 Contributions of This Work

This work proposes new stability monitoring approach and new damping control method considering the nonlinear electromechanical oscillations in multi-machine power systems, including an NMD based power system transient stability analysis (TSA) approach and a direct damping feedback control method. A real-time damping estimation on nonlinear electromechanical oscillation is also proposed for the purpose of damping control. Specifically, the contributions can be categorized into the following several aspects:

- This work analyzes the nonlinear characteristics of electromechanical oscillations in power systems, understanding which will be valuable for designing a more accurate damping estimation algorithm and more effective grid stabilization control methods against both small and large disturbances.

- This work compares the transient stability analysis results on the original system and the decoupled system from the NMD. It is shown that transient stability analysis on a decoupled system that has higher order polynomial terms truncated in its model may introduce errors compared

to the analysis on the original system. It is also shown that keeping the polynomial terms up to the 3rd-order for the decoupled system is acceptable for the purpose of approximate or conservative transient stability analysis.

- This work establishes an NMD based power system TSA approach for large-scale power system. The analysis of the original high-dimensional system can be reduced to individual analyses on decoupled nonlinear oscillators about a few selected critical modes. The most critical mode that could induce instability can be identified by comparing the state and stability boundary of the decoupled oscillator regarding that mode.

- This work proposes an approach for real-time damping estimation on nonlinear electromechanical oscillation energized by a large disturbance. By identifying a nonlinear oscillator to fit the measurements on the dominant mode of oscillation, the proposed damping estimation approach can utilize complete post-disturbance data including the data during the transient period. Its robustness is verified from its independence from the length and starting point of the measuring window.

- This work develops a method to approximate the power system model together with the damping estimation algorithm by a transfer function. This approximation is enabled by *a*) representing the target mode as a single oscillator model, which is obtained from model reduction via the

NMD method, and *b*) considering the parametric resonance of the single oscillator model.

- This work proposes a direct damping feedback control method to eliminate the damping ratio deviation for a target mode by controlling the power converters based devices in the system. The parameters of the PI controller are determined by considering the trade-off between robustness and control performance.

CHAPTER 2

STABILITY ANALYSIS ON NONLINEAR OSCILLATIONS

In this chapter, the NMD method is investigated on its ability in capturing the stability information of the power system, and new NMD based power system TSA approach is proposed afterwards. It is shown that the decoupled oscillator obtained from NMD can retain higher order polynomial terms in the differential equations and can more accurately represent the nonlinear modal dynamics and conditions of stability regarding the corresponding oscillation mode. Then, it is shown that for power system analysis, keeping the polynomial terms up to the 3rd-order during the decoupling is acceptable for the purpose of approximating assessment for transient stability. Finally, a TSA approach is proposed to apply the NMD to the early warning of instability, which reduces the monitoring of the whole power systems to only a few critical modes and can indicate the most critical one that could induce instability.

2.1 Introduction of Nonlinear Modal Decoupling

The basic idea of NMD is described as follows [13]. A multi-oscillator system is given by a set of ordinary differential equations (ODEs)

$$\dot{\mathbf{X}} = \mathbf{f}(\mathbf{X}), \mathbf{X} \in \mathbb{R}^N \tag{1-1}$$

where $\mathbf{X}$ is the state vector and $\mathbf{f}$ governs the system dynamics. Without loss of generality, assume its SEP at the origin and apply Taylor expansion (TE):

$$\dot{\mathbf{X}} = \mathbf{A}_1\mathbf{X} + \sum_{j=2}^{\infty} \mathbf{A}_j \mathbf{X}^{[j]} \tag{1-2}$$

The *k*-jet system of (1-1) is defined as (1-3) that only keeps the terms up to order *k* having higher-order terms truncated.

$$\dot{\mathbf{X}} = \mathbf{A}_1\mathbf{X} + \sum_{j=2}^{k} \mathbf{A}_j \mathbf{X}^{[j]} \tag{1-3}$$

where $\mathbf{X}^{[j]}$ is a Kronecker product form, denoting all the *j*th-order homogenous polynomial components of the vector **X**. $\mathbf{A}_j \in \mathbb{R}^{N^j \times 1}$ is the coefficient matrix. *k* determines the accuracy of (1-3) to approximate (1-1). Usually a larger *k* is preferred if a higher accuracy is needed.

A *k*th-order NMD transformation (*k*-NMDT) denoted by **H** decouples *k*-jet (1-3) into independent oscillators of 1-DOF, and it is essentially a set of polynomial functions of the state vector **Z** on the decoupled system:

$$\mathbf{X} = \mathbf{H}(\mathbf{Z}) = \mathbf{B}_1\mathbf{Z} + \sum_{j=1}^{k} \mathbf{B}_j \mathbf{Z}^{[j]}, \mathbf{Z} \in \mathbb{R}^N \tag{1-4}$$

where $\mathbf{B}_j \in \mathbb{R}^{N^j \times 1}$ is the coefficient matrix.

To obtain decoupled nonlinear oscillators, NMD first substitutes (1-4) into *k*-jet (1-3), and then, re-group the state variables of **Z** into pairs as below, with each representing the two state variables (corresponding to the position and velocity) associated with one oscillator.

$$\mathbf{Z} = \left[\mathbf{z}_1^T, \mathbf{z}_2^T, \cdots\right]^T \quad \text{where } \mathbf{z}_i = \left[z_{i1}, z_{i2}\right]^T \tag{1-5}$$

$$\dot{\mathbf{Z}} = \mathbf{G}(\mathbf{Z}) + \mathbf{R}(\mathbf{Z}) \Leftrightarrow \begin{bmatrix} \dot{\mathbf{z}}_1 \\ \dot{\mathbf{z}}_2 \\ \vdots \end{bmatrix} = \begin{bmatrix} \mathbf{g}_1(\mathbf{z}_1) \\ \mathbf{g}_2(\mathbf{z}_2) \\ \vdots \end{bmatrix} + \begin{bmatrix} \mathbf{r}_1(\mathbf{Z}) \\ \mathbf{r}_2(\mathbf{Z}) \\ \vdots \end{bmatrix} \tag{1-6}$$

$$\dot{\mathbf{z}}_i = \mathbf{g}_i\left(\mathbf{z}_i\right) + \mathbf{r}_i\left(\mathbf{Z}\right) \Leftrightarrow \begin{bmatrix} z_{i1} \\ z_{i2} \end{bmatrix} = \begin{bmatrix} g_{i1}\left(z_{i1}, z_{i2}\right) \\ g_{i2}\left(z_{i1}, z_{i2}\right) \end{bmatrix} + \begin{bmatrix} r_{i1}\left(\mathbf{Z}\right) \\ r_{i2}\left(\mathbf{Z}\right) \end{bmatrix} \tag{1-7}$$

Thus, system (1-1) is transformed into (1-6), defined as the transformed system (TS) with each oscillator expressed by (1-7), where $\mathbf{g}_i(\mathbf{z}_i)$ only includes the polynomial terms up to order k and $\mathbf{r}_i(\mathbf{Z})$ includes all terms higher than order k.

Remarks

(a) If a polynomial term in the ith oscillator only consists of $\mathbf{z}_i$, it is called an intra-modal term, i.e. only depending on the state variables about this mode (oscillator); otherwise it is called an inter-modal term, which also involves state variables about other modes (oscillators). Note that $\mathbf{g}_i(\mathbf{z}_i)$ only contains intra-modal terms, while $\mathbf{r}_i(\mathbf{Z})$ can contain both intra-modal terms and inter-modal terms.

(b) After substitution, the TS may still be coupled; that is, the inter-modal terms greater than order k could exist, i.e. the existence of $\mathbf{R}(\mathbf{Z})$. This indicates that a k-NMDT can only decouple the terms up to order k while other terms greater than order k could still have inter-modal terms. ■

By truncating $\mathbf{R}(\mathbf{Z})$ in TS, we obtain the k-jet decoupled system (k-DS) (1-8) with a set of independent oscillators each having only intra-modal terms as expressed by (1-9):

$$\dot{\mathbf{Z}} = \mathbf{g}\left(\mathbf{Z}\right) \tag{1-8}$$

$$\dot{\mathbf{z}}_i = \mathbf{g}_i\left(\mathbf{z}_i\right) = \begin{bmatrix} g_{i1}\left(z_{i1}, z_{i2}\right) \\ g_{i2}\left(z_{i1}, z_{i2}\right) \end{bmatrix} = \mathbf{\Lambda}_i \mathbf{z}_i + \sum_{j=2}^{k} \mathbf{D}_{ij} \mathbf{z}_i^{[j]} \tag{1-9}$$

where $\mathbf{\Lambda}_i \in \mathbb{R}^{2\times 2}$ is a diagonal matrix and $\mathbf{D}_{ij} \in \mathbb{R}^{2^j \times 1}$ is a coefficient matrix.

While **X** is the state vector, we treat **Z** as the modal vector, since each oscillator represents a nonlinear mode that is only related to $\mathbf{z}_i$ after the decomposition. The NMD procedure is illustrated in Figure 2, from which two factors may introduce errors in deriving *k*-DS: *a)* the truncation between TE and *k*-jet, and *b)* the truncation between TS and *k*-DS.

Remarks

(a) Ref. [13] suggests inversely constructing the decoupled system by first assigning polynomial formation (1-9) to each oscillator with the coefficients undetermined, and then deriving the transformation (1-4) and the coefficients in (1-9). Note that the polynomial form is not the only choice and other forms may be applied to each oscillator.

(b) After the decomposition, the modal dynamics of the original coupled system are decoupled into dynamics of oscillators (9). It provides a possibility to analyze stability of the original system based on stabilities of some of crucial oscillators so as to reduce the dimension of the system model and simplify angular stability analysis. ■

The two truncations, *a)* the truncation between TE and *k*-jet and *b)* the truncation between TS and *k*-DS, would lead to the difference between the original system and decoupled system, like the stability information. For instance, the truncations would lead to the difference in their equilibrium points (EPs), which is explained as follows.

The set of the EPs of the original system is denoted by

$$\mathbf{EX} = \left\{ \mathbf{X} \in \mathbb{R}^{2N} : \mathbf{f}\left(\mathbf{X}\right) = 0 \right\} \tag{1-10}$$

The set of the EPs of the *k*-jet system is denoted by

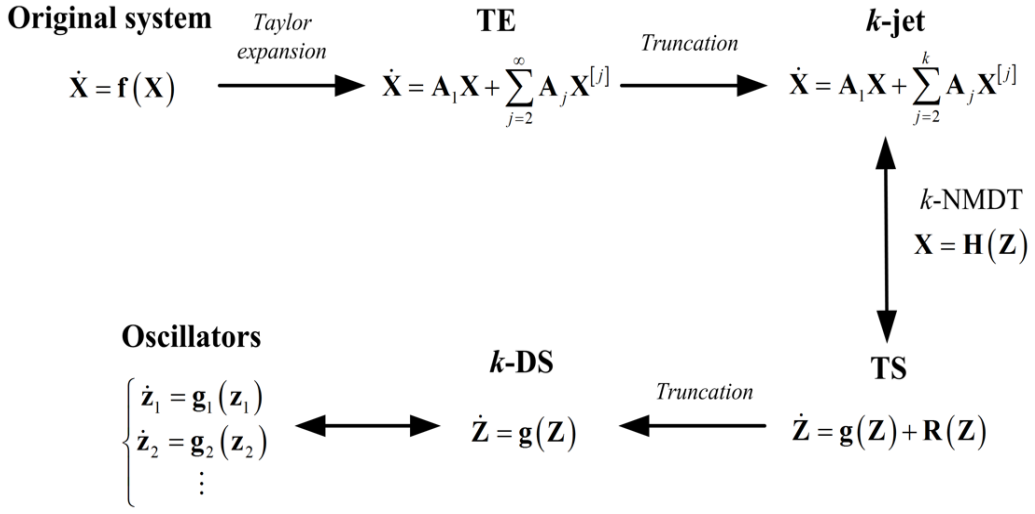

Figure 2. NMD procedure and the relation of different systems.

$$\mathbf{EX}_{k-jet} = \left\{ \mathbf{X} \in \mathbb{R}^{2N} : \mathbf{A}_1 \mathbf{X} + \sum_{i=2}^{k} \mathbf{A}_i \mathbf{X}^{[i]} = 0 \right\} \tag{1-11}$$

The set of the EPs of the decoupled system, which is obtained by truncating the **R**(**Z**) of the TS system, is denoted by

$$\mathbf{EZ}_{DS} = \left\{ \mathbf{Z} \in \mathbb{R}^{2N} : \mathbf{g}(\mathbf{Z}) = 0 \right\} \tag{1-12}$$

The set of the EPs of *i*th oscillator is denoted by

$$\mathbf{EZ}_{Osc,i} = \left\{ \mathbf{z}_i \in \mathbb{R}^{2} : \mathbf{g}(\mathbf{z}_i) = 0 \right\} \tag{1-13}$$

$\mathbf{EZ}_{DS}$ can also be expressed as the Cartesian product of $\mathbf{EZ}_{Osc,i}$:

$$\mathbf{EZ}_{DS} = \mathbf{EZ}_{Osc,1} \times \cdots \times \mathbf{EZ}_{Osc,N} \tag{1-14}$$

The relation between these EPs sets are listed below.

i) The EPs in **EX** can be approximated by the EPs in $\mathbf{EX}_{k\text{-}jet}$. The inaccuracy is caused by the truncation of the high-order terms in Taylor expansion.

ii) $\mathbf{EX}_{k\text{-}jet}$ can be approximated by $\mathbf{EX}_{appro} = \mathbf{H}(\mathbf{EZ}_{DS})$. The inaccuracy is caused by the truncation of **R**(**Z**) in (1-6).

iii) The SEP in **EX**, $\mathbf{EX}_{k\text{-}jet}$, and $\mathbf{EX}_{appro}$ are identical.

The relationships between these systems are re-organized in Figure 3 for better understanding. The solid line means the two EP sets are identical, while dashed line means they approximate each other. It shows that the two truncations lead to the inconsistency between **EX** and $\mathbf{H}(\mathbf{EZ}_{DS})$.

2.2 Stability Comparison of the Original System and Decoupled System

The two truncations of higher order polynomial terms, i.e. *a)* the truncation between TE and *k*-jet, and *b)* the truncation between TS and *k*-DS, would lead to the

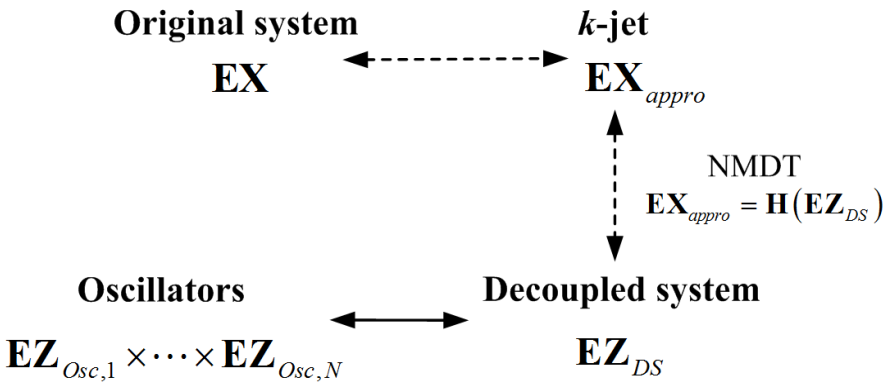

Figure 3. The relationships between different systems in terms of EPs.

inconsistency of the stability information between the original system and the decoupled system. In this section, it is first investigated which order of *k*-jet can be selected for power system stability analysis. Then, numerical studies are made on the IEEE 9-bus system for the stability comparison of the original system and decoupled system in terms of the approximation of the stability boundary and closest UEP.

Since the IEEE 9-bus system will be frequently used for the numerical studies in the following subsection, its information is given here. The rest subsection will use this model unless specifically explained. The one-line-diagram of the IEEE 9-bus system is shown in Figure 4, and the other parameters can be found in [26].

The system is modeled as an *m*-machine power system modeled by (1-15), which has generators in the classic model, loads modeled as impedances, and network losses considered.

$$\begin{cases} \dot{\delta}_i = \Delta\omega_i, \\ \Delta\dot{\omega}_i = \dfrac{\omega_R}{M_i}\left(P_{mi} - P_{ei} - D_i \dfrac{\Delta\omega_i}{\omega_R} \right), \end{cases} \quad i = 1, 2, \cdots, m \tag{1-15}$$

$$P_{ei} = \sum_{j=1}^{N} E_i E_j \left[G_{ij} \cos\left(\delta_i - \delta_j\right) + B_{ij} \sin\left(\delta_i - \delta_j\right) \right] \tag{1-16}$$

where δ_i, $\Delta\omega_i$, $P_{\mathrm{m}i}$, $P_{\mathrm{e}i}$, E_i, M_i and D_i represent the absolute rotor angle, speed deviation, mechanical power, electrical power, electromotive force, the inertias and damping coefficients of machine i, respectively. ω_R is a constant for synchronous speed [40]. G_{ij} and B_{ij} represent the conductance and susceptance, respectively. The system state **X** is organized as:

$$\mathbf{x} = \begin{pmatrix} \delta_1 & \Delta\omega_1 & \delta_2 & \Delta\omega_2 & \cdots & \delta_m & \Delta\omega_m \end{pmatrix}^{\mathrm{T}} \tag{1-17}$$

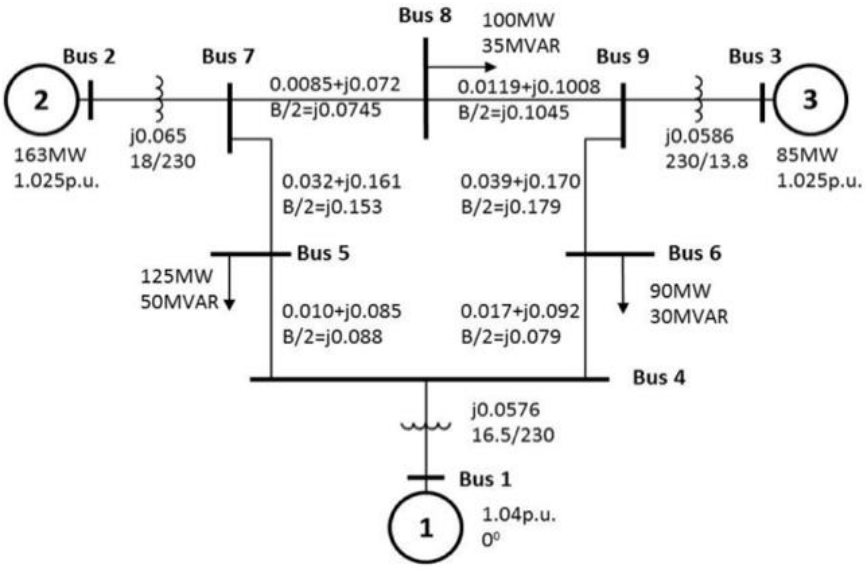

Figure 4. Diagram of IEEE 3-machine 9-bus system [26].

2.2.1 Truncated Taylor Expansion of the Original System

The *k*-jet system (*k*-jet) and *k*-jet decoupled system (*k*-DS) can be generalized by the definition of the truncated Taylor expansion: given the TE of (1-1) at the SEP, keeping only the first *n* terms gives an approximate system, called the *n*th order TTE system, or the TTE system at order *n*. *k*-jet and *k*-DS are essentially *k*th order TTE systems.

For the single-machine-infinite-bus (SMIB) system, it has been shown that the 3^{rd}, 4^{th}, 7^{th}, and 8^{th} orders TTE always give conservative stability analysis results. Moreover, the result from the 3^{rd} order TTE is most conservative. The proofs and technical details can be found in [41].

For the case of multi-machine power systems, to explore the capability of analytical approaches starting from TTE systems and without involving systematic errors, the transient stability is assessed by time domain simulations. A stability boundary searching algorithm is proposed to determine the stability boundaries of the original system and its TTE systems, whose comparison can show how accurately the TTE systems can be used to assess the transient stability of multi-machine power systems.

The stability boundaries of the original system and its TEE systems are searched by the algorithm below. Different parts of the stability boundary are acquired by applying sustained disturbances in different directions in the state space. In this paper, the random number generation function “rand” in Matlab is used to create a number of unit vectors to represents disturbances in different directions.

START

1 Let $k = 1$ and $l = l_0$, $s = s_0$.
2 Given a unit vector $\boldsymbol{n}$ in the state space representing the disturbance in a specific direction.
3 Initialize the system at $\mathbf{X}(t=0) = \mathbf{X}_{SEP} + l \cdot \boldsymbol{n}$ and simulate the system for a certain time T.
4 **if** $|\delta_i(t=T) - \delta_j(t=T)| < \Delta$ for any i and j in $\{1, 2, \ldots, m\}$
| **if** $s < \varepsilon$
| | ($\mathbf{X}_{SEP} + l_k \cdot \boldsymbol{n}$) is on the boundary. **Return**.
| **else**
| | $l = l + s$.
| **end**
else
| $s = s/2$ and $l = l - s$.
end
5 **go to 3**

Two systems are selected for numerical studies, IEEE 9-bus power system and WECC 179-bus system.

On the IEEE 9-bus system, the number of all (N-1) line tripping contingencies is 12, which are shown in Table 1. The critical clearing time (CCT) from the TTE systems are searched by a number of simulation runs and their normalized values by the true CCTs from Table 1 are shown in Table 2. Then, the generations are re-dispatched by increasing P_{m2} from 163MW to 200MW, P_{m3} from 85MW to 100MW and decreasing P_{m1} from 71.61MW to 22.55MW. Such modification will push the system closer to its steady state angle stability limit due to the increase of the power transfer from generators 2 and 3 to generator 1. It should be mentioned that after the re-dispatch, the CCT of each contingency is more or less reduced compared to their counterparts in Table 1. In this case, the normalized CCTs of TTE systems are shown in Table 3. The comparison between Table 3 and Table 2 indicates that the errors in the CCTs of TTE systems decrease if the system is closer to its steady state angle stability limit as expected from

Table 1. (N-1) Line Tripping Contingencies and Their CCTs

Cont. #	Fault bus	Tripped line	CCT /s	Cont. #	Fault bus	Tripped line	CCT /s
1	4	4-6	0.329	7	7	5-7	0.179
2	4	4-5	0.338	8	7	7-8	0.195
3	5	4-5	0.441	9	8	7-8	0.297
4	5	5-7	0.353	10	8	8-9	0.325
5	6	4-6	0.493	11	9	6-9	0.231
6	6	6-9	0.430	12	9	8-9	0.249

Table 2. Normalized CCTs of TTE Systems in 9-Bus System

#	TTE2	TTE3	TTE4	TTE5	TTE6	TTE7	TTE8	TTE9
1	1.817	0.895	0.935	2.446	1.016	0.998	0.999	1.000
2	1.806	0.885	0.929	2.351	1.287	0.997	0.999	1.000
3	1.717	0.857	0.911	∞*	∞	0.996	0.998	1.000
4	1.282	0.904	0.973	1.014	1.002	0.999	1.000	1.000
5	1.623	0.859	0.910	∞	1.024	0.996	0.998	1.000
6	1.373	0.892	0.960	1.020	1.004	0.999	1.000	1.000
7	1.276	0.908	0.974	1.013	1.002	0.999	1.000	1.000
8	1.347	0.911	0.969	1.015	1.003	0.999	1.000	1.000
9	1.380	0.895	0.959	1.023	1.005	0.999	1.000	1.000
10	1.602	0.870	0.929	2.361	1.016	0.997	0.999	1.000
11	1.358	0.904	0.964	1.019	1.004	0.999	1.000	1.000
12	1.776	0.887	0.930	2.345	1.061	0.997	0.999	1.000

* In each of these cases, the CCT is larger than 1 second.

Table 3. Normalized CCTs if TTE Systems in 9-Bus System after Generation Re-Dispatch

#	TTE2	TTE3	TTE4	TTE5	TTE6	TTE7	TTE8	TTE9
1	1.409	0.907	0.964	1.018	1.004	0.999	1.000	1.000
2	1.344	0.897	0.963	1.024	1.007	0.999	1.000	1.000
3	1.388	0.887	0.959	1.025	1.005	0.999	1.000	1.000
4	1.894	0.592	0.941	1.030	1.001	0.999	0.999	0.999
5	1.430	0.894	0.958	1.021	1.005	0.999	1.000	1.000
6	1.173	0.929	0.989	1.004	1.000	1.000	1.000	1.000
7	1.854	0.577	0.942	1.027	0.999	0.997	0.998	0.998
8	1.206	0.923	0.985	1.006	1.001	1.000	1.000	1.000
9	1.222	0.919	0.983	1.007	1.001	1.000	1.000	1.000
10	1.387	0.894	0.962	1.020	1.004	0.999	1.000	1.000
11	1.176	0.926	0.989	1.005	1.001	1.000	1.000	1.000
12	1.521	0.887	0.943	1.151	1.012	0.998	0.999	1.000

the observation on SMIB systems.

Table 2 shows that the CCTs determined by TTE systems at orders 2, 5, 6 and 9 are larger than the true CCT, while the CCTs from TTE systems at orders 3, 4, 7 and 8 are always smaller. In addition, the degree of optimism/conservativeness, i.e. the error in CCT, decreases when the TE order increases.

The last test on IEEE 9-bus system summarizes the TTE based TSA using 1000 randomly generated directions in the state space under the default loading condition without any topology changes. The distributions of the normalized stability boundaries of TTE systems are shown in Figure 5, which basically verifies the conclusions from SMIB power systems. Specifically, 2^{nd}, 6^{th} and 9^{th} order TTE systems generally give the stability boundaries respectively 0.7-2.5, 0.66-3, 1-1.005 times larger compared to the true boundaries, while the 5^{th} order is about 1-5 times larger including a few cases where no instability can be detected. The stability boundaries from 3^{rd}, 4^{th}, 7^{th} and 8^{th} order TTE systems are respectively about 0.52-0.88, 0.51-0.96, 0.98-0.999 and 0.99-1 times the true boundaries.

Next, the 179-bus 29-generator simplified WECC power system model is used to test the accuracy of TTEs on top-8 most critical line-tripping contingencies near the California-Oregon intertie [41]. The results shown in Table 4 also roughly validate the conclusions on SMIB systems. According to the comparison between Table 2 and Table 3, the good accuracy in results Table 4 from the 4th order and above indicates that the original system is close to its steady state angle stability limit along the California-Oregon intertie.

Table 4. Normalized CCTs of TTE Systems in 179-Bus System

#	TTE2	TTE3	TTE4	TTE5	TTE6	TTE7	TTE8	TTE9
1	1.144	0.885	0.996	1.017	1.000	0.999	1.000	1.000
2	1.144	0.886	0.995	1.017	1.000	0.999	1.000	1.000
3	1.104	0.895	1.000	1.014	1.000	0.999	1.000	1.000
4	1.105	0.894	1.000	1.015	1.000	0.999	1.000	1.000
5	1.085	0.917	0.996	1.009	1.000	1.000	1.000	0.999
6	1.086	0.916	0.996	1.009	1.000	1.000	1.000	1.000
7	1.116	0.893	1.040	1.015	1.000	0.999	1.000	1.000
8	1.119	0.893	1.041	1.015	1.000	0.999	1.000	1.000

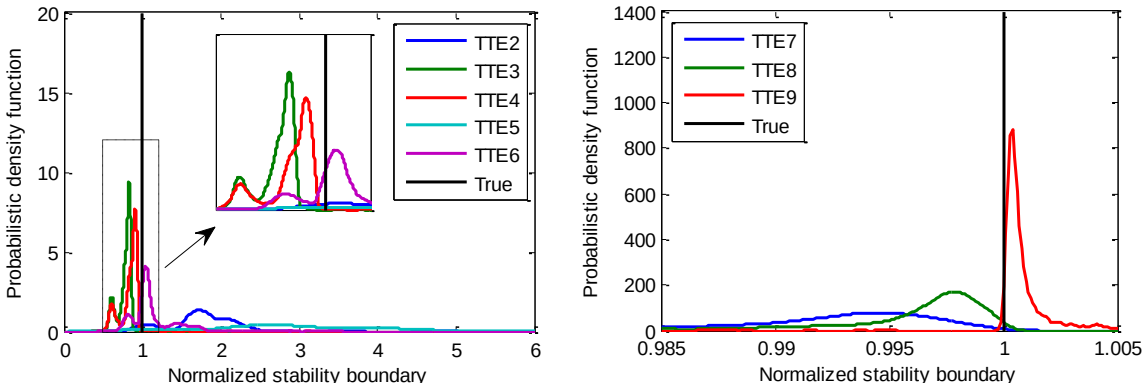

Figure 5. Distributions of normalized stability boundaries of TTE systems of IEEE 9-bus power system in 1000 different directions in the state space.

Based on all the analysis above, it is concluded that TTE systems at orders 2, 5, 6 and 9 give optimistic TSA results while those at orders 3, 4, 7 and 8 give conservative results.

Henceforth, we select 3rd order TTE system for the following analysis in this chapter for two reasons. First, in terms of stability analysis, it is important to ensure that the stability boundary of *k*-jet system should be consistent with, or conservative when compared to, the boundary of the original system. Moreover, a lower order TTE would reduce the computation burden.

2.2.2 Approximation of the Stability Boundary

This section investigated the stability boundary, which is usually referred to as region-of-attraction (ROA) boundary in the field of control, for the original system, *k*-jet, and *k*-DS. The ROA of interests is assumed to be compact and connected. Time domain simulation is used to verify if a given initial state leads to the SEP. The boundary search algorithms are proposed to determine the stability boundaries of the original system, *k*-jet, and *k*-DS, whose comparison can show the consistency between the boundaries from those systems.

The algorithm estimates the stability boundaries of the original system and its *k*-jet is the same as one used in the section 2.2.1. The algorithm finding the boundary of *k*-DS (8) is given below, which is similar to the previous one but with some modifications. To compare the stability boundary of *k*-DS with that of the original system or *k*-jet, the perturbations in different directions are applied to system state **X**. The initial state on any direction, say $\mathbf{X}(t=0)$, is first transformed to the modal vector **Z** via *k*-NMDT, i.e., $\mathbf{Z} = \mathbf{H}^{-}$

$^{1}(\mathbf{X}(t=0))$, and then simulated using k-DS. There are many ways to solve the NMDT, e.g. by applying the Newton-Raphson method to equation $\mathbf{H}(\mathbf{Z})–\mathbf{X}(t=0) = 0$.

START

1 Let $k = 1$ and $l = l_0$, $s = s_0$.

2 Given a unit vector $\boldsymbol{n}$ in the state space representing a specific perturbation direction in the state space.

3 Initialize the system at $\mathbf{X}(t=0) = \mathbf{X}_{SEP} + l \cdot \boldsymbol{n}$, and simulate k-DS from $\mathbf{Z} = \mathbf{H}^{-1}(\mathbf{X}(t=0))$ for certain time T.

4 **if** $|z_i(t=T) - z_j(t=T)| < \Delta$ for any i and j in $\{1, 2, \ldots, m\}$
| **if** $s < \varepsilon$
| | ($\mathbf{x}_{ep} + l_k \cdot \boldsymbol{n}$) is on the boundary. **Return**.
| **else**
| | $l = l + s$.
| **end**
else
| $s = s/2$ and $l = l - s$.
End

5 **go to 3**

The numerical studies of the proposed NMD-based stability boundary estimation is applied on the IEEE 3-machine 9-bus system. First, the expression of the original system, 3-jet and 3-DS are given, with all the states denoted by:

$$\mathbf{X} = [\delta_1, \Delta\omega_1, \delta_2, \Delta\omega_2, \delta_3, \Delta\omega_3]^T = [x_1, x_2, x_3, x_4, x_5, x_6]^T \quad (1\text{-}18)$$

Each pair $[\delta_i, \Delta\omega_i]$ represents the state variables for machine i. The original power system model is (1-19). The corresponding 3-jet is expressed by (1-20). Note that in (1-20), the coordinates are transformed to make SEP $\mathbf{x}_{SEP} = 0$. After applying the NMD with the small transfer assumption, the 3-DS is derived consisting of two oscillators expressed by (1-21). Note that in (1-21), the former two ODEs related to z_1 and z_2 are referred to as mode 1, while the rest two ODEs related to z_3 and z_4 are referred to as mode 2.

$$\begin{cases} \dot{x}_1 = x_2 \\ \dot{x}_2 = -0.5x_2 + 13.4\sin(x_{31} + 0.305) - 2.54\cos(x_{31} + 0.305) \\ \quad -1.8\cos(x_{51} + 0.19) + 10.5\sin(x_{51} + 0.19) - 1.81 \\ \dot{x}_3 = x_4 \\ \dot{x}_4 = -0.5x_4 - 2.35\cos(x_{31} + 0.305) - 12.4\sin(x_{31} + 0.305) \\ \quad -1.68\cos(x_{35} + 0.115) - 8.56\sin(x_{35} + 0.115) + 8.59 \\ \dot{x}_5 = x_6 \\ \dot{x}_6 = -0.5x_6 + 20.8\sin(x_{35} + 0.115) - 4.03\cos(x_{51} + 0.19) \\ \quad -23.6\sin(x_{51} + 0.19) - 4.08\cos(x_{35} + 0.115) + 10.1 \end{cases} \tag{1-19}$$

where $x_{ij} = x_i - x_j$

$$\begin{cases} \dot{x}_1 = x_2 \\ \dot{x}_2 = -24.2x_1 - 0.5x_2 + 13.5x_3 + 10.7x_5 - 0.907x_1^2 + 1.59x_1x_3 \\ \quad +0.221x_1x_5 - 0.797x_3^2 - 0.111x_5^2 + 4.03x_1^3 - 6.77x_1^2x_3 \\ \quad -5.33x_1^2x_5 + 6.77x_1x_3^2 + 5.33x_1x_5^2 - 2.26x_3^3 - 1.78x_5^3 \\ \dot{x}_3 = x_4 \\ \dot{x}_4 = 11.1x_1 - 19.4x_3 - 0.5x_4 + 8.31x_5 + 2.97x_1^2 - 5.95x_1x_3 \\ \quad +4.3x_3^2 - 2.64x_3x_5 + 1.32x_5^2 - 1.85x_1^3 + 5.54x_1^2x_3 \\ \quad -5.54x_1x_3^2 + 3.23x_3^3 - 4.15x_3^2x_5 + 4.15x_3x_5^2 - 1.38x_5^3 \\ \dot{x}_5 = x_6 \\ \dot{x}_6 = 22.4x_1 + 21.1x_3 - 43.5x_5 - 0.5x_6 + 4.21x_1^2 - 8.41x_1x_5 \\ \quad +0.836x_3^2 - 1.67x_3x_5 + 5.04x_5^2 - 3.73x_1^3 + 11.2x_1^2x_5 \\ \quad -11.2x_1x_5^2 - 3.52x_3^3 + 10.6x_3^2x_5 - 10.6x_3x_5^2 + 7.25x_5^3 \end{cases} \tag{1-20}$$

$$\begin{cases} \dot{z}_1 = -0.5z_1 - 53.3z_2 - 0.0464z_1z_2 + 4.93z_2^2 - 0.122z_1z_2^2 + 8.69z_2^3 \\ \dot{z}_2 = z_1 + 0.0232z_2^2 + 0.0409z_2^3 \\ \dot{z}_3 = -0.5z_3 - 33.8z_4 - 0.0661z_3z_4 + 4.45z_4^2 - 0.109z_3z_4^2 + 4.91z_4^3 \\ \dot{z}_4 = z_3 + 0.033z_4^2 + 0.0364z_4^3 \end{cases} \tag{1-21}$$

Hyperplane δ_{21}-δ_{31} is chosen to visualize the stability boundary because for a power system, all unstable equilibrium points (UEPs) on the stability boundary are in this plane, which are crucial for power system stability analysis. Here, $\delta_{ij} = \delta_i - \delta_j$ denotes the relative rotor angle difference between generator i and j and is used as the coordinate because angular stability is mainly about the synchronism between the rotors of synchronous machines. Also note that the boundary visualized on this hyperplane is actually the intersection of the hyperplane and the true ROA of the system, as illustrated in Figure 6.

The stability boundaries from the original system, 3-jet and 3-DS are compared in Figure 7. The inconsistency between the original system and 3-DS is analyzed as follows: (*i*) from the original system to the 3-jet, the boundary is shrunk, and (*ii*) from the 3-jet to the 3-DS, their boundaries are consistent well on most parts despite four sharp corners, which together take a small portion of the boundary. Hence, if $\mathbf{f}(\mathbf{X})$ of the original system only consists of polynomial terms, then inconsistency between the boundaries from the original system and the *k*-DS is mainly on the four corners.

To compare the dynamics of the 3-DS and 3-jet with initial states near stability boundaries, three initial states PA, PB and PC are selected: PA and PC are near the "well-consistent" part and PB is in one of the "corners". All the three points are very close to the 3-DS boundary but are still inside, as shown in Figure 8. For the 3-DS, the phase space trajectories starting from PA, PB and PC are shown in Figure 9, Figure 10 and Figure 11, respectively about the two decoupled oscillators. The SEP and UEPs of the 3-DS in (15) is also depicted. Note that each decoupled oscillator has its ROA bounded by

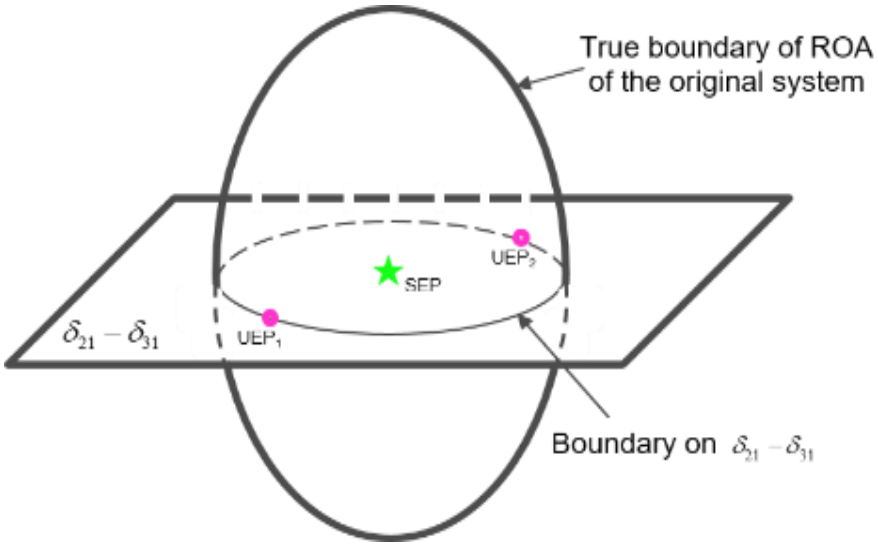

Figure 6. Diagram of IEEE 3-machine 9-bus system.

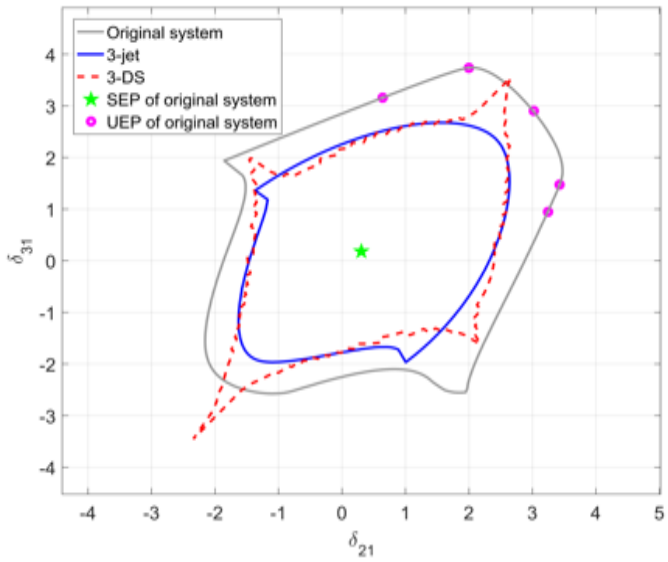

Figure 7. Comparison between the original system, 3-jet and 3-DS.

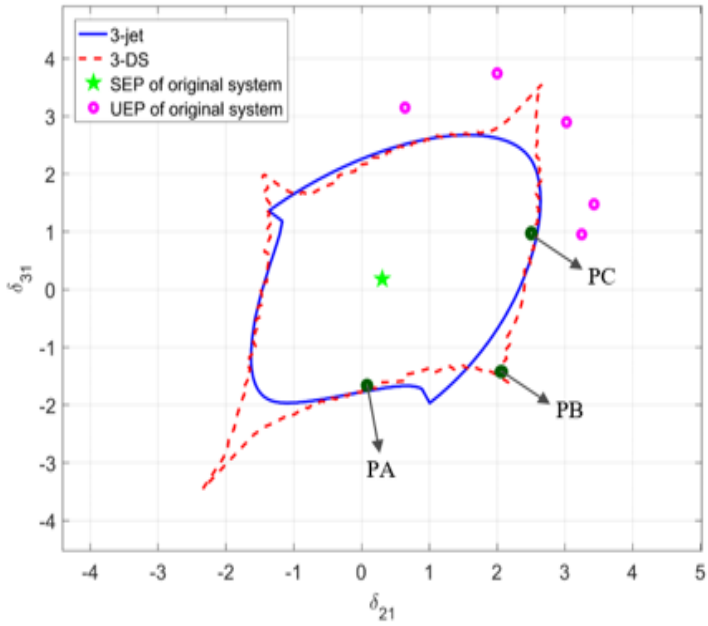

Figure 8. Locations of the starting points PA, PB, and PC.

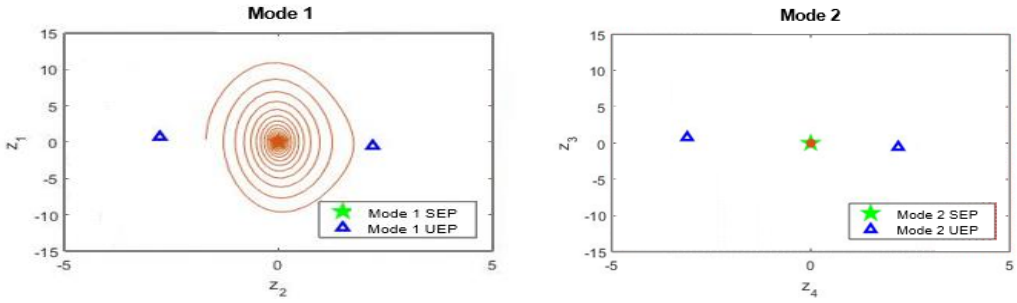

Figure 9. The dynamics of 3-DS with starting point PA.

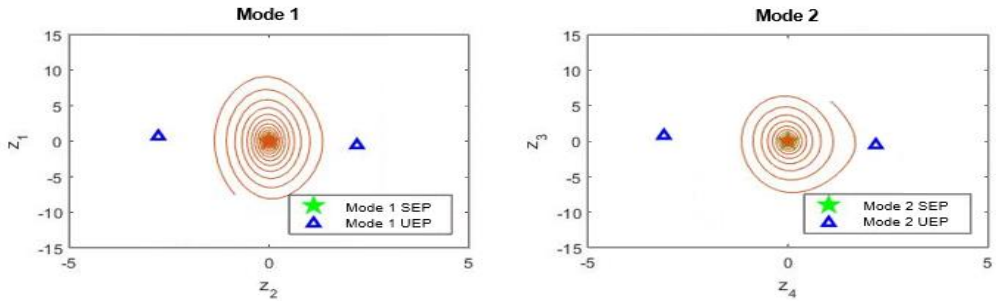

Figure 10. The dynamic of 3-DS with starting point PB

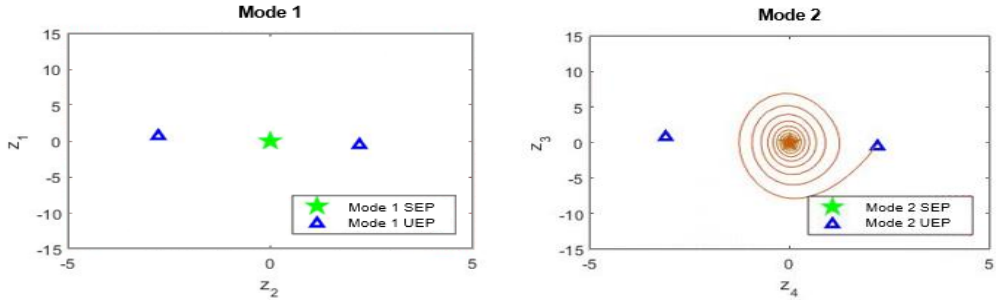

Figure 11. The dynamics of 3-DS with starting point PC.

two UEPs as a one DOF system.

For PA and PC, only one mode is severely excited, while the other one is almost quiescent as shown by Figure 9 and Figure 11. In this case, if the initial state of one decoupled oscillator escapes from its ROA, the corresponding initial states in the original system will escape from the ROA as well. For the initial state PB in one of the "corners", which is outside the stability boundary of the original system. However, the initial states of both decoupled oscillators are still inside their ROAs. The inconsistency between stability boundaries is because both modes are excited as shown by Figure 8. Therefore, excitation of multiple modes may increase the coupling among the modes (or in other words, the coupling of the corresponding oscillators). When using the 3-DS for stability analysis, all the excited modes should be considered.

The shrinkage of the ROA of the 3-jet compared to that of the original system is a main reason causing boundary inconsistency. Note that the boundary of the 3-jet has a similar shape to that of the original system but a smaller size. An intuitive idea for a more accurate stability boundary is to modify the 3-DS by scaling the coefficients in (1-21), such that the new boundary is more consistent with that of the original system. We propose to scale the coefficients of (1-21). Without loss of generality, let $\mathbf{z}_i$ be the state variable after modification, and $\mathbf{y}_i$ be the state variable of the original (1-21). Substitute $\mathbf{y}_i$ into (1-21) to obtain the modified 3-DS system as:

$$\dot{\mathbf{y}}_i = \mathbf{g}_i\left(\mathbf{y}_i\right) \xrightarrow{\mathbf{y}_i=\left[sc_{i1}z_{i1}, sc_{i2}z_{i2}\right]^T} \dot{\mathbf{z}}_i = \tilde{\mathbf{g}}_i\left(\mathbf{z}_i\right) \tag{1-22}$$

where sc_i is the scaling factor, and $\dot{\mathbf{z}}_i = \tilde{\mathbf{g}}_i\left(\mathbf{z}_i\right)$ is the oscillator after modification.

Tentatively change the scaling factors and test the consistency of the stability boundaries. A modified 3-DS system with sc_{11}=sc_{21}=1 and sc_{21}=sc_{22}=0.86 are shown in (1-23) and its boundary of ROA is shown in Figure 12, from which a less conservative boundary is obtained by scaling, despite of the "corners" outside of the boundary of the original system.

$$\begin{cases} \dot{z}_1 = -0.5z_1 - 45.8z_2 - 0.0399z_1z_2 + 3.65z_2^2 - 0.0902z_1z_2^2 + 5.53z_2^3 \\ \dot{z}_2 = 1.16z_1 + 0.02z_2^2 + 0.0302z_2^3 \\ \dot{z}_3 = -0.5z_3 - 29.1z_4 - 0.0568z_3z_4 + 3.29z_4^2 - 0.0806z_3z_4^2 + 3.12z_4^3 \\ \dot{z}_4 = 1.16z_3 + 0.0284z_4^2 + 0.0269z_4^3 \end{cases} \quad (1\text{-}23)$$

In conclusion, the numerical studies show that the boundary inconsistency between the original system and decoupled system is caused by (*i*) the truncation from the original system to the *k*-jet to shrink the ROA, and (*ii*) the truncation from the *k*-jet to the *k*-DS to cause mismatches on corners of the ROA. However, with the use of 3-jet and 3-DS, the main portion of the ROA from NMD basically matches the accurate ROA.

2.2.4 Approximation of the Closest Unstable Equilibrium Point

Due to those two truncations, $\mathbf{EX}_{appro}$ cannot exactly provide the UEPs in **EX**. However, if (1-3) have a more conservative stability boundary, we can expect that (1-8) could be used to approximate the closest UEP, at which the energy is lower than the true closest UEP of the original system. This idea motivates the closest UEP approximation procedure.

Based on the analysis on sets of the EPs, a procedure for approximating the closest UEP via NMD is proposed as described below.

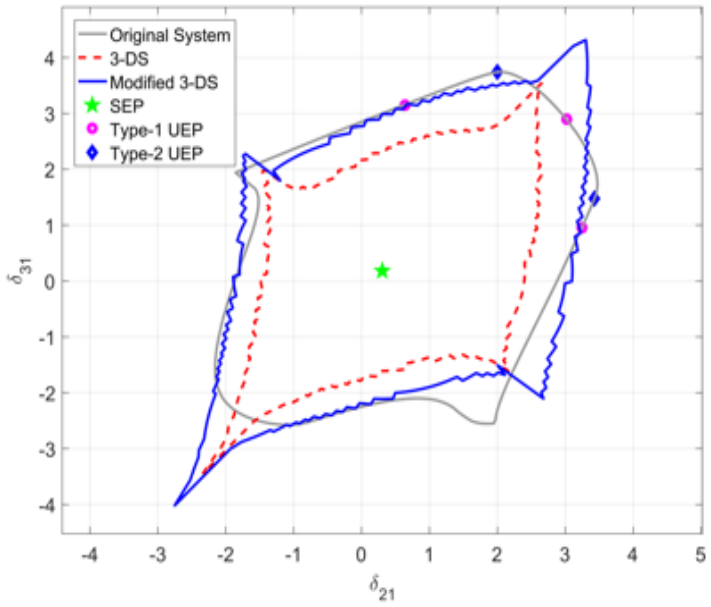

Figure 12. Boundaries of the original system, 3-DS, and modified 3-DS.

Step1: For a given original system in (1-1), find the 3-jet system and decouple it via NMD.

Step2: Solve the EPs of the decoupled system, $\mathbf{EZ}_{DS}$. Then obtain $\mathbf{EX}_{appro}$ by $\mathbf{EX}_{appro} = \mathbf{H}(\mathbf{EZ}_{DS})$. $\mathbf{EX}_{appro}$ is viewed as an approximation of **EX**.

Step3: Find the UEPs among $\mathbf{EX}_{appro}$, and evaluate their energy via a given energy function. Select the one with least energy as the approximated closest UEP.

Remarks

In **Step 2**, to obtain $\mathbf{EZ}_{DS}$, first solve the UEPs of each oscillator (1-9) to obtain $\mathbf{EZ}_{Osc,i}$. Then, the Cartesian product of all the $\mathbf{EZ}_{Osc,i}$ is exactly $\mathbf{EZ}_{DS}$. The UEPs of each oscillator are much easier to solve since mathematically it is equivalent to solve the roots of two equations with two variables. ■

The IEEE 9-bus power system is used to test the performance of the closest UEP approximation using NMD. Three cases are considered with different settings of dynamic parameters, as shown in Table 5. Their differences in inertia and damping may lead to the different EPs, and thus different closest UEPs. But they all have the same SEP, $(\delta_{21}, \delta_{31}) = (0.3047 \text{ rad}, 0.1901 \text{ rad})$.

The distribution of the EPs of the original system, including the type-1 and type-2 UEPs, are drawn on $\delta_{21}-\delta_{31}$ plane, as shown in Figure 13, Figure 14 and Figure 15, for case 1-3, respectively. Those true EPs can be identified by either exhaustive search, or using the holomorphic embedding method [42]. The closest UEPs of each case are marked by solid black circles, and listed in Table 6. The energy function to be used is the same as the one in [43], in which the path-dependent integral is approximated by using a

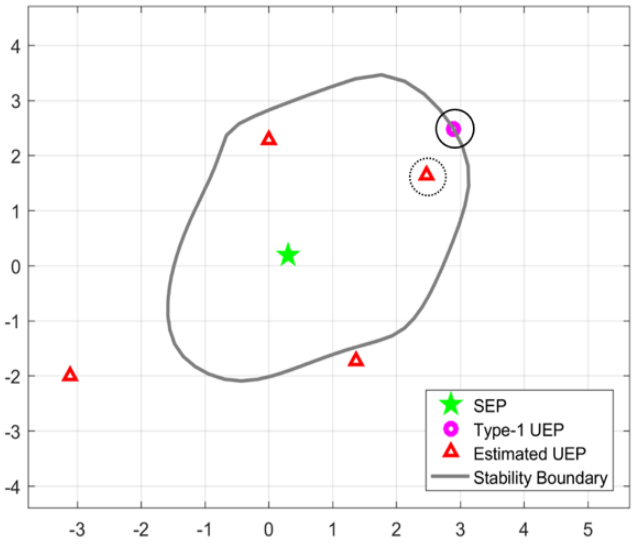

Figure 13. UEPs of the original system and approximated UEPs in case 1.

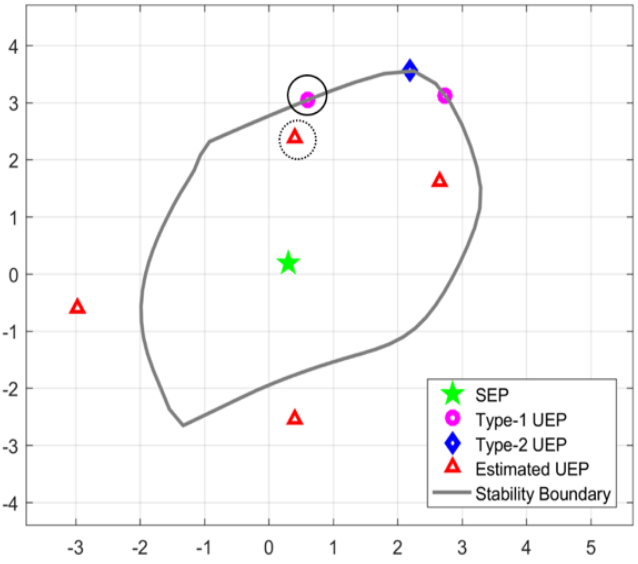

Figure 14. UEPs of the original system and approximated UEPs in case 2.

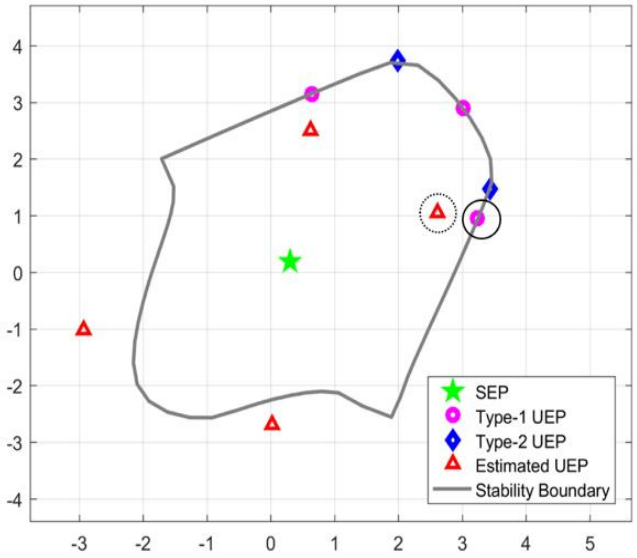

Figure 15. EPs of the original system and approximated UEPs in case 3.

Table 5. Dynamic Data

Case	H_1 (s)	H_2 (s)	H_3 (s)	D_1 (s)	D_2 (s)	D_3 (s)
1	25.640	6.400	3.010	25.640	6.400	3.010
2	25.640	25.600	3.010	25.640	25.600	3.010
3	25.640	25.600	10.535	25.640	25.600	10.535

Table 6. Closest UEP of each case

Case #	δ_{21}	δ_{31}	***Energy***
Case 1	2.8907	2.4931	3.1964
Case 2	0.6020	3.0512	3.4387
Case 3	3.2433	0.9515	3.6369

linear integral path. In addition, the stability boundary on the $\delta_{21}-\delta_{31}$ plane is also shown for comparison.

The NMD is implemented in each case, and the closest UEP approximation procedure is used to approximate the closest UEP. In each case, within a domain surrounding SEP, the approximated UEPs are visualized on the $\delta_{21}-\delta_{31}$ plane in Figure 13, Figure 14 and Figure 15. Those UEPs are also listed in Table 7, Table 8, and Table 9, respectively for cases 1-3. The ones with the lowest energy are identified as the approximated closest UEPs, which are marked by dotted circles in figures and shaded in grey in tables.

The results show that the approximated UEPs via NMD is not always geometrically close to the UEPs of the original system, which is due to the two truncations. However, the approximated closest UEP are always close to the closest UEP of the original system. Moreover, the energy of these approximated closest UEP is always lower than the energy of the corresponding true closest UEP. Hence, it would be worthwhile to investigate how to use the proposed closest UEP approximation procedure for the stability analysis purpose.

In addition, although the rest of the approximated UEPs may not be geometrically close to the UEPs of the original system, they are close to the stability boundary of the original system. Thus, it would be worthy to investigate the relation of the approximated UEPs and the stability boundary.

Table 7. Approximated UEPs and Approximated Closest-UEP of 3-Machine System in Case 1

UEP #	δ_{21}	δ_{31}	***Energy***
1	-3.1229	-2.0052	8.0840
2	2.4651	1.6408	3.1927
3	1.3662	-1.7296	5.2159
4	0.0043	2.2969	3.3399

Table 8. Approximated UEPs and Approximated Closest-UEP of 3-Machine System in Case 2

UEP #	δ_{21}	δ_{31}	***Energy***
1	0.3999	-2.5485	5.9253
2	0.3969	2.3768	3.0687
3	-2.9773	-0.5948	7.7325
4	2.6573	1.6179	3.4200

Table 9. Approximated UEPs and Approximated Closest-UEP of 3-Machine System in Case 3

UEP #	δ_{21}	δ_{31}	***Energy***
1	-2.9372	-1.0152	7.6929
2	2.6019	1.0492	3.2279
3	0.0111	-2.6867	5.7882
4	0.6236	2.5114	3.2686

2.2.5 Conclusions on Stability Comparison

The conclusions on the stability comparison are listed below.

- TTE systems at orders 2, 5, 6 and 9 give optimistic TSA results while those at orders 3, 4, 7 and 8 give conservative results. Since 3rd order TTE could be preferable for fast stability analysis since it has the least polynomial terms among all the TTEs giving conservative results.

- Boundary inconsistency is caused by (*i*) the truncation from the original system to the *k*-jet to shrink the ROA, and (*ii*) the truncation from the *k*-jet to the *k*-DS to cause mismatches on corners of the ROA. With the use of 3-jet and 3-DS, the main portion of the ROA from NMD basically matches the accurate ROA.

- The closest UEP approximated from NMD is geometrically close to the closest UEP of the original system. A procedure for the closest UEP approximation via NMD is proposed.

2.3 Nonlinear Modal Decoupling Based Power System Transient Stability Analysis

In this section, NMD is applied on power system model for TSA. First, how to apply NMD on power system model is discussed. Then, the first integral and Zubov's method for estimating the stability boundary of each decoupled oscillator are introduced. After that, the procedure for applying the NMD on large-scale power system is given. Finally, numerical studies on the 48-machine Northeast Power Coordinating Council system is analyzed.

2.3.1 NMD on Large-Scale Power System Model

Although NMD can be applied to the power system model (1-15) without any limitations in theory, some modifications are needed when dealing with high-dimensional model due to the intensive computation burden. In this section, the generic procedure for applying NMD on power system model is given. Then, some modifications are proposed to reduce the computation burden for large-scale power system model.

Denote $\hat{\mathbf{x}}=[\boldsymbol{\delta}^{\mathrm{T}}, \Delta\boldsymbol{\omega}^{\mathrm{T}}]^{\mathrm{T}}$ as the state vector. The first-order differential equations of the system in (1-15) have the form:

$$\dot{\hat{\mathbf{x}}} = \mathbf{f}_0(\hat{\mathbf{x}}) \tag{1-24}$$

Apply a transformation matrix **R**, whose columns are right eigenvectors of $\mathbf{f}_0$'s Jacobian matrix, to both sides of (1-24) to obtain its modal space representation as below, where $\mathbf{y} = [y_{11}\ y_{12}\ \ldots\ y_{m1}\ y_{m2}]^{\mathrm{T}}$ is the new state vector.

$$\dot{\mathbf{y}} = R^{-1}\mathbf{f}_0(R\mathbf{y}) \triangleq \mathbf{g}(\mathbf{y}), \quad \text{where } \mathbf{y} = R^{-1}\hat{\mathbf{x}} \tag{1-25}$$

Without loss of generality, let y_{11}, y_{12}, ..., $y_{m\text{-}1,1}$, $y_{m\text{-}1,2}$ represent the relative motions of the system, and y_{m1} and y_{m2} represent the mean motions, which are non-oscillatory dynamics that all generators are moving together. It has been proved in [44] that the relative motions can be represented by an (m-1)-oscillator system consisting of different equations about y_{m1}, y_{m2}, ..., $y_{m\text{-}1,1}$, $y_{m\text{-}1,2}$. Thus, the first (2m–2) equations of (1-25) are the model in (1-1) with N = (2m–2), to which the NMD will be applied.

For a large-scale multi-machine power system, the implementation of NMD on (1-25) could be computationally expensive. It is often observed that when a power system is subject to a disturbance, usually only a few modes are significantly excited while the

rest of the modes are either quiescent or less influential in stability of the system. Thus, a large-scale system can be reduced to a smaller system only about the dynamics associated with those few selected modes.

Re-write the first (2*m*–2) equations in (1-25) as (1-26), which partitions (2*m*–2) equations into two groups: one group for the modes of interest (denoted with subscript "int") and the other group for the rest of modes (denoted with subscript "non").

$$\begin{pmatrix} \dot{\mathbf{y}}_{\text{int}} \\ \dot{\mathbf{y}}_{\text{non}} \end{pmatrix} = \begin{pmatrix} \mathbf{g}_{\text{int}}(\mathbf{y}_{\text{int}}, \mathbf{y}_{\text{non}}) \\ \mathbf{g}_{\text{non}}(\mathbf{y}_{\text{int}}, \mathbf{y}_{\text{non}}) \end{pmatrix} \tag{1-26}$$

Ignore the dynamics with the second group, i.e. admitting (1-27). Then, eq. (1-26) is reduced to (1-28) containing only the modes of interest. NMD will be applied to (1-28) to obtain the decoupled system.

$$\begin{cases} \dot{\mathbf{y}}_{\text{non}} = \mathbf{0} \\ \mathbf{y}_{\text{non}} = \mathbf{0} \end{cases} \tag{1-27}$$

$$\dot{\mathbf{y}}_{\text{int}} = \mathbf{g}_{\text{int}}(\mathbf{y}_{\text{int}}, \mathbf{0}) \tag{1-28}$$

For the sake of convenience, the *i*th decoupled system is represented in the form of (1-29), where $w_{2i\text{-}1}$ and w_{2i} are its state variables. υ and ν are coefficients and *k* denotes the highest order of polynomial terms to be kept. In the case studies, *k* is selected to be 3 as indicated by section 2.2.1 unless specifically explained.

$$\begin{cases} \dot{w}_{2i-1} = \upsilon_{i10} w_{2i-1} + \sum_{l=1}^{k} \upsilon_{i0l} w_{2i}^{l} + \sum_{\substack{j\geq 1, l\geq 0 \\ (j,l)\neq(1,0)}}^{j+l\leq k} \upsilon_{ijl} w_{2i-1}^{j} w_{2i}^{l} \\ \dot{w}_{2i} = w_{2i-1} + \sum_{j\geq 0, l\geq 0}^{2\leq j+l\leq k} \nu_{ijl} w_{2i-1}^{j} w_{2i}^{l} \end{cases} \tag{1-29}$$

2.3.2 Stability Analysis of Mode-Decoupled Systems: First Integral and Zubov's method

The numerical search algorithm in section 2.2.1 can give a fairly accurate estimate for the mode-decoupled systems. The entire time cost is moderate since each decoupled system only has two state variables. With the estimated boundary from numerical search algorithm as a reference, the following will present two analytical approaches for estimating the stability boundary.

First integral

Eq. (1-30) gives a necessary and sufficient condition for (1-1) to have a first-integral based Lyapunov function. Unfortunately, there are no general methods for constructing a first-integral based Lyapunov function for nonlinear dynamical systems [45].

$$\sum_{j=1}^{N} \frac{\partial f_j}{\partial x_j} = 0 \tag{1-30}$$

With the help of NMD, after admitting the assumptions in (1-31) and (1-32), the system in (1-29) can be transformed to (1-33), and a Lyapunov function $V(w_{2i-1},w_{2i})$ for (1-29) can be constructed as in (1-34).

$$\begin{cases} \upsilon_{ijl} = 0 & \text{for all } j \geq 1, l \geq 1,\ j + l \leq k, (j,l) \neq (1,0) \\ \nu_{ijl} = 0 & \text{for all } j \geq 0, l \geq 0, 2 \leq j + l \leq k \end{cases} \tag{1-31}$$

$$\upsilon_{i10} = 0 \tag{1-32}$$

$$\begin{cases} \dot{w}_{2i-1} = \sum_{l=1}^{k} \upsilon_{i0l} w_{2i}^{l} \\ \dot{w}_{2i} = w_{2i-1} \end{cases} \tag{1-33}$$

$$\frac{dw_{2i}}{dw_{2i-1}} = \frac{\dot{w}_{2i}}{\dot{w}_{2i-1}} = \frac{w_{2i-1}}{\sum_{j=1}^{k} \upsilon_{ij} w_{2i}^{j}}$$
$$\Rightarrow V(w_{2i-1}, w_{2i}) = \frac{w_{2i-1}^2}{2} - \int_0^{w_{2i}} \sum_{j=1}^{k} \upsilon_{ij} s^j ds = \frac{w_{2i-1}^2}{2} - \sum_{j=1}^{k} \frac{\upsilon_{ij}}{j+1} w_{2i}^{j+1} \quad (1\text{-}34)$$

Note that the assumption in (1-31) changes the nonlinear characteristics of the system, while the assumption (1-32) forces the oscillation damping to zero, which does not have a significant influence on the stability analysis result. Validated by the numerical studies presented later in section 2.3.3, the coefficients ignored by (1-31) are always found to be small and ignoring positive damping can keep the stability analysis based on (1-29) to be conservative.

For each decoupled system in (1-29), the closest UEPs denoted by w_{2i}, UEP can be obtained by letting the right hand side be zero and solving the resulting algebraic equations for the roots with the smallest magnitude. Note that there may be one or two (a positive one and a negative one) closest UEPs depending on the order *k*. Then, the critical energy is defined as $V(0, w^*_{2i})$, where w^*_{2i} is selected as the UEP having a smaller energy. When the systems in (1-29) has an initial state $(w_{2i-1}(0), w_{2i}(0))$, it is stable if and only if $V(0, w^*_{2i}) \geq V(w_{2i-1}(0), w_{2i}(0))$. Therefore, the stability boundary of (1-29) can be approximated by an equipotential curve of (1-29) with the potential of $V(0, w^*_{2i})$, i.e.:

$$V(w_{2i-1}, w_{2i}) = V(0, w^*_{2i}) \quad (1\text{-}35)$$

Zubov's method

A Lyapunov function $V(\mathbf{X})$ for determining the exact stability boundary of the ordinary differential equations in (1-1) can be constructed by solving the partial

differential equation in (1-36), called the Zubov's equation [46], [47]. Note that the mode-decoupled system in (1-29) is a special case of the general system in (1-1). Thus, this subsection only applies the Zubov's method to (1-1). All conclusions drawn are automatically applicable to (1-29).

$$\sum_{j=1}^{N} \frac{\partial V(\mathbf{x})}{\partial x_j} f_j(\mathbf{x}) = -\varphi(\mathbf{x}) \cdot \left(1 - V(\mathbf{x})\right) \tag{1-36}$$

where $\varphi(\mathbf{X})$ is a positive definite or semidefinite function of $\mathbf{X}$. Note that $\varphi(\mathbf{X})$ must be chosen before solving the above equation, and its selection will not influence the resulting stability boundary.

Several necessary theorems (see proofs in [46]) and definitions are briefly reviewed below due to their importance for understanding the Zubov's method based stability analysis.

Theorem III-C1. The function $V(\mathbf{X})$ solved from (1-36) is a Lyapunov function establishing the asymptotic stability of the unperturbed motion at the SEP of the system .

Definition III-C1. Let Ω be the set of the initial values $\mathbf{X}_0$ which make up the domain of asymptotic stability of the unperturbed motion at the SEP of the system in (1-1). Thus, Ω is the ROA of the system (1-1).

Theorem III-C2. If $\mathbf{X}$ is in Ω, then

$$0 \le V(\mathbf{x}) < 1 \tag{1-37}$$

Theorem III-C3. The stability boundary of the system in (1-1), i.e. the boundary of Ω, is the surface defined by $V(\mathbf{X}) = 1$.

Eq. (1-1) has a closed-form solution only for very special cases, while whose solution can always be represented in a power series form (1-38), where $V_j(\mathbf{X})$ represents

all homogeneous terms of order j in $\mathbf{X}$. Truncating the terms above order L, an approximate of $V(\mathbf{X})$ is given in (1-39).

$$V(\mathbf{x}) = \sum_{j=2}^{\infty} V_j(\mathbf{x}) \tag{1-38}$$

$$V(\mathbf{x}) \approx V^{(L)}(\mathbf{x}) = \sum_{j=2}^{L} V_j(\mathbf{x}) \tag{1-39}$$

Definition III-C2. Given $V^{(L)}(\mathbf{X})$ in (1-39), define the set Φ and the constant scalar $v^{(L)}$ respectively b (1-40) and (1-41).

$$\Phi = \{\mathbf{x} \mid \dot{V}^{(L)}(\mathbf{x}) = 0\} \tag{1-40}$$

$$v^{(L)} = \min\{V^{(L)}(\mathbf{x}) \mid \mathbf{x} \in \Phi\} \tag{1-41}$$

Theorem III-C4. The surface $V^{(L)}(\mathbf{X}) = v^{(L)}$ is completely contained in Ω.

Remarks

Note that even though there is no theoretical difficulty in estimate the stability boundary from (1-40) and (1-41), there could be a huge computational burden for systems with high dimensions [48]. Thus, the above analysis is applied to each of the mode-decoupled systems in (1-29) rather than the original N-dimensional system in (1-1). In theory, the Lyapunov function with infinite terms in (1-38) is independent of the choice of the function φ used in the Zubov's equation (1-38). However, when a finite number of terms are kept in (1-38), the choice of the function φ influences the rate of convergence. In addition, the intuition that keeping more terms will always give better accuracy is unnecessarily true even for an SMIB system [49]. The optimal selection of the function and the order L is not a focus here but deserves further investigations [50]. In

the case studies, we choose φ and L based on our experience on extensive case studies and use them for all test cases. ■

2.3.3 Procedure for Large-scale Power Systems

For a power system with not many generators, the NMD can be applied directly to the entire system to determine (m–1) independent second-order systems in the form of (1-29) with polynomial nonlinearities up to a desired order k, as shown by the following procedure (named "**NMD-TSA 1**"):

Step 1: Given an m-machine system represented by (1-24), derive the modal space representation (1-25).

Step 2: Assume uniform damping and obtain a unique (m–1)-oscillator system by the first (2m–2) equations in (1-25).

Step 3: Apply NMD to this (m–1)-oscillator system to obtain (m–1) decoupled second-order systems in the form of (1-29) that respectively correspond to (m–1) oscillation modes.

Step 4: Apply a stability analysis by either first integral or Zubov's method to estimate the stability boundary of each of these (m–1) nonlinear oscillators.

Step 5: For the original system, i.e. (1-24), given any trajectory subjected to a disturbance of interest, transform it to the decoupled coordinates using NMD transformations, and visualize the transformed trajectory. If the trajectory does not exceed the stability boundary obtained in step 4 for any mode, the system subject to that disturbance is assessed to be stable; otherwise, it is considered unstable.

The stability boundary of each mode-decoupled system actually represents a portion of the stability boundary of the original system that is projected to the decoupled coordinates about one mode.

For large-scale power system, NMD is applied to (1-28) instead of (1-25), and perform a stability analysis on each of the resulting mode-decoupled systems to obtain TSA results. The above enhanced TSA procedure for large-scale multi-machine systems is named "**NMD-TSA 2a**".

Remarks

(a) We called a multi-machine power system small or large mainly depending on computational requirement of the proposed approach. Currently, the derivation of NMD is implemented using Symbolic Math Toolbox in Matlab, which is not highly efficient. Thus, power systems with 2-6 machines are thereby called small systems, while those with more machines are called large systems. Since NMD has similar computation procedures to normal form [51]-[53], a more efficient implementation is also achievable, with which power systems with up to 50 machines may be considered as small [54].

(b) In addition, The **NMD-TSA 2a** procedure may introduce errors of TSA in two aspects. First, to reduce the large-scale system, dynamics with most modes that having little impact on stability are neglected, and hence the stability boundary estimated with respect to the modes of interest may not exactly match the true boundary. Second, inter-modal terms of orders $>k$ are not considered in the decoupled systems but they may become unneglectable when the system state is far from the SEP, especially when approaching the transient stability boundary. Therefore, even if **NMD-TSA 2a** judges a

post-disturbance trajectory to be stable, there is still a possibility that the original system may exit the true stability boundary due to influences from the ignored modes and high order inter-modal terms. ■

To address the issue in the second remark, a shrinking ratio *r* defined in (1-42) is adopted to shrink the stability boundary about the *i*th mode in (1-28) based on estimates of modal energies by (1-43)-(1-45). Here, we assume that the speed deviation of any generator rotor can be represented by a sum of sinusoids as shown in (1-45) about excited modes in (1-28). The representation (1-45) can be estimated by modal analysis tools, e.g. Prony and Matrix pencil methods, on stable trajectories.

$$r_i \overset{\Delta}{=} E_i / E_{\text{all}} \tag{1-42}$$

$$E_i \overset{\Delta}{=} a\sum\nolimits_{j=1}^{m} H_j A_{ji}^2 \tag{1-43}$$

$$E_{\text{all}} \overset{\Delta}{=} \sum\nolimits_i E_i \tag{1-44}$$

$$\Delta\omega_j(t) = A_{ji} e^{\sigma_i t}\cos(\Omega_i t + \phi_{ji}) + \sum\nolimits_{k\neq i} A_{jk} e^{\sigma_k t}\cos(\Omega_k t + \phi_{jk}) \tag{1-45}$$

where E_i and E_{all} respectively represent the transient energies of mode *i* and all modes; H_j is the inertia constant of machine *j*; *a* is a certain constant, whose value does not affect the shrinking ratio r_i at all; $\Delta\omega_j(t)$ represents the trajectory of speed deviation of machine *j*, with A_{jk}, ϕ_{jk}, σ_{jk} and Ω_k as the amplitude, phase, damping and frequency of mode *k*.

The procedure that additionally applies the shrinking ratio to the stability boundary about each mode is named "**NMD-TSA 2b**" for comparison purposes. For instance, the estimated stability boundaries by the aforementioned first integral method and the Zubov's method become $V(w_{2i-1}, w_{2i}) = r_i V(0, w^*_{2i})$ and $V^{(L)}(\mathbf{X}) = r_i v^{(L)}$,

respectively. Note that calculation of the shrinking ratio requires a stable trajectory and is contingency-dependent, while **NMD-TSA 1** and **2a** are contingency-independent.

To summarize, NMD-based TSA for general power systems may contain three types of error: (i) truncation errors due to ignoring high-order Taylor expansion terms of (1-1), (ii) model decoupling errors due to ignoring inter-modal terms of orders $>k$ of (1-6), and (iii) the estimation errors of the stability boundary. In section 2.2.1, the first type of errors is investigated and it is suggested that a third order polynomial truncation be used for both conservative stability assessment and moderate computational burden, which will be adopted in case studies.

2.3.4 Case Studies on NPCC 140-bus System with Classical Model

A simplified NPCC system is adopted to demonstrate a potential application of NMD based TSA for early warning of the oscillation mode that may most likely develop into a transient instability in large power systems. It contains 48 generators and 140 buses, [55], [56]. A temporary three-phase fault is added at bus 13 and cleared after a certain time without disconnecting any line. The critical clearing time of this contingency is 0.16 second and the resulting post-contingency response is shown in Figure 16. By calculating the modal energies according to the definition in (1-43)-(1-45), it is found that this fault only largely excites a few modes, as indicated by Table 10. When the fault duration increases to 0.17s, the system will lose its stability as shown in, where all rotor angles are divided into two clusters. The diagram of NPCC 140-bus system and the two clusters are shown in Figure 17. The polynomial terms in the decoupled system is kept up to the 3rd order.

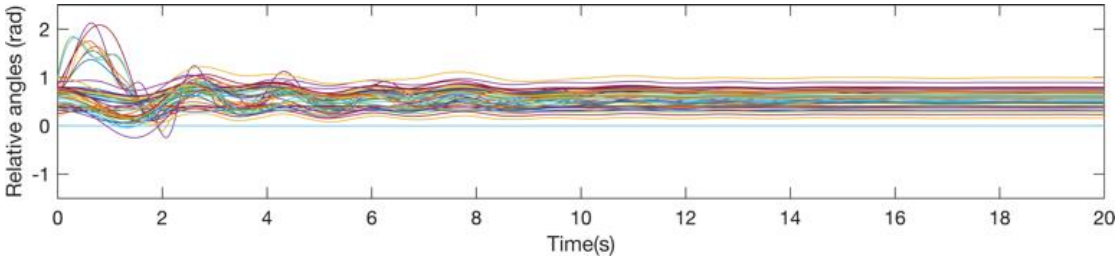

Figure 16. Marginally stable relative rotor angles w.r.t. generator 78.

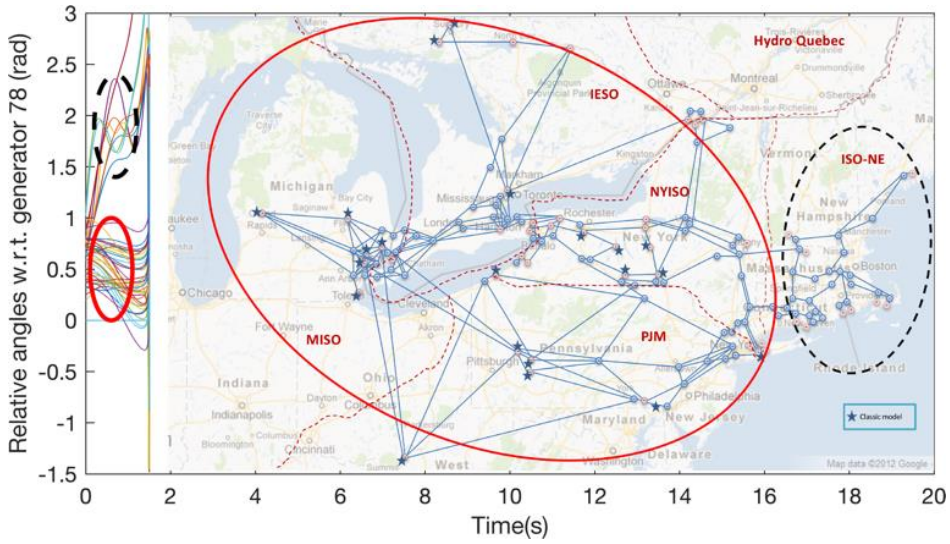

Figure 17. One-line diagram of the 140-bus NPCC power system (right) and the marginally unstable relative rotor angles w.r.t. generator 78 (left).

Table 10. Modal Energy Under the Studied Contingency

f_i(Hz)	E_i^*	f_i(Hz)	E_i	f_i(Hz)	E_i	f_i(Hz)	E_i
0.38	1	1.28	<10-3	1.57	<10-4	1.69	<10-6
0.26	0.51	1.56	<10-3	1.58	<10-5	1.99	<10-6
0.53	0.17	0.96	<10-3	1.40	<10-5	1.45	<10-6
0.60	0.12	1.04	<10-3	1.68	<10-5	2.51	<10-6
0.47	0.02	0.83	<10-3	1.28	<10-5	1.70	<10-7
2.44	0.01	0.95	<10-3	1.20	<10-5	1.41	<10-7
1.27	<10-2	0.91	<10-3	1.63	<10-5	1.51	<10-8
1.14	<10-2	1.55	<10-3	2.14	<10-5	1.87	<10-8
1.41	<10-2	1.38	<10-4	2.09	<10-5	1.85	<10-9
0.72	<10-2	1.78	<10-4	1.33	<10-6	1.69	<10-10
0.70	<10-3	1.72	<10-4	2.06	<10-6	1.35	<10-33
1.08	<10-3	1.17	<10-4	1.78	<10-6		

* All the model energies are normalized by the energy of the 0.38Hz mode

The **NMD-TSA 2b** is applied to the top-five largely excited modes. The stability boundaries estimated by **NMD-TSA 2b** with first integral and Zubov's method about five modes are shown in Figure 18, respectively. On one hand, it should be noted that the complex behaviors of generators shown in Figure 17 become much simpler to understand in Figure 18, which clearly shows whether the system is going back to the SEP or not upon the fault clearance. When the marginally stable contingency occurs, the 0.6Hz mode in Figure 18(d) is more likely to transit to instability modes because the post-contingency state of the system is close to the boundary. Thus, an early warning signal should be generated to request for preventive control actions. On the other hand, the four modes in Figure 18(a)(b)(c)(e) are quite stable even though they are excited to exhibit noticeable dynamics. In addition, note that the two split clusters of generators under the marginally unstable contingency match the mode shape of the 0.6 Hz mode, which further validates the correctness of the early warning produced by the proposed method.

Therefore, mode-by-mode stability information can be assessed by the NMD based TSA to signal an early warning of the oscillation mode that may most likely develop into a transient instability in a large power system. This information would be valuable for identification of the most vulnerable grid interface(s) for preventive/remedial control actions. However, by no means the proposed approach can replace the conventional simulation-based TSA tools since the results from NMD based TSA are still approximate, as illustrated in Figure 18(d), where the marginally stable trajectory has a small portion located outside the ROA while the marginally unstable trajectory has a small portion inside.

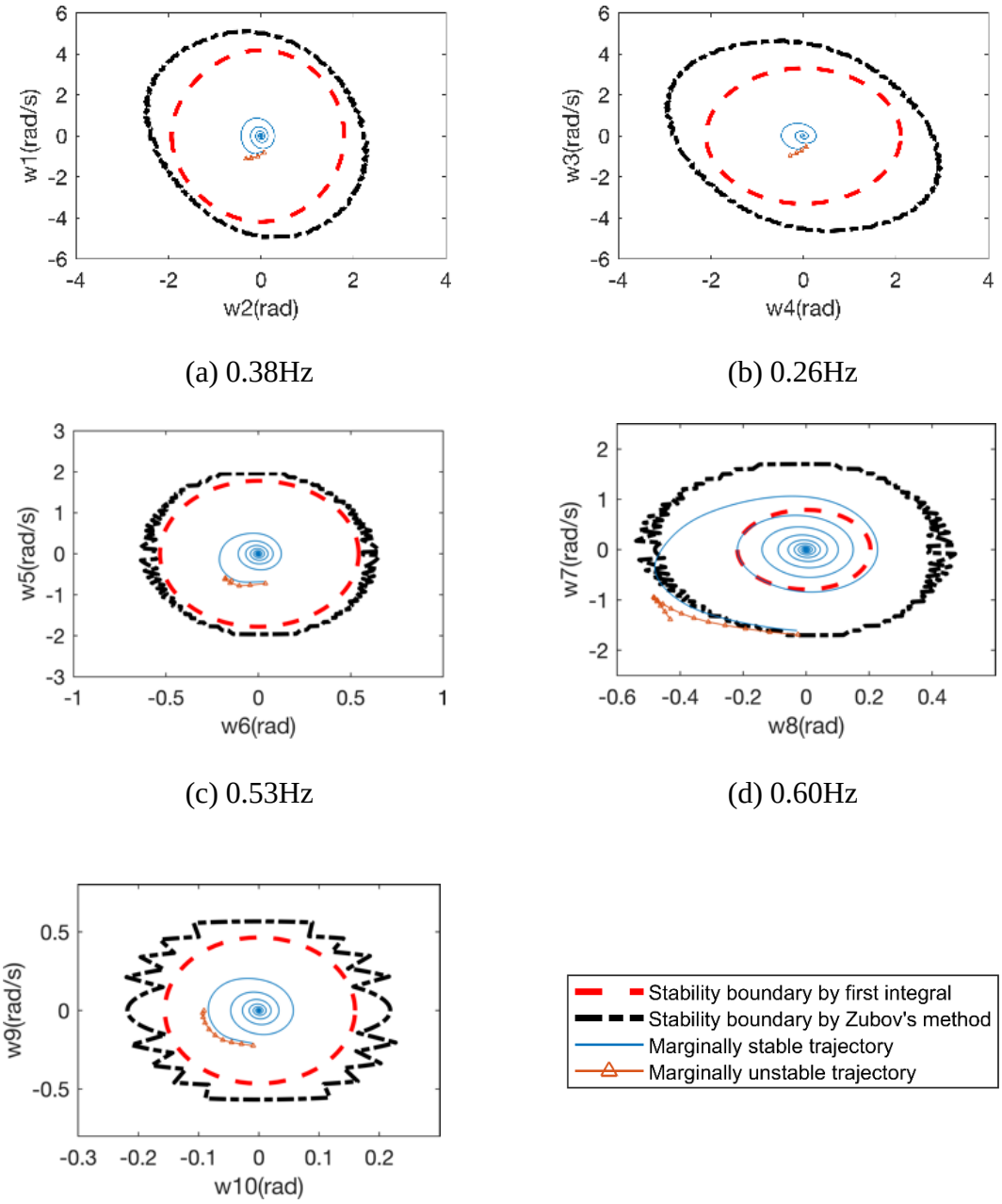

(a) 0.38Hz (b) 0.26Hz

(c) 0.53Hz (d) 0.60Hz

(e) 0.47Hz (f) Legend

Figure 18. Shrunk stability boundaries of mode-decoupled system by NMD-TSA 2b. Trajectories are obtained using classical model.

The early warning provided by the NMD methodology is promising to be used in an out-of-step (OOS) protection system. The following strategy is one idea but will need further investigation. A nonlinear oscillator about the 0.6Hz mode as shown in Figure 18(d), from the proposed approach can be embedded in a properly selected OOS relay, e.g. on the two interties connecting the regions of ISO New England and New York ISO. Multiple variations of the oscillator can be prepared offline representing different operating conditions. In the online environment, measured system trajectory (assuming the availability of wide-area measurement data) can be transformed into the coordinates regarding the 0.6Hz oscillator for prediction of OOS between the two regions. Such a strategy may coordinate with traditional OOS logics to enable a more adaptive special protection system.

2.3.5 Case Studies on NPCC 140-bus System with Detailed Model

The detailed NPCC 140-bus power system with excitation and governor controls [55] is used to show to what extent the NMD based TSA result based on the classical model can work for the stability analysis with the associated detailed model. It is simulated with the same contingency in Section 2.3.3.

The projection of the marginally stable and unstable trajectories to each mode are shown in Figure 19. Comparing Figure 19 to Figure 18, it is observed that the difference compared to the trajectories from the associated classical model seems not significant in the decoupled coordinates. Therefore, the modeling details of the generator do not affect the overall accuracy, which implies that the major error in the entire process of NMD is from the two truncations, i.e. truncating Taylor expansion and truncating high-order

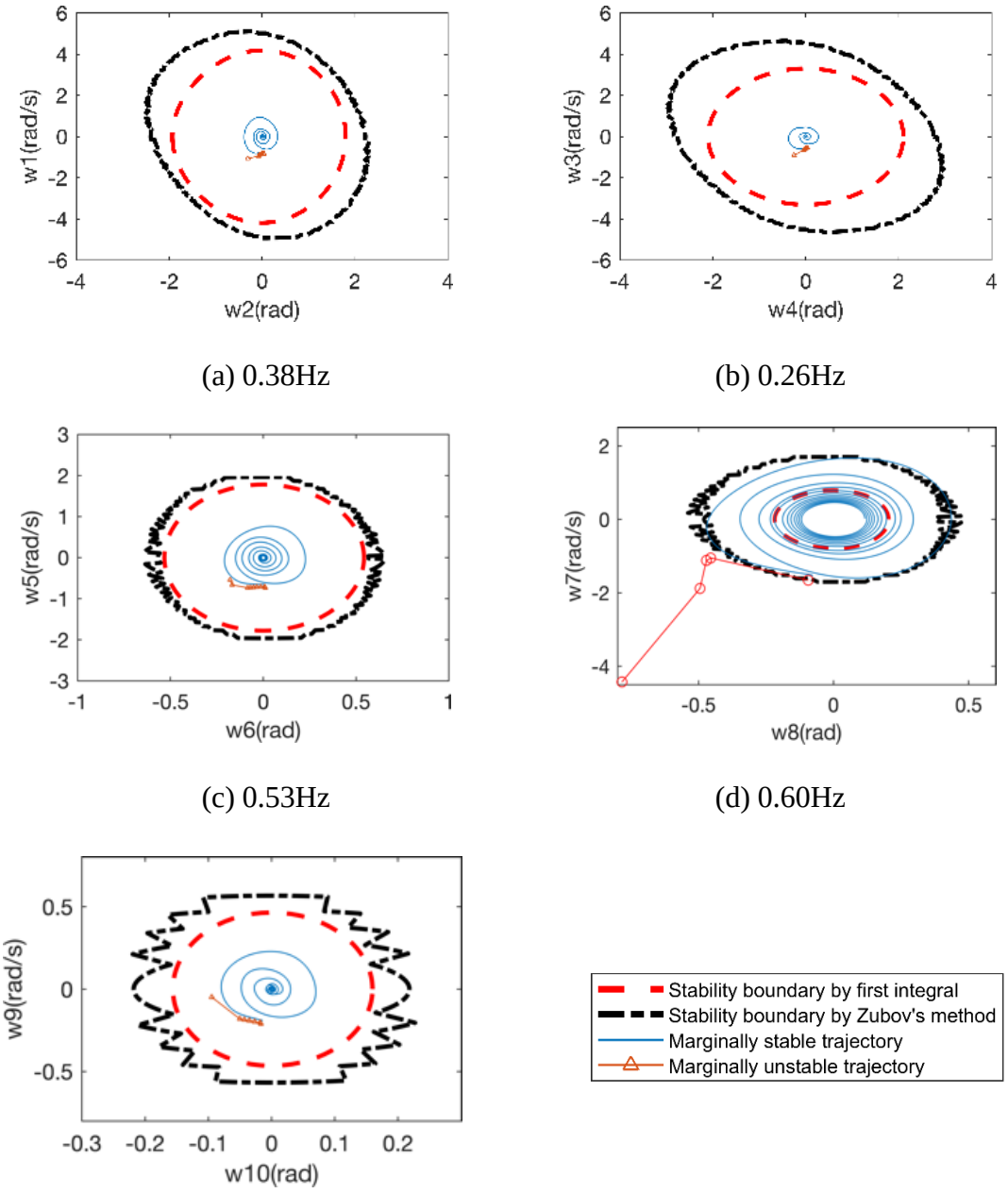

(a) 0.38Hz (b) 0.26Hz

(c) 0.53Hz (d) 0.60Hz

(e) 0.47Hz (f) Legend

Figure 19. Shrunk stability boundaries of mode-decoupled system by NMD-TSA 2b using classical model. Trajectories are obtained using detailed model.

nonlinear terms in the decoupled system, such that the modeling error seems to be buried by the truncation errors and would be difficult to be distinguished from the overall error.

2.4 Conclusions

For general multi-oscillator systems including multi-machine power systems in the classical model, the NMD approach provides an approximate representation for stability analysis, i.e. a number of decoupled nonlinear one-degree-of-freedom oscillators. It is shown that the use of 3rd order TTE induces much conservative stability boundary compared to the original power system model. Moreover, using the decoupled system from 3rd order TTE, an even more conservative approximation of the stability boundary can be identified and the closest UEP can be approximated. This validates the use of NMD on power system TSA. Then, an NMD based TSA approach is proposed to analyze the transient stability of the multi-machine power systems. Each of the decoupled nonlinear oscillators can infer the transient stability of the original multi-machine power systems by using the Lyapunov function theory. Moreover, the most critical mode that could induce the instability can be identified. The proposed approach is validated on the simplified and detailed NPCC 140-bus power system. Test results show that the NMD based analysis has a potential to assess the transient stability and visualize the modal dynamics of multi-machine power systems.

The potential significant benefits from NMD include: (i) a rough estimation of transient stability boundary; (ii) an early warning of the oscillation mode that may most likely develop into a transient instability; (iii) visualization of the dynamics of a high-dimensional dynamical system in many low-dimensional coordinates for stability

monitoring purpose. Future works will investigate in detail the online applications of the proposed NMD methodology, early warning of transient instability and out-of-step protection, using a more efficient implementation and also the design of preventive and remedial control actions.

CHAPTER 3

DIRECT DAMPING FEEDBACK CONTROL FOR OSCILLATION

In this chapter, a direct damping feedback control method is proposed to eliminate the damping ratio deviation for a target mode by controlling the power converters based devices in the system. To reach the goal of measuring the damping ratio in real-time, a damping estimation approach is proposed, which is more accurate and robust for nonlinear oscillation and is insensitive to the length and starting point of the measuring time window. Using the proposed damping estimation approach and the power converter based devices in the system, a direct damping feedback control method is proposed using PI (proportional-integral) controller. The power system model together with the damping estimation algorithm is approximated by a transfer function in the control system. This approximation is enabled by *a*) representing the target mode as a single oscillator model which is obtained from model reduction via the NMD method, and *b*) considering the "zeroth-order" parametric resonance of the single oscillator model. Then, the parameters of the PI controller are determined by considering the trade-off between the requirements of robustness and control performance. Numerical studies on the 48-machine Northeast Power Coordinating Council system validate the effectiveness of the proposed damping control method.

3.1 Methodology

The proposed direct feedback control system is illustrated in Figure 20, including three modules: 1) a PI controller, 2) a low-pass filter, and 3) a power system module, where are described as follows:

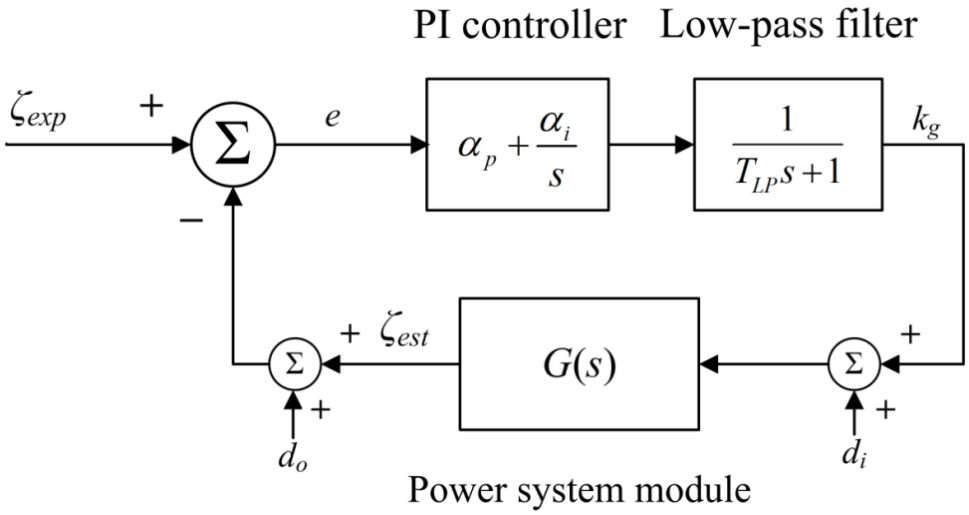

Figure 20. Diagram of Feedback Control System

1) PI controller is the core of the proposed control system, whose goal is to eliminate the error e between the real-time estimated damping ratio ζ_{est}, and the desired value ζ_{exp} for a target mode. Its parameters α_p and α_i are to be optimized considering both robustness and accuracy of damping control.

2) Low-pass filter provides a control signal k_g to the power converter of the energy storage device, which removes high frequency components in the PI controller output. As being shown later, the filter is to avoid exciting the nonlinear response of the power system module, such that the power system module could be approximated by a transfer function.

3) The power system module consists of two parts, the power system model and damping ratio estimation algorithm. The input is a control signal k_g and the output is the measured damping ratio ζ_{est}. This module will be approximated by a linear transfer function, say G(s), considering the "zeroth-order" parametric resonance. How to identify G(s) will be shown later.

In addition, the damping ratio cannot be estimated continuously, but discretely, in the practical application, e.g. estimated for every one second. Consequently, the control signal k_g is also changed discretely. Hence, two signals d_o and d_i are added in Figure 20 to represent such discontinuity. They act like disturbances for the system and might be a cause of instability. Two additional conditions are considered to cope with d_o and d_i. On one hand, impact of d_o and d_i should be reduced to avoid instability. On the other hand, it is expected to quickly stabilize the system. A procedure for designing a robust PI damping controller will be proposed to consider those two conditions and a unique

selection of α_p and α_i can be determined.

After the parameter α_p and α_i being determined, the whole control system will continuously operate in real time with the power system. The damping ratio can be measured using the ambient data from the load change or the ring down data from disturbances. When the damping ratio deviates from the expected value, the control system will change k_g to eliminate the deviations, and the control parameters of the converters **k** will also be changed accordingly.

3.2 Robust Damping Estimation Approach

For the purpose of direct damping feedback control, an accurate and robust feedback signal of estimated damping ratio is necessary. The measuring time window to meet the real-time performance needs to be short, e.g. 3-5 seconds, to reflect the variation of damping ratio in real-time. The estimation should be accurate when the response exhibits nonlinearity and when a differently short window length is used. The details of this approach will be given. The performance of this approach and other analysis are given in the Appendix A for the sake of brevity.

3.2.1 Methodology

The proposed damping estimation approach inherits the idea of NMD and fits post-disturbance measurements into a nonlinear oscillator for more robust estimation of oscillation damping, which is insensitive to the length and starting point of time window of measurements. It is assumed that rotor angles of all main generation units can be directly measured or estimated in a real-time and synchronous manner [57], [58]. The approach performs three steps: 1) linearly transforming rotor angle measurements into a

modal space for approximate modal decomposition; 2) fitting a nonlinear oscillator for the mode of interest, e.g. the dominant mode; 3) calculating the damping ratio from the oscillator. The methodology of the approach is, when a window of data is selected, those aforementioned three steps are implemented as follows:

Step 1 (modal decomposition): Use the decomposition transformation to extract the response of each mode from the state space response, especially the response of the target mode.

Step 2 (nonlinear oscillator fitting): Identify a 1-DOF nonlinear oscillator for the target mode from the mode response.

Step 3 (damping ratio estimation): Calculate the damping ratio from the identified coefficients of the nonlinear oscillator.

Those steps will be repeated when the next window of data is selected. This process can be automated for on-line and real-time application. The details of those steps will be given in the subsequent sections.

3.2.2 Modal Decomposition

The linear transformation for decomposing electromechanical modes can be obtained from linearization of the power grid model in the form of ordinary differential equations (2-1), which can consider detailed generator models with exciters and governors and equivalent impedance loads. The model parameters should be online updated to reflect the current topology and system condition of the grid.

$$\dot{\mathbf{X}} = \mathbf{f}(\mathbf{X}) \tag{2-1}$$

where $\mathbf{X}=[\delta, \Delta\omega, \ldots]^T$ is a $N\times1$ vector of system state variables, including rotor angles δ, speed deviations $\Delta\omega$, etc.. **f** governs the system dynamics.

Linearize **f**(**X**) at the stable equilibrium (SEP) to obtain

$$\Delta\dot{\mathbf{X}} = \mathbf{A}\Delta\mathbf{X} \tag{2-2}$$

where **A** is the Jacobian matrix.

Let $\Delta\delta$ be the difference between rotor angles δ and the SEP. The desired linear transformation to decouple the dynamics of rotor angles $\Delta\delta$, say **T**, can be obtained by the two steps a) and b) below.

a) Let $\mathbf{A}=\mathbf{L}\mathbf{\Lambda}\mathbf{L}^{-1}$, where $\mathbf{\Lambda}$ is a diagonal matrix of all eigenvalues and **L** is the corresponding modal matrix, whose rows are left eigenvectors. Then, define $\mathbf{Y}=\mathbf{L}\Delta\mathbf{X}$, which includes linearly transformed, decomposed state variables. Amongst $\mathbf{\Lambda}$, each conjugate complex pair of eigenvalues, say λ_i and λ_i^*, define one oscillation mode. If $\lambda_i = \sigma_i + jw_i$, the oscillation frequency $f_{osc,i}$ equals $w_i/2\pi$ and damping ratio ς_i is computed by (2-3). Assume that N_{osc} modes, i.e. N_{osc} pairs of eigenvalues, have $f_{osc,i}$ in 0.1-2 Hz. They are the modes of electromechanical oscillation (EO) of interests. Re-organize and divide the rows of **L** into $\mathbf{L}_{osc}$ and $\mathbf{L}_{rest}$ respectively corresponding to N_{osc} selected EO modes and the other modes as shown in (2-4).

$$\varsigma_i = \frac{-\sigma_i}{\sqrt{\sigma_i^2 + w_i^2}} \tag{2-3}$$

$$\mathbf{Y} = \begin{bmatrix} \mathbf{L}_{osc} \\ \mathbf{L}_{rest} \end{bmatrix} \Delta\mathbf{X} \tag{2-4}$$

Here, we assume that only rotor angles δ are directly measured by PMUs for online modal analysis. The proposed approach extracts the columns of $\mathbf{L}_{osc}$ that correspond to $\Delta\delta$ to make matrix $\mathbf{L}^{\delta}_{osc}$. Thus, define

$$\mathbf{Y}^{\delta}_{osc} = \mathbf{L}^{\delta}_{osc}\Delta\boldsymbol{\delta} \tag{2-5}$$

b) Real-valued decomposed state variables are preferred in terms of fitting, but $\mathbf{Y}^{\delta}_{osc}$ is complexed-valued due to the complex-valued $\mathbf{L}^{\delta}_{osc}$. Hence, instead of directly using $\mathbf{Y}^{\delta}_{osc}$, another transformation **P** is adopted [13] to obtain a set of real-valued decomposed state variables, say **Z**, as in (2-6).

$$\mathbf{Z} = \mathbf{P}\mathbf{Y}^{\delta}_{osc} = \mathbf{P}\mathbf{L}^{\delta}_{osc}\Delta\boldsymbol{\delta} = \mathbf{T}\Delta\boldsymbol{\delta} \tag{2-6}$$

$$\begin{cases} \mathbf{Z} = \left(\mathbf{z}_i\right)_{Nosc\times 1}, \quad \mathbf{z}_i = \left[\delta_{zi}, \omega_{zi}\right]^T \\ \mathbf{P} = diag\left(\begin{bmatrix} 1 & 1 \\ \lambda_i & \lambda_i^* \end{bmatrix}\right) \end{cases} \tag{2-7}$$

where **T** is the desired linear transformation to decouple the dynamics of the oscillation modes from $\Delta\delta$. **Z** contains real-valued linearly decomposed state pairs z_i. Note that $\dot{\delta}_{zi} = \omega_{zi}$, which makes z_i behaves like an oscillator, i.e. δ_{zi} behaves like an oscillator "angle" and ω_{zi} behaves like "speed".

Henceforth, **T** is used to decouple the time series measurements of $\Delta\delta$ to obtain a mode of interest, e.g. a dominant mode. One may note that if the SEP cannot be accurately obtained, the time series of $\Delta\delta$ and **Z** would contain some constant bias. This will be coped with by the mean centering technique and by assuming a fitting model with constant term as shown later in the nonlinear oscillator fitting approach.

3.2.3 Nonlinear Oscillator Fitting

Let $\{z[1],\ldots, z[K]\}$, where $z[k] = [\delta_z[k], \omega_z[k]]^T$, be the time series of a dominant mode, which oscillates around zero (if not, use techniques like mean centering to meet this requirement [59]). Since each pair z_i behaves like an oscillator as aforementioned, it is assumed that the time series can be fitted by the nonlinear fitting model (2-8), which is essentially a nonlinear oscillator of 1-DOF. The high-order polynomial term δ_{zi} represents the nonlinearity in the waveform of the dominant mode.

$$\ddot{\delta}_z + c_d\dot{\delta}_z + c_1\delta_z + \sum_{i=2}^{L} c_i\delta_z^i + c_0 = 0 \tag{2-8}$$

where c_d and c_i (i=0, …, L) are the unknowns to be estimated. The constant term c_0 is to allow the existence of constant bias in the time series of $\Delta\delta$ and **Z**. L is the highest polynomial order to be selected. A large L can usually give a better fitting since the model (2-8) has more freedom to accommodate the nonlinearity in system response, and it is recommended to be L = 30 based on the experimental results in this paper. $\dot{\delta}_z = \omega_z$, and the time series of $\ddot{\delta}_z$ can be numerically computed via that of $\dot{\delta}_z$, as in [60] and [61]. This oscillator has a stable equilibrium point (SEP), $\delta_{z,SEP}$.

Let **C**= $[c_d, c_0, \ldots, c_L]$, i.e. all the unknowns, $\mathbf{\Psi}_k$ = [$\dot{\delta}_z$ [k], 1, $\delta_z[k]$, $(\delta_z[k])^2$,…, $(\delta_z[k])^L]^T$, and $\boldsymbol{\xi}_k = \ddot{\delta}_z[k]$. Then, the estimation of **C** based on least square can be obtained by solving

$$\min_{\mathbf{C}} \quad Obj = \sum_{k=1}^{K}\left(\mathbf{C}\Psi_k + \boldsymbol{\xi}_k\right)^2 \tag{2-9}$$

The minimum of (2-9) is obtained when the derivative vector $\partial Obj/\partial\mathbf{C}$ is equal to zero, from which the optimal solution $\mathbf{C}_{opt}$ of (2-9) can be obtained by (2-10) and (2-11).

$$\mathbf{C}_{opt} = -\boldsymbol{v}\boldsymbol{u}^{-1} \tag{2-10}$$

$$\boldsymbol{u} = \sum_{k=1}^{K} \Psi_k \Psi_k^T, \quad \boldsymbol{v} = \sum_{k=1}^{K} \boldsymbol{\xi}_k \Psi_k^T \tag{2-11}$$

The derivation of (2-10) and (2-11) is given as follows.

The global optimal solution to reach the minimum of the least square problem (2-9) must satisfy a necessary condition as shown by (2-12).

$$\frac{\partial Obj}{\partial \mathbf{C}} = \left[\frac{dObj}{dC_1} \quad \frac{dObj}{dC_2} \quad \cdots \right] = 0 \tag{2-12}$$

Note that C_i denotes the ith entry in $\mathbf{C} = [c_d, c_0, \ldots, c_L]$. Each entry in (2-12) is calculated by:

$$\frac{dObj}{dC_i} = 2\sum_{k=1}^{K} \Psi_{k,i} \left(\mathbf{C}\Psi_k + \boldsymbol{\xi}_k \right) \tag{2-13}$$

where $\Psi_{k,i}$ is the ith entry in Ψ_k.

Since $(\mathbf{C}\Psi_k + \boldsymbol{\xi}_k)$ is a scalar, (2-12) can be rewritten as a compact form as (2-14).

$$\begin{aligned} \frac{\partial Obj}{\partial \mathbf{C}} &= 2\left(\sum_{k=1}^{K} \left(\mathbf{C}\Psi_k + \boldsymbol{\xi}_k \right) \Psi_k^T \right) \\ &= 2\left(\mathbf{C}\sum_{k=1}^{K} \Psi_k \Psi_k^T + \sum_{k=1}^{K} \boldsymbol{\xi}_k \Psi_k^T \right) \\ &= 2\left(\mathbf{C}\boldsymbol{u} + \boldsymbol{v} \right) = 0 \end{aligned} \tag{2-14}$$

where $\boldsymbol{u}$ and $\boldsymbol{v}$ are defined in (2-11). Since (2-14) has a unique solution, i.e. (2-15), it is also the global optimal solution that can reach the minimum of (2-9).

$$\mathbf{C}_{opt} = -\boldsymbol{v}\boldsymbol{u}^{-1} \tag{2-15}$$

3.2.4 Calculation of Damping Ratio

Shift the SEP of the oscillator (2-8) to the origin by replacing δ_z by $\hat{\delta}_z = \delta_z - \delta_{z,SEP}$. The resulting system is represented by (2-16).

$$\ddot{\hat{\delta}}_z + \hat{c}_d \dot{\hat{\delta}}_z + \hat{c}_1 \hat{\delta}_z + \sum_{i=2}^{L} \hat{c}_i \hat{\delta}_z^i = 0 \tag{2-16}$$

$$\lambda_{z1}, \lambda_{z2} = \sigma_z \pm j w_z = \frac{-\hat{c}_d}{2} \pm j \frac{\sqrt{4\hat{c}_1 - \hat{c}_d^2}}{2} \tag{2-17}$$

The first three terms actually constitute the linear counterpart of (2-16). The two eigenvalues of the characteristic equation of the linear counterpart can be solved by (2-17), say λ_{z1} and λ_{z2}. Here, assume $4\hat{c}_1 - \hat{c}_d^2 > 0$ so that λ_{z1} and λ_{z2} are a conjugate pair. The damping ratio ς_z and the oscillation frequency f_z are calculated by (2-18).

$$\varsigma_z = \frac{-\sigma_z}{\sqrt{\sigma_z^{\,2} + w_z^{\,2}}} = \frac{\hat{c}_d}{2\hat{c}_1}, \qquad f_z = \frac{w_z}{2\pi} = \frac{\sqrt{4\hat{c}_1 - \hat{c}_d^2}}{4\pi} \tag{2-18}$$

3.3 Transfer Function of Power System Module

In this section, a single oscillator model representing the target mode is obtained by model reduction via the NMD method or alternatively normal form theory. The impact of the converters on the single oscillator model is considered via the eigenvalue sensitivity. Then, together with the damping ratio estimation algorithm, a transfer function is identified for the power system module using the parametric resonance.

3.3.1 Model Reduction: Single Oscillator Model

Without loss of generality, only the active power outputs of converters are considered here. The same derivation process can be immediately applied if the reactive power outputs are considered.

Consider the active power output variation of the power converters $\Delta\mathbf{P}_C$ follows the control rule below.

$$\Delta\mathbf{P}_C = diag(\mathbf{k})\Delta\boldsymbol{\omega}_C \tag{2-19}$$

where *diag*(•) is the operator to convert the vector inside to a diagonal matrix. **k** is the control parameter of the converters, and $\Delta\boldsymbol{\omega}_C$ is the bus frequency of the converters. This control rule is based on the fact that the dynamics of the converters are much faster than that of the electromechanical dynamics.

The impact of $\Delta\mathbf{P}_C$ on the electrical power of the generators, $\Delta\mathbf{P}_e$, is mainly considered. The part of ODEs that is directly related to $\Delta\mathbf{P}_e$ is expressed by (2-20) in the linearized form.

$$diag(2\mathbf{H})\Delta\dot{\boldsymbol{\omega}} = \Delta\mathbf{P}_m - \Delta\mathbf{P}_e - diag(\mathbf{D})\Delta\boldsymbol{\omega} \tag{2-20}$$

where **H**, **D**, $\mathbf{P}_m$, and $\mathbf{P}_e$ are the vectors of inertia, damping coefficient, mechanical power, and electrical power of the generators, respectively.

By linearization and Kron reduction techniques [62], $\Delta\mathbf{P}_e$ can be expressed by:

$$\Delta\mathbf{P}_e = \kappa_1\Delta\mathbf{E}'_d + \kappa_2\Delta\mathbf{E}'_q + \kappa_3\Delta\mathbf{P}_C \tag{2-21}$$

where $\mathbf{E}'_d$ and $\mathbf{E}'_q$ are the transient voltage along the *d* and *q* axis, respectively. κ_i is the resulting coefficient matrix. Substitute (2-19) and (2-21) into (2-20):

$$diag(2\mathbf{H})\Delta\dot{\boldsymbol{\omega}} = \Delta\mathbf{P}_m - \kappa_1\Delta\mathbf{E}'_x - \kappa_2\Delta\mathbf{E}'_y - \kappa_3 diag(\mathbf{k})\Delta\boldsymbol{\omega}_C - diag(\mathbf{D})\Delta\boldsymbol{\omega} \tag{2-22}$$

The bus frequency deviation $\Delta\boldsymbol{\omega}_C$ could be approximated by a linear function of $\Delta\boldsymbol{\omega}$, which could simplify the analysis. By Kron reduction techniques, the network equations could be obtained which only consider the generator buses and converter buses:

$$\begin{bmatrix}\mathbf{I}_G\\ \mathbf{I}_C\end{bmatrix}=\begin{bmatrix}\mathbf{Y}_{GG} & \mathbf{Y}_{GC}\\ \mathbf{Y}_{CG} & \mathbf{Y}_{CC}\end{bmatrix}\begin{bmatrix}\mathbf{V}_G\\ \mathbf{V}_C\end{bmatrix} \tag{2-23}$$

where **I**, **V**, and **Y** are the current injection phasor, node voltage phasor, and the network impedance. The subscript "*G*" denotes the generator terminal buses, and "*C*" denotes the buses with controllable converters. Each V_i can be expressed in the polar coordinates $V_i = |V_i|e^{j\theta_i}$. For the generator buses, (2-24) holds, where δ_j is the rotor angle and θ_{Gdqj} is the phase angle in the rotating *d-q* coordinates.

$$\theta_{Gj} = \delta_j - \frac{\pi}{2} + \theta_{Gdqj} \tag{2-24}$$

The active power balance equations at the converter buses are computed by (2-25), where Re(·) is the operator to extract the real part.

$$\mathbf{P}_C = \mathrm{Re}\left(diag(\mathbf{V}_C)\left(\mathbf{Y}_{CG}^{*}\mathbf{V}_G^{*} + \mathbf{Y}_{CC}^{*}\mathbf{V}_C^{*}\right)\right) \tag{2-25}$$

Considering (2-24) and the assumptions listed below, eq. (2-26) can be derived from (2-25).

a) All the conductances are omitted, i.e. $\mathbf{G}_{CG} = 0$ and $\mathbf{G}_{CC} = 0$;

b) $\sin(\theta_{Ci} - \theta_{Gj}) \approx \theta_{Ci} - \theta_{Gj}$ and $\sin(\theta_{Ci} - \theta_{Cj}) \approx \theta_{Ci} - \theta_{Cj}$;

c) $|V_{Ci}| = |V_{Gi}| \approx 1$;

d) $\dot{\theta}_{Gdqi} = 0$.

$$\begin{aligned}\dot{\mathbf{P}}_C &= \mathbf{B}_{CC}\dot{\boldsymbol{\theta}}_C - \mathbf{B}_{CG}\dot{\boldsymbol{\delta}}\\ &\Downarrow\\ \Delta\dot{\mathbf{P}}_C &= \mathbf{B}_{CC}\Delta\boldsymbol{\omega}_C - \mathbf{B}_{CG}\Delta\boldsymbol{\omega}\end{aligned} \tag{2-26}$$

where $\mathbf{B}_{CC}$ and $\mathbf{B}_{CG}$ are susceptance matrices.

If further assume $\Delta\dot{\mathbf{P}}_C$ is negligible, (2-26) becomes (2-27).

$$\Delta\boldsymbol{\omega}_C = \mathbf{B}_{CC}^{-1}\mathbf{B}_{CG}\Delta\boldsymbol{\omega} \tag{2-27}$$

An alternative way to derive the function between $\Delta\boldsymbol{\omega}$ and $\Delta\boldsymbol{\omega}_C$ is introduced in [63], named as frequency divider, which is similar to (2-27) but the local load changes are not considered during the derivation.

Substitute (2-27) into (2-22) :

$$diag(2\mathbf{H})\Delta\dot{\boldsymbol{\omega}} = \Delta\mathbf{P}_m - \kappa_1\Delta\mathbf{E}'_x - \kappa_2\Delta\mathbf{E}'_y - \left(\kappa_3 diag(\mathbf{k})\mathbf{B}_{CC}^{-1}\mathbf{B}_{CG} - diag(\mathbf{D})\right)\Delta\boldsymbol{\omega} \tag{2-28}$$

Let the complete linearized power system ODE be (2-29) with (2-28) being included. $\Delta\mathbf{X}$ is the vector of the system states.

$$\Delta\dot{\mathbf{X}} = \mathbf{A}\Delta\mathbf{X} \tag{2-29}$$

The NMD method could be viewed as a model reduction technique that can decouple (2-29) and obtain a set of independent 1-DOF oscillators, with each one representing an oscillation mode. Normal form theory could also be used to reach this goal since it is essentially equivalent to the NMD method when facing linear ODEs. Let δ_{zi} and ω_{zi} be a pair of states corresponding to an oscillation mode and $\mathbf{Z}$ includes all the δ_{zi} and ω_{zi}. Note that δ_{zi} and ω_{zi} are analogous to the "angle" and "speed", respectively. The NMD transformation can be expressed by

$$\mathbf{Z} = \mathbf{T}_h\mathbf{X} \tag{2-30}$$

Note that it is a linear transformation since (2-29) is linear ODEs. $\mathbf{T}_h$ is a square matrix. The form of the independent 1-DOF oscillator of each mode can be generalized by:

$$\begin{bmatrix}\dot{\delta}_{zi}\\ \dot{\omega}_{zi}\end{bmatrix} = \begin{bmatrix}0 & 1\\ -\sigma_i^2 - w_i^2 & 2\sigma_i\end{bmatrix}\begin{bmatrix}\delta_{zi}\\ \omega_{zi}\end{bmatrix} \tag{2-31}$$

or equivalently:

$$\ddot{\delta}_{zi} + 2\zeta_i \omega_{ni} \dot{\delta}_{zi} + \omega_{ni}^2 \delta_{zi} = 0 \tag{2-32}$$

where $\lambda_{i1,2} = \sigma_i \pm jw_i$ are a conjugate pair of eigenvalues of (2-32) and are also part of the eigenvalues of **A**. ζ_i is the damping ratio and ω_{ni} is the natural frequency.

$$\zeta_i = -\frac{\sigma_i}{\omega_{ni}}, \quad \omega_{ni} = \sqrt{\sigma_i^2 + w_i^2} \tag{2-33}$$

If (2-32) corresponds to the target mode, it is a single oscillator model of the power system regarding the target mode. The change of $\lambda_{i1,2} = \sigma_i \pm jw_i$ regarding the parameter **k** can be approximated by:

$$\Delta\sigma_i + j\Delta w_i = \sum_j \frac{\partial \sigma_i}{\partial k_j} k_j + j \sum_j \frac{\partial w_i}{\partial k_j} k_j \tag{2-34}$$

The sensitivity $\partial\sigma_i/\partial k_j$ and $\partial w_i/\partial k_j$ can be calculated by (2-35) [62].

$$\frac{\partial \sigma_i}{\partial k_j} + j \frac{\partial w_i}{\partial k_j} = \sum_m \sum_n \left(\frac{\partial \sigma_i}{\partial a_{mn}} + j \frac{\partial w_i}{\partial a_{mn}} \right) = \sum_m \sum_n L_{im} R_{ni} \frac{\partial a_{mn}}{\partial k_j} \tag{2-35}$$

where L_{im} is the entry of the left eigenvector at row i and column m, and R_{ni} is the entry of the right eigenvector at row n and column i. $\partial a_{mn}/\partial k_j$ is the sensitivity of each entry a_{mn} in **A** regarding each k_j in **k**.

Two assumptions are taken before considering $\Delta\sigma_i$ and Δw_i in (2-32). First, assume $\partial w_i/\partial k_s \approx 0$ and $\Delta w_i \approx 0$ since usually $\partial w_i/\partial k_j << \partial\sigma_i/\partial k_j$ and $\Delta w_i << w_i$. Second, ω_{ni} is assumed to remain unchanged since $\Delta\sigma_i << \omega_{ni}$. Hence, (2-32) becomes:

$$\ddot{\delta}_{zi} + \left(2\zeta_i \omega_{ni} + k_g\right) \dot{\delta}_{zi} + \omega_{ni}^2 \delta_{zi} = 0 \tag{2-36}$$

$$k_g = -2\Delta\sigma_i = -2 \sum_j \frac{\partial \sigma_i}{\partial k_j} k_j \tag{2-37}$$

Eq. (2-36) is the reduced-order model representing the target mode with the parameter **k** being considered. Note that k_g is considered as a control signal. When the control signal is given, **k** only needs to be changed to meet (2-37). The sensitivity $\partial\sigma_i/\partial k_j$ can be used as a criterion to rank the effectiveness of each converter. Only the converter with the largest $\partial\sigma_i/\partial k_j$ is the best candidate for damping control service unless it reaches its limit and then a second candidate converter has to be used.

3.3.2 Transfer function

Using the single oscillator model and the previously proposed damping estimation approach, the diagram of the power system module is shown in Figure 21. This module is essentially nonlinear. Moreover, a certain type of the signal k_g will excite parametric resonance in the response of δ_{zi} as shown in the Appendix A and B, which makes it even more complicated to control.

If k_g is a sinusoidal signal, say $k_g = K\cos(\Omega t)$ where K is the amplitude and Ω is the frequency, the conclusions of the parametric resonance can be stated as follows. The principal parametric resonance in Appendix A states that if $\Omega \approx 2w_i$, the waveform of δ_{zi} exhibits either a periodic changed damping of which the frequency of that periodicity is close to $\sqrt{\left|(\Omega-2w)^2-K^2/4\right|}$, or simply a time-variant damping. On the other hand, the "zeroth-order" parametric resonance in Appendix B states that if $\Omega \approx 0$, the waveform of δ_{zi} shows a periodic varied damping and the frequency of that periodicity is close to Ω.

To approximate the power system module by a transfer function, the "zeroth-order" parametric resonance is utilized. Since the frequency of output signal ζ_{est} will be very close to the frequency of the input signal k_g under "zeroth-order" parametric

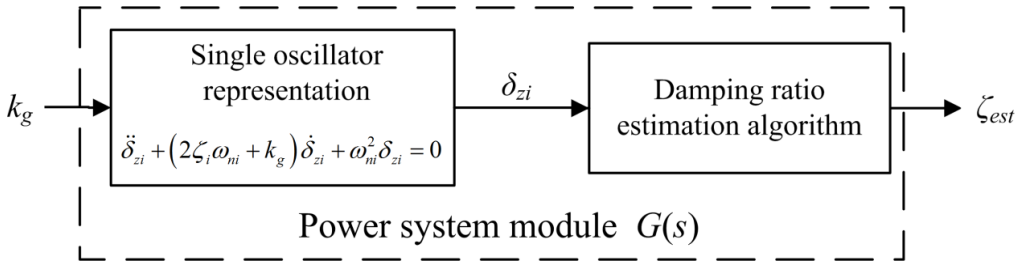

Figure 21. Diagram of the power system module

resonance, it makes the module behaves like a linear transfer function.

To obtain the transfer function $G(s)$, one modification is the use of a low-pass filter to reduce the high frequency components in k_g. Let the cut-off frequency of the filter be w_{cut}. Then, the frequency-response characteristics of the power system module within a small frequency domain surrounding 0 rad/s is measured, through which $G(s)$ can be estimated. The frequency-response characteristics can be obtained as follows. Given a frequency domain, say [0, ω_{cut}], densely select a set of frequencies within the domain. At each frequency ω_p, feed a harmonic signal of single frequency ω_p and amplitude one into a system and measure the output. The relative variation in the magnitude and phase angle of the output relative to the input can be viewed as an approximation of $|G(j\omega_p)|\angle G(j\omega_p)$. When the relative variations at all the frequencies are known, $G(s)$ can be identified via transfer function estimate from experimental data, like the function *tfest*() in MATLAB.

3.4 Robust PI Controller

There are many different ways to tune the PI controller. Following the principles in [64], the all stabilizing parameter domain is defined as a domain within which any selection of the parameters α_p and α_i can stabilize the system. Following the PI stabilization method in [64], when d_o and d_i are assumed to be zero, the all stabilizing parameter domain can be analytically determined within which there exist infinitely many selections of α_p and α_i.

More conditions need to be considered to obtain a unique selection. Here, the methodology of [65] is followed to uniquely determine α_p and α_i by considering the robustness and control performance of the PI controller.

The robustness considers the impact of d_o and d_i on the estimated damping ratio ζ_{est}. The following relationship can be derived:

$$\zeta_{est}(s) = T(s)\zeta_{exp}(s) + S(s)G_c(s)d_i(s) - T(s)d_0(s) \tag{2-38}$$

$$\begin{cases} G_c(s) = \dfrac{G(s)}{T_{LP}s+1}, & C(s) = \alpha_p + \dfrac{\alpha_i}{s} \\ S(s) = \dfrac{1}{1+G_c(s)C(s)}, & T(s) = \dfrac{G_c(s)C(s)}{1+G_c(s)C(s)} \end{cases} \tag{2-39}$$

where $S(s)$ and $T(s)$ are the sensitivity function and complementary sensitivity function, respectively. $S(s)$ should be minimized over the frequency domain to reduce the impact of d_i, while $T(s)$ should be minimized over the frequency domain to minimize the impact of d_o. Hence, set the robustness measure as (2-40). As indicated in [65], the reasonable values M_{st} are in a range between 1.2 and 2. A smaller M_{st} indicates better robustness.

$$M_{st} = \max_{\omega}(|S(j\omega)|, |T(j\omega)|), \qquad \forall \omega \in \mathbb{R} \tag{2-40}$$

The control performance is characterized by the integrated absolute error (IAE) defined in (2-41). A smaller *IAE* indicates faster stabilization of a perturbed system.

$$IAE = \int_0^{\infty} |e(t)|\, dt \tag{2-41}$$

where e is the control error after a disturbance like a step change in the reference ζ_{exp}.

Based on the conclusion of [65], it is not always possible to find a selection that can both minimize M_{st} and *IAE*. By depicting the contours of M_{st} and *IAE* within the all stabilizing parameter domain, there exists a trade-off curve between the optimums of M_{st}

and *IAE* along which every point is Pareto optimal. The trade-off curve can be numerically obtained by minimizing *IAE* for a set of fixed M_{st}. One way to uniquely determine α_p and α_i is to first determine a target M_{st}, and then, find the optimal value minimizing *IAE*. The problem is formulated as:

$$\begin{aligned} \min_{[\alpha_p,\alpha_i]\in\Theta} \quad & IAE \\ s.t. \quad & M_{st} = M_{st,tar} \end{aligned} \tag{2-42}$$

where Θ denotes the all stabilizing parameter domain, and $M_{st,tar}$ is the target value.

3.5 Case Studies on NPCC system

The NPCC system is used to illustrate the design procedure of the proposed method, and validate the effectiveness in a practical scenario.

3.5.1 Control System Design

The proposed design procedure is investigated in detail through the implementation on an NPCC 140-bus system. The system is changed a little for the case studies. A line is added between buses 7 and 13, with the impedance to be *j*0.0028 (pu). The damping coefficients are set to be 1.21 times the original value.

The 0.62 Hz inter-area mode is selected for designing the damping control. The diagram is the same as in Figure 17 except that one line is added between bus 13 and bus 7. The information related to this target mode from linearized model based small signal analysis is given in Table 11. The expected damping ratio is ζ_{exp} = 3%. The buses 1 and 23 are assumed to have power converter based devices that can provide damping control service. For each bus, $0 \le k_j \le 200$. According to the sensitivity $\partial\sigma_i/\partial k_j$, bus 23 is the better one for damping control.

Table 11. Target Mode for Control System Design

Frequency (Hz)	**Eigenvalue**	**Damping ratio (%)**
0.62	$-0.1175 \pm 3.8872i$	3.02

The single oscillator model for the target mode is given in (2-43).

$$\ddot{\delta}_z + \left(0.2348 + k_g\right)\dot{\delta}_{zi} + 15.1243\delta_{zi} = 0 \tag{2-43}$$

The transfer function $G(s)$ is given in (2-44). Note that ω_{cut} = 2π×0.3 rad/s is selected to meet the assumption of "zeroth-order" parametric resonance.

$$G(s) = \frac{0.665s^2 - 0.140s + 3.602}{s^3 + 3.338s^2 + 5.788s + 3.975} \tag{2-44}$$

The cut-off frequency of the low-pass filter is also set as ω_{cut} = 2π×0.3 rad/s, i.e. $T_{LP} = 1/\omega_{cut} = 0.53$. $G_c(s)$, $S(s)$ and $T(s)$ are determined as follows.

$$\begin{cases} G_c(s) = \dfrac{0.665s^2 - 0.140s + 3.602}{0.531s^4 + 2.772s^3 + 6.411s^2 + 7.899s + 3.975} \\ S(s) = \dfrac{s(0.531s+1)(s^3 + 3.338s^2 + 5.788s + 3.975)}{Don(s)} \\ T(s) = \dfrac{0.665\alpha_p s^3 + (-0.140\alpha_p + 0.665\alpha_i)s^2 + (3.602\alpha_p - 0.140\alpha_i)s + 3.602\alpha_i}{Don(s)} \\ Don(s) = 0.531s^4 + (2.772 + 0.665\alpha_p)s^3 + (6.411 - 0.140\alpha_p + 0.665\alpha_i)s^2 \\ \qquad + (7.899 + 3.602\alpha_p - 0.140\alpha_i)s + 3.975 + 3.602\alpha_i \end{cases} \tag{2-45}$$

Now, only the parameters of the PI controller need to be determined. Using the method in [64], the all stabilizing parameter domain is depicted in Figure 22, marked by the white area. The contours of M_{st} and the optimum M^*_{st} are depicted in Figure 23. The contours of *IAE* and the optimum IAE^* are depicted in Figure 24. Trade-off between M_{st} and *IAE* can be easily observed by comparing their contours, as shown in Figure 25. The trade-off curve corresponds to $1 \le M_{st} \le 1.75$ and $2.15 \le IAE \le 82.71$.

To show if the control model in Figure 20 could properly reflect the control performance exhibited in the power system simulation, consider a step function as the input to the control model and the power system simulation and the responses of the

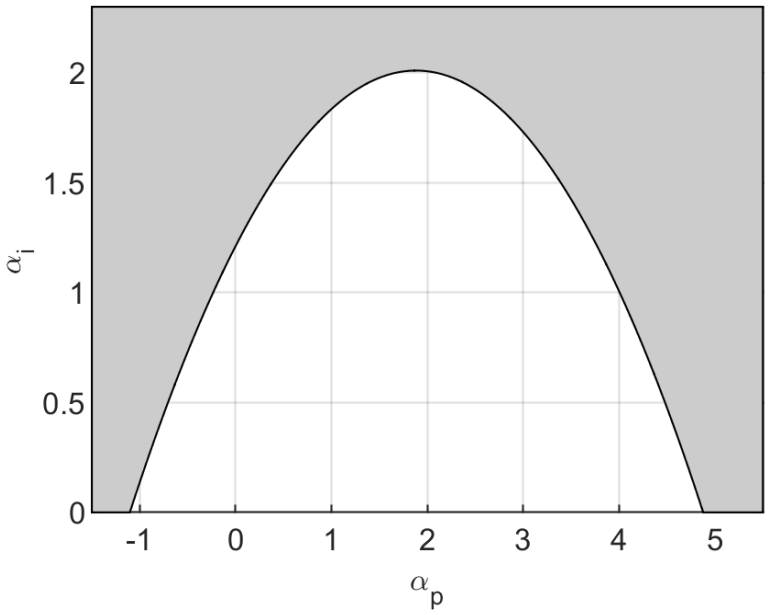

Figure 22. All stabilizing parameter domain.

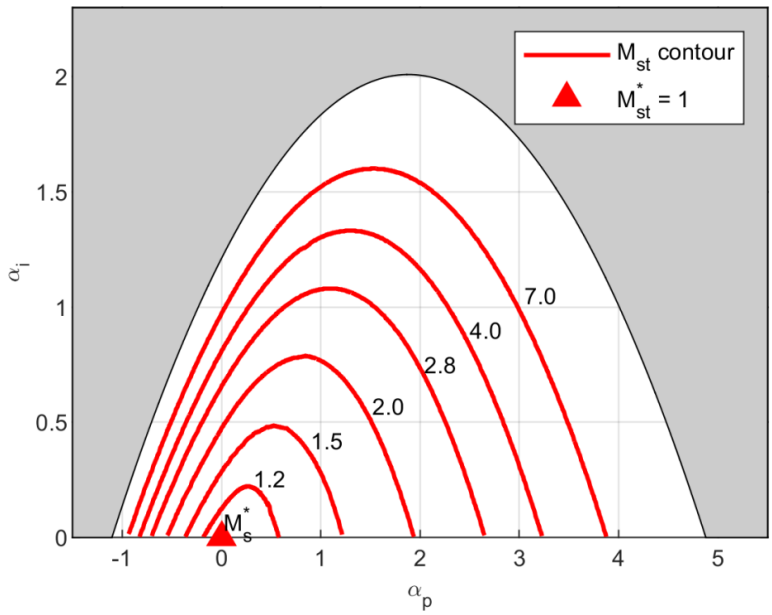

Figure 23. Contours and optimum of M_{st}.

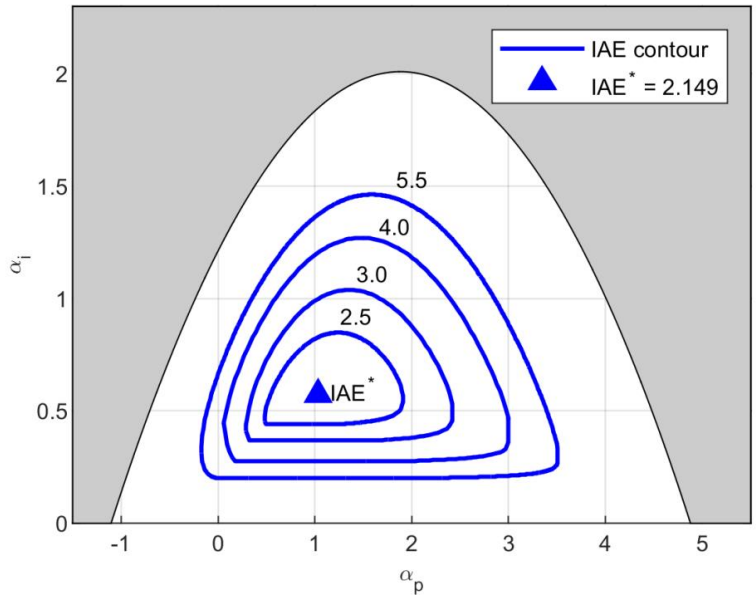

Figure 24. Contours and optimum of *IAE*.

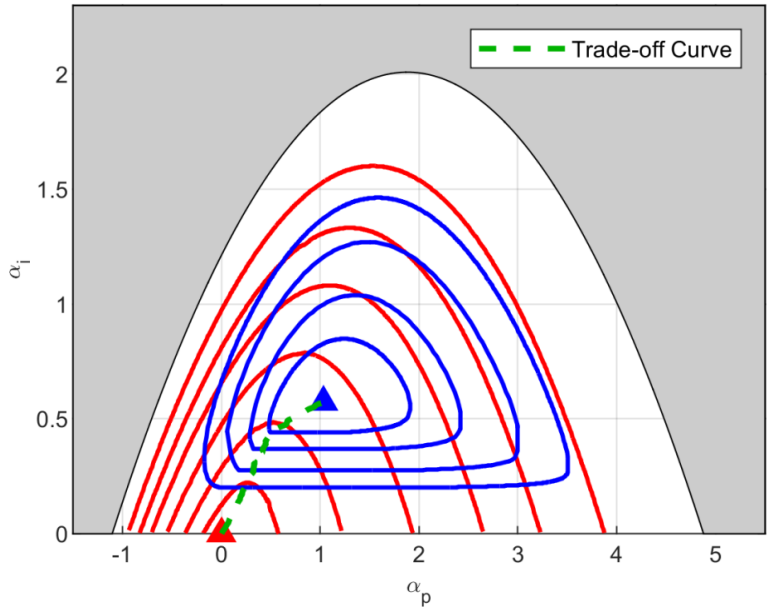

Figure 25. Trade-off curve.

damping ratio are compared. The specific configuration of control model and power system simulation is set as below.

1) Control model: the initial value of ζ_{exp} is set to be 0.92%. Then, after one second, ζ_{exp} is immediately changed to 3%.

2) Power system model: first deactivate the damping control. The rotor angle oscillation in the power system simulation is excited by a permanent three-phase fault added at bus 13 and cleared after 0.125s by disconnecting the line 13-7. Note that the damping ratio of the target mode drops to 0.92% in the post-fault system. Then, the damping control is reactivated after the first several seconds and ζ_{exp} is set as 3%.

For the power system model case, the first several seconds are skipped to avoid including the response from the fault-on system, which could hardly be handled by any damping ratio estimation methods. Another reason is that, the control model is based on a linearized power system model. For the purpose of test, the data of the first several seconds that exhibits nonlinearity are skipped and the subsequent data is used which is close to sinusoidal response. How to handle the data in first several seconds is discussed in the next section.

Three points on the trade-off curve, [0.3251, 0.3172], [0.6518, 0.4742] and [1.0557, 0.5623], are selected for [α_p, α_i], which are corresponding to [M_{st}, IAE] = [1.3, 3.479], [1.5, 2.333], and [1.75, 2.149], respectively. The comparison results are given in Figure 26, Figure 27 and Figure 28, respectively. For the sake of convenience, the responses of the damping ratio are realigned such that t = 0 s corresponds to the time instant of the step change.

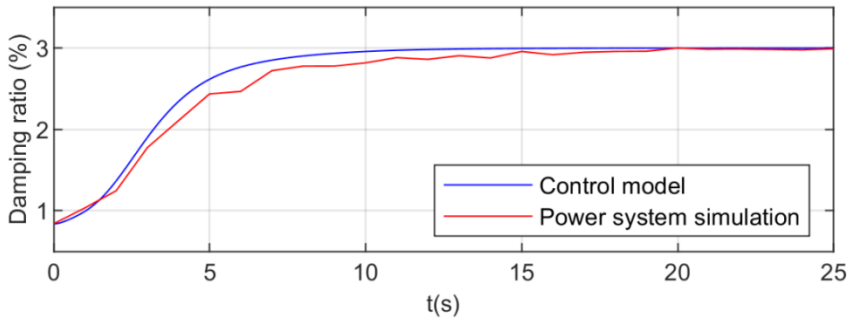

Figure 26. Comparison: [α_p, α_i] = [0.3251, 0.3172].

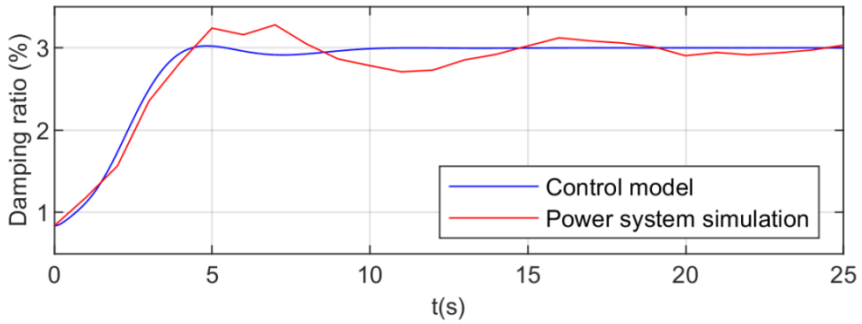

Figure 27. Comparison: [α_p, α_i] = [0.6518, 0.4742].

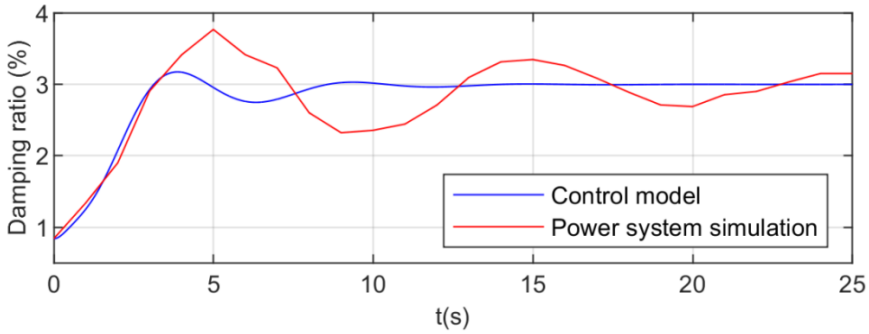

Figure 28. Comparison: [α_p, α_i] = [1.0557, 0.5623].

The results from the control model and the power system simulation agree well when M_{st} is small, and become less consistent when M_{st} becomes larger. Hence, it is recommended to set M_{st} to be a small value, such that the control model could properly reflect the practical scenario.

Finally, the case of $[\alpha_p, \alpha_i] = [1.0557, 0.5623]$ is used to show the accuracy of the approximation (2-27). The true $\Delta\boldsymbol{\omega}_C$ and the approximated $\Delta\boldsymbol{\omega}_C$ are compared for bus 1 and 23, and the results are shown in Figure 29. Note that there exists observable difference between the true $\Delta\boldsymbol{\omega}_C$ and the approximated $\Delta\boldsymbol{\omega}_C$ for bus 23, which might be caused by neglecting $\Delta\dot{\mathbf{P}}_C$ in (2-26). How to compensate such difference will be investigated in the future works.

3.5.2 Practical Scenario

In this section, a practical scenario is considered. Before t = 30 s, there is only ambient data caused by load change. At t = 30 s, a permanent three-phase fault is added at bus 13 and cleared at the critical clearing time (CCT), 0.125 s, or 0.5 CCT, 0.0625 s, by disconnecting the line 13-7. Three groups of parameters are selected for $[\alpha_p, \alpha_i]$, [0.3251, 0.3172], [0.6518, 0.4742] and [1.0557, 0.5623], which corresponds to $[M_{st}, IAE]$ = [1.3, 3.479], [1.5, 2.333], and [1.75, 2.149], respectively. Note that in this study the damping control is activated all the time.

As mentioned in the previous section, the data in the first several seconds after a large disturbance should be handled. On one hand, the response of fault-on system would be included in those data. Based on the experimental experience, damping ratio estimation on such data usually cannot identify an oscillation mode; actually, most of the

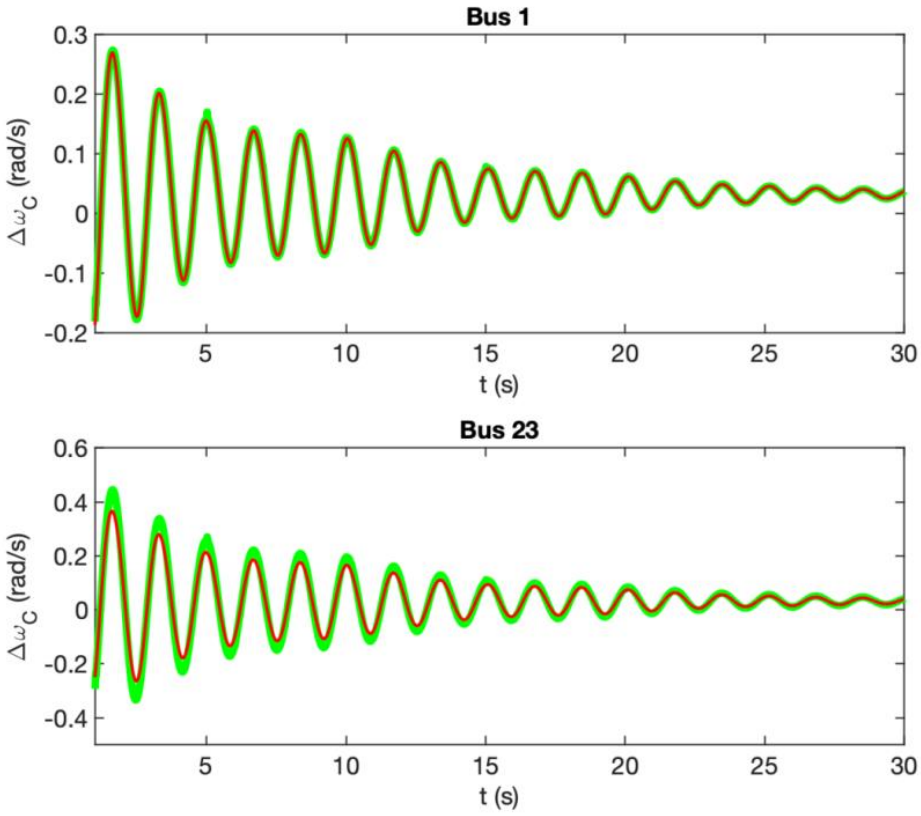

Figure 29. Comparison of true and approximated $\Delta\boldsymbol{\omega}_C$.

estimation algorithms would give a result of non-oscillation mode, i.e. a real eigenvalue. On the other hand, the response of the post-fault system could exhibit severe nonlinearity at the early stage, and a robust estimation method should be used to identify the accurate damping ratio. Two remedies are used to deal with those two issues.

1) When a real eigenvalue mode is identified, the current damping ratio result is set to be equal to the previous result. By doing this, the response of the fault-on system could be skipped.

2) The recently proposed nonlinear oscillator fitting based damping ratio estimation method are used to handle the nonlinearity at the early stage, which is shown to be more robust than the existing methods, and is insensitive to selection of the length of the measuring time window.

Note that the length of the measuring time window is selected as 3 seconds. The damping ratio is estimated and updated for every 0.5 second.

The comparisons of those three groups of parameters are given in Figure 30 when the fault is cleared at the CCT, and in Figure 31 when the fault is clear at 0.5 CCT. The results show that all the three groups of [α_p, α_i] can eliminate the damping ratio deviation. The comparison between 35 seconds and 50 seconds shows that a group of [α_p, α_i] with smaller *IAE* can eliminate the deviation much faster. For instance, in Figure 31, [α_p, α_i] = [1.0557, 0.5623] can be around 5 seconds ahead than [α_p, α_i] = [0.3251, 0.3172] to tune the damping ratio back to 3%.

Use Figure 30 to illustrate the variation of the measured damping ratio. At around 34 seconds, the measured damping ratio increases to over 5%. This increase is mainly

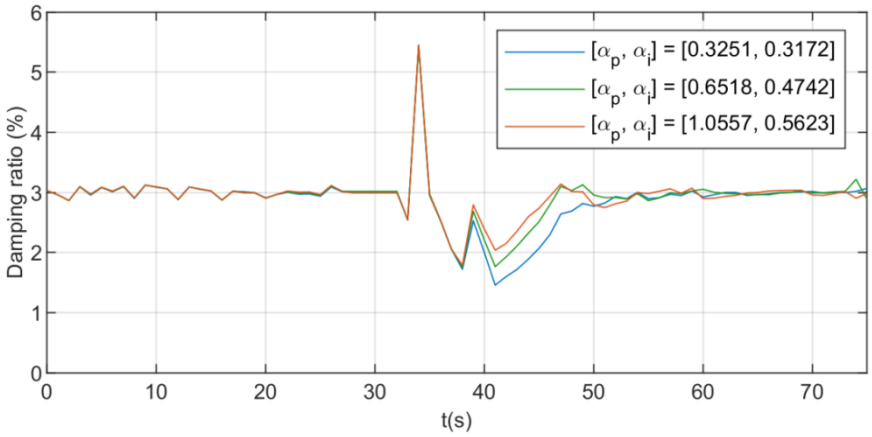

Figure 30. Damping control performance: fault cleared at CCT.

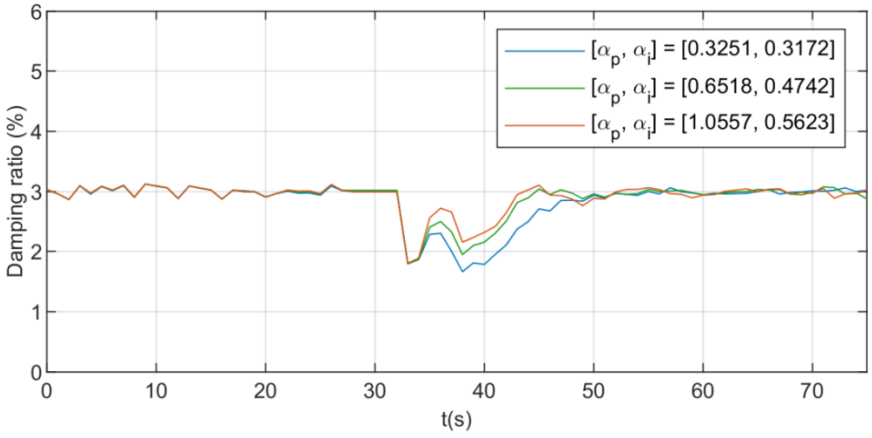

Figure 31. Damping control performance: fault cleared at 0.5CCT.

caused by the system nonlinear response. As investigated by the proposed damping estimation method in Appendix A, when fault is cleared at CCT, the modal response of the target mode could exhibit a large damping ratio at the early stage, and the measured damping ratio will also increase. It could also be observed that at around 39 seconds, there is an increase from less than 2% to almost 3%. This increase might be caused by the fact that, if the control signal k_g exhibits more complex dynamics than a sine wave, the system response would also be more complex and could exhibit unusual damping ratio. If such increase is viewed as part of disturbance d_i in Figure 20, one may want to enhance the robustness against such disturbance by selecting a small M_{st} when optimizing [α_p, α_i].

3.6 Conclusion

A feedback control method is proposed for direct damping control. The feedback control system is designed using PI controller. A single oscillator model representing the target mode is derived based on which the power system together with the damping estimation algorithm is approximated by a transfer function. The identification of this transfer function utilizes the parametric resonance. The optimal parameters of the PI controller are determined by considering the robustness and control performance. Simulation results on the 48-machine Northeast Power Coordinating Council system validate the effectiveness of the proposed damping controller.

Future works may include but not limited to: *a*) how to find a better approximation of $\Delta\boldsymbol{\omega}_C$ considering the derivative of $\Delta\mathbf{P}_C$, *b*) more advanced control techniques to model the control system and more effective control algorithm, and *c*) how

to better handle the response data of the large disturbance at the early stage such that the damping controller could contribute to transient stability.

CHAPTER 4

CONCLUSION AND RECOMMENDATIONS

4.1 Summary of Contributions

This work proposed an NMD based power system TSA (transient stability analysis) approach, a real-time damping estimation method on nonlinear electromechanical oscillation, and a new real-time damping controller to eliminate the damping ratio deviation of a target mode. Specifically, the contributions of this work can be briefly summarized into the following aspects.

- This works showed the necessity to consider nonlinear oscillations for more accurate stability assessment and more advanced stability control.
- It was shown that keeping the polynomial terms up to the 3^{rd}-order for the decoupled system from NMD is acceptable for the purpose of approximate or conservative transient stability analysis.
- An NMD based power system TSA approach was proposed that can reduce the analysis of the original high-dimensional system to individual analyses on decoupled nonlinear oscillators about a few selected critical modes. The most critical mode that could induce instability can also be identified.
- A robust and accurate real-time damping estimation approach on nonlinear electromechanical oscillation was proposed, which can utilize

complete post-disturbance data and is insensitive to the length and starting point of the measuring window.

- The power system module consists of power system model and damping estimation algorithm could be approximated by a transfer function via the "zeroth-order" parametric resonance.

- A PI controller based direct damping feedback control method was proposed that utilizes the power converters based devices to control the damping ratio of a target mode to a desired value, with the requirements of both robustness and control performance being considered.

4.2 Future Works

Investigations on nonlinear power system oscillations could provide more insight on the connection between the oscillation modes and instability, e.g. reveal the mechanism of how a poorly-damped oscillation mode induces the out-of-synchronism among the generators. More effective assessment tools and more complex control methods can be developed to benefit the system operation and protection.

As a continuation of the NMD based power system TSA approach, the application of NMD or other methods for power system stability control would be investigated in the future. It is worthwhile to develop advanced control measures regarding the most critical mode to avoid the instability.

In the proposed damping controller, the measurement data around the fault clearing time cannot contribute to the damping control since it is difficult to extract useful features of a target mode from those data. How to effective recognize the information of

the target mode deserves more studies such that those data could be utilized for the damping controller, and even for the control methods of transient stability. Besides, more complex controller could be considered for designing the direct damping feedback control, where the nonlinear nature of the power system module is fully considered.

LIST OF REFERENCES

[1] NERC, “1996 System Disturbances – Review of Selected 1996 Electric System Disturbances in North America,” Aug. 2002.

[2] U.S.-Canada Power System Outage Task Force, “Final Report on the August 14, 2003 Blackout in the United States and Canada: Causes and Recommendations,” Apr. 2004.

[3] B. V. Chirikov, “A universal instability of many-dimensional oscillator systems,” *Physics Reports*, vol.52, no.5, pp.263-379, 1979.

[4] Z. Bai, “Krylove subspace techniques for reduced-order modeling of large-scale dynamical systems,” *Applied Numerical Mathematics*, vol. 43, no. 1-2, pp. 9-44, Oct. 2002.

[5] S. K. Khaitan, “A survey of high-performance computing approaches in power systems,” *IEEE PES General Meeting*, Boston, 2016.

[6] V. Centeno, A. G. Phadke, A. Edris, J. Benton, M. Gaudi, and G. Michel, “An adaptive out-of-step relay for power system protection,” *IEEE Trans. Power Del.*, vol. 12, no. 1, pp. 61-71, Jan. 1997.

[7] C. Liu, M. Su, S. Tsay, and Y. Wang, “Application of a novel fuzzy neural network to real-time transient stability swings prediction based on synchronized phasor measurements,” *IEEE Trans. Power Syst.*, vol. 14, no. 2, pp. 685-692, May 1999.

[8] K. Sun, et al, “An online dynamic security assessment scheme using phasor measurements and decision trees,” *IEEE Trans. Power Syst.*, vol. 22, no. 4, pp. 1935-1943, Nov. 2007.

[9] J. Yan, C. Liu and U. Vaidya, “A PMU-based monitoring scheme for rotor angle stability,” *IEEE PES General Meeting*, San Diego, 2012.

[10] F. Bai, Y. Liu, Y. Liu, K. Sun, et al, “A measurement-based approach for power system instability early warning,” *Protection and Control of Modern Power Systems*, 2016.

[11] I. B. Yadykin, et al, "Characterization of power systems near their stability boundary by Lyapunov direct method," *IFAC Proceedings Volumes*, vol.47, no.3, pp.9087-9092, 2014.

[12] K. R. Padiyar, *Structure Preserving Energy Functions in Power Systems: Theory and Applications*, CRC Press, 2016.

[13] B. Wang, K. Sun and W. Kang, "Nonlinear Modal Decoupling of Multi-Oscillator Systems with Applications to Power Systems," *IEEE Access*, vol. 6, pp. 9201-9217, 2018.

[14] L.O. Chua, H. Kokubu, "Normal forms for nonlinear vector fields. I. Theory and algorithm," *IEEE Trans. Circuits Syst.*, vol.35, no.7, pp.863-880, July 1988.

[15] W. Kang and A. J. Krener, "Normal forms of nonlinear control systems," *Chaos in automatic control*, pp. 345-376, CRC Press, 2006.

[16] IEEE Task Force on Identification of Electromechanical Modes, "Identification of electromechanical modes in power systems," *Technical Report PES-TR15 (formerly TP462)*, June 2012.

[17] J. Hauer, et al, "Initial results in Prony analysis of power system response signals," *IEEE Trans. Power Syst.*, vol. 5, no. 1, pp. 80-89, Feb. 1990.

[18] N. Zhou, J. W. Pierre, D. J. Trudnowski, R. T. Guttromson, "Robust RLS methods for online estimation of power system electromechanical modes," *IEEE Trans. Power Syst.*, vol. 22, no. 3, pp. 1240–1249, Aug. 2007.

[19] J. F. Hauer, "Application of prony analysis to the determination of modal content and equivalent models for measured power system response," *IEEE Trans. Power Syst.*, vol. 6, no. 3, pp. 1062–1068, Aug. 1991.

[20] J. N. Juang, R. S. Pappa, "An eigensystem realization algorithm for modal parameter identification and model reduction," *J. Guidance, Control, Dynam.*, vol. 8, no. 5, pp. 620–627, Sep. 1985.

[21] Y. Hua, T. K. Sarkar, "Matrix pencil method for estimating parameters of exponentially damped/undamped sinusoids in noise," *IEEE Trans. Acoust., Speech, Signal Process.*, vol. 38, no. 5, pp. 814–824, May 1990.

[22] K. Poon, K. Lee, "Analysis of transient swings in large interconnected power systems by Fourier transformation," *IEEE Trans. Power Syst.*, vol. 3, no. 4, pp. 1573–1579, Nov. 1988.

[23] J. L. Rueda, C. A. Juarez, I. Erlich, "Wavelet-based analysis of power system low-frequency electromechanical oscillations," *IEEE Trans. Power Syst.*, vol. 26, pp. 1733–1743, 2011.

[24] N. E. Huang, et al, "The empirical mode decomposition and the Hilbert spectrum for nonlinear and nonstationary time series analysis," *Proc. R. Soc. London*, vol. 454, pp. 903–995, 1998.

[25] B. Wang, K. Sun, "Formulation and characterization of power system electromechanical oscillations," *IEEE Trans. Power Syst.*, vol. 31, no. 6, pp. 5082–5093, Nov. 2016.

[26] B. Wang, X. Su, K. Sun, "Properties of the frequency–amplitude curve," *IEEE Trans. Power Syst.*, vol. 32, no. 1, pp. 826–827, Jan. 2017.

[27] Vahidnia, G. Ledwich, E. W. Palmer, "Transient stability improvement through wide-area controlled SVCs," I*EEE Trans. Power Syst.*, vol. 31, no. 4, pp. 3082–3089, Jul. 2016.

[28] K. Y. Wang and M. L. Crow, "Power system voltage regulation via STATCOM internal nonlinear control," *IEEE Trans. Power Syst.*, vol. 26, no. 3, pp. 1252–1262, Aug. 2011.

[29] X. Zhang, K. Tomsovic, and A. Dimitrovski, "Optimal investment on series FACTS device considering contingencies," in *Proc. 48th North Amer. Power Symp.*, Denver, CO, USA, Sep. 2016.

[30] Y. Wang, J. Meng, X. Zhang, and L. Xu, "Control of PMSG-based wind turbines for system inertial response and power oscillation damping," *IEEE Trans. Sustain. Energy*, vol. 6, no. 2, pp. 565–574, Apr. 2015.

[31] Y. Liu, Y. Liu, J. R. Gracia and T. J. King, "Oscillation damping contributions of variable-speed wind generators in the Eastern Interconnection (EI)," *2014 IEEE PES General Meeting*, National Harbor, 2014.

[32] C. Loutan et al., "Demonstration of essential reliability services by a 300-MW solar photovoltaic power plant," Nat. Renewable Energy Lab., Golden, CO, USA, Tech. Rep. NREL/TP-5D00-67799, 2017.

[33] R. K. Varma and M. Akbari, "Simultaneous Fast Frequency Control and Power Oscillation Damping by Utilizing PV Solar System as PV-STATCOM," *IEEE Trans. Sustain. Energy*, vol. 11, no. 1, pp. 415-425, Jan. 2020.

[34] Y. Zhu, B. Wang, K. Sun, "Damping control for power systems using energy storage," *29th Chinese Control and Decision Conference*, Chongqing, 2017.

[35] Y. Zhu, C. Liu, B. Wang, and K. Sun, "Damping control for a taret oscillation mode using battery energy storage," *J. Modern Power Syst. Clean Energy*, vol. 6, pp. 833–845, 2018.

[36] Y. Zhu, C. Liu, K. Sun, D. Shi, and Z. Wang, “Optimization of battery energy storage to improve power system oscillation damping,” *IEEE Trans. Sustain. Energy*, vol. 10, no. 3, pp. 1015–1024, Jul. 2019.

[37] B. C. Pal et al., “Robust damping controller design in power systems with superconducting magnetic energy storage devices,” *IEEE Trans. Power Syst.*, vol. 15, no. 1, pp. 320–325, Feb. 2000.

[38] S. Y. Ruan, G. J. Li, B. T. Ooi, and Y. Z. Sun, “Power system damping from real and reactive power modulations of voltage source converter station,” *IET Gener. Transm. Distrib.*, vol. 2, no. 3, pp. 311–320, 2008.

[39] X. Sui, Y. Tang, H. He, and J. Wen, “Energy-storage-based low-frequency oscillation damping control using particle swarm optimization and heuristic dynamic programming,” *IEEE Trans. Power Syst.*, vol. 29, no. 5, pp. 2539–2548, Sep. 2014.

[40] K. Sun, J. Qi, W. Kang, "Power System Observability and Dynamic State Estimation for Stability Monitoring Using Synchrophasor Measurements,” *Control Engineering Practice*, vol. 53, pp. 160-172, Aug. 2016.

[41] B. Wang, X. Xu, K. Sun, "Power system transient stability analysis using high-order Taylor expansion systems," *Texas Power and Energy Conference*, College Station, 2019.

[42] X. Xu, C. Liu, K. Sun, “A holomorphic embedding method to solve unstable equilibrium points of power systems,” *IEEE Conf. Decision and Control (CDC)*, Miami Beach, Dec. 2018.

[43] T. Athay, R. Podmore, and S. Virmani, "A Practical Method for the Direct Analysis of Transient Stability," *IEEE Trans. Power App. Syst.*, vol. PAS-98, pp. 573-584, 1979.

[44] B. Wang, K. Sun, W. Kang, "Relative and mean motions of multi-machine power systems in classical model," *arXiv:1706.06226*, 2017.

[45] M. A. Pai, *Power System Stability*, New York: North-Holland Publishing Company, 1981.

[46] V. I. Zubov, *Methods of A.M. Lyapunov and their application*, Izdatel'stvo Leningradskogo Universiteta, 1961.

[47] S. Margolis and W. Vogt, "Control engineering applications of V. I. Zubov's construction procedure for Lyapunov functions," *IEEE Trans. Autom. Control*, vol.8, no.2, pp. 104-113, Apr 1963.

[48] A. K. De Sarkar, N. D. Rao, "Zubov's method and transient stability problems of power systems," *Proc. IEE*, vol.118, no.8, pp.1035-1040, Aug. 1971.

[49] Y. Yu, K. Vongsuriya, "Nonlinear power system stability study by Liapunov function and Zubov's method," *IEEE Trans. Power App. Syst.*, vol.pas-86, no.12, pp.1480-1485, 1967.

[50] R. Genesio, M. Tartaglia, A. Vicino, "On the estimation of asymptotic stability regins: state of the art and new proposals," *IEEE Trans. Autom. Control*, vol.ac-30, no.8, pp.747-755, 1985.

[51] S. Wiggins, *Introduction to Applied Nonlinear Dynamical Systems and Chaos*. New York, NY, USA: Springer-Verlag, 1990.

[52] V. I. Arnold, *Geometrical Methods in the Theory of Ordinary Differential Equations*. New York, NY, USA: Springer-Verlag, 1988.

[53] V. Vittal, et al, "Analysis of stressed power systems using normal forms," *Proc. IEEE Int. Symp. Circuits Syst.*, San Diego, May 1992.

[54] Z. Wang, Q. Huang, "A closed normal form solution under near-resonant modal interaction in power systems," *IEEE Trans. Power Syst.*, vol. 32, no. 6, pp. 4570-4578, Mar. 2017.

[55] J. Chow, G. Rogers, *User manual for power system toolbox*, version 3.0, 1991–2008.

[56] J. Qi, K. Sun, W. Kang, "Optimal PMU placement for power system dynamic state estimation by using empirical observability Gramian," *IEEE Trans. Power Syst.*, vol.30, no. 4, pp.2041-2054, 2015.

[57] J. Qi, K. Sun, J. Wang, H. Liu, "Dynamic state estimation for multimachine power system by unscented Kalman filter with enhanced numerical stability," *IEEE Trans. Smart Grid*, vol. 9, no. 2, pp. 1184–1196, Mar. 2018.

[58] E. Ghahremani, I. Kamwa, "Online state estimation of a synchronous generator using unscented Kalman filter from phasor measurements units," *IEEE Trans. Energy Convers.*, vol. 26, no. 4, pp. 1099–1108, Dec. 2011.

[59] J. Hox, M. Moerbeek, R. Van de Schoot, *Multilevel analysis: techniques and applications*, Routledge, 2017.

[60] D. Eberly, "Derivative approximation by finite differences," *Magic Software, Inc*, 2008.

[61] W. Ju, B. Wang, K. Sun, "Estimating transient stability margin regarding a dominant oscillation mode," *IEEE PES Powertech*, Milano, Italy, Jun. 2019.

[62] P. Kundur, *Power System Stability and Control*. New York: McGraw-Hill, 1994.

[63] F. Milano, Á. Ortega, "Frequency Divider," *IEEE Trans. Power Syst.*, vol. 32, no. 2, pp. 1493-1501, March 2017.

[64] G. J. Silva, A. Datta, S. P. Bhattacharyya, "PI Stabilization of Delay-Free Linear Time-Invariant Systems" in *PID controllers for time-delay systems*. Springer Science & Business Media, 2007.

[65] O. Garpinger, T. Hägglund, K. J. Åström K J, "Performance and robustness trade-offs in PID control", *Journal of Process Control*, vol. 24, no. 5, pp. 568-577, 2014.

[66] R. Leelaruji, L. Vanfretti, K. Uhlen, J.O. Gjerde, "Computing sensitivities from synchrophasor data for voltage stability monitoring and visualization," *Int. J. Electr. Energy Syst.*, vol. 25, no. 6, pp. 933-947, Jun. 2015.

[67] S. W. Smith. *The Scientist and Engineer's Guide to Digital Signal Processing*, California Technical Pub, 1997.

[68] R. E. Blake, "Basic Vibration Theory," in *Shock and Vibration Handbook*. New York, NY, USA: McGraw Hill, 1988.

[69] B. Wang, K. Sun, X. Xu, "Nonlinear modal decoupling based power system transient stability analysis," *IEEE Trans. Power Syst.*, vol. 34, no. 6, pp. 4889-4899, Jun. 2019.

[70] H. D. Chiang, *Direct Methods for Stability Analysis of Electric Power Systems: Theoretical Foundation, BCU Methodologies, and Applications*. Hoboken, NJ, USA: Wiley, 2011.

[71] H. D. Chiang, F. Wu, P. Varaiya, "Foundations of direct methods for power system transient stability analysis," *IEEE Trans. Circuits Syst.*, vol. 34, no. 2, pp. 160-173, Feb. 1987.

[72] L. D. Zavodney, A. H. Nayfeh, "The response of a single-degree-of-freedom system with quadratic and cubic non-linearities to a fundamental parametric resonance", *Journal of Sound and Vibration*, vol. 120, no. 1, pp. 63-93, 1988.

[73] L. D. Zavodney, A. H. Nayfeh, N. E. Sanchez, "The response of a single-degree-of-freedom system with quadratic and cubic non-linearities to a principal parametric resonance", *Journal of Sound and Vibration*, vol. 129, no. 3, pp. 417-442, 1989.

[74] J. K. Kevorkian, J. D. Cole, *Multiple scale and singular perturbation methods*. Springer Science & Business Media, 2012.

APPENDICES

APPENDIX A – Performance of Damping Estimation Approach

At the beginning, three factors that could affect the accuracy of damping estimation are introduced, i.e. measurement noises, limited coverage of PMU measurements, and existence of multiple dominant modes, and the corresponding suggestions to reduce their influences and ensure the estimation accuracy are also proposed. Then, the performance of the damping estimation approach is shown via case studies, with those three factors also investigated.

A.1 Influencing Factors on Damping Estimation

In the real-world application, some factors could influence the damping estimation and even worsen the accuracy of the result. Three factors are considered including measurement noises, limited coverage of measurements, and the existence of multiple dominant modes. For each factor, the corresponding suggestions is proposed and illustrated to reduce its impact and ensure the accuracy of damping estimation.

Measurement Noises

The noises in measurements can influence estimation accuracy, and thus data preprocessing is needed to screen out the noises in measurements before the estimation. The filter deployed in this paper is similar to the one used in [66], i.e. a low-pass (LP) filter plus a moving average (MA) filter as shown in Figure 32. In the LP filter, the high frequency noises are extracted by the HP filter, and then, they are removed out of the original measurements by subtraction. MA filter is used to make the filtered data smoother. The proposed approach will be applied to the filtered data afterwards.

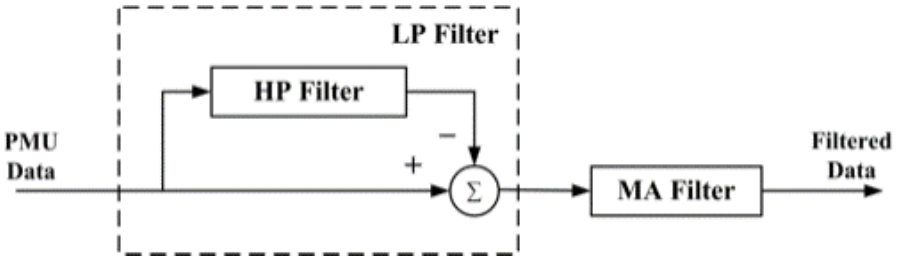

Figure 32. Schematic diagram of filter for preprocessing measurements.

Compared to an ordinary LP filter, the LP filter in Figure 32 can keep the low-frequency components less affected than a conventional LP filter when screening out high frequency noises [66]. The requirements for designing the inside HP filter can be found in [67]. The cut-off frequency of the HP filter is recommended to be 2.5Hz in this paper according to the frequency range of electromechanical modes.

Limited Coverage of PMU Measurements

For calculating the damping ratio of a dominant mode, the ideal situation is that all rotor angles of generators are available by either direct PMU measurements or dynamic state estimation. However, in reality, it could happen that not all rotor angles of generators are measurable by PMUs if either there are no PMUs installed on those generators, or some PMU measurements are not available temporarily due to communication interruption or PMU malfunctions. Thus, the influence of limited coverage of PMU measurements on the accuracy of damping estimation needs to be investigated.

In the case studies, the impact of missing PMU measurements on the estimation accuracy is investigated by assuming the measurements to be available for down to 85% of generators, e.g. 41 generators for the NPCC system. As later shown in the case studies, if a dominant mode is specified to be monitored during system oscillation, in order to ensure estimation accuracy on oscillation damping, it is recommended to guarantee the accessibility of the PMU measurements of the generators which have high observability of dominant mode.

Multiple Dominant Modes

Real-life oscillation events usually involve one dominant mode while the other modes are either insignificant in terms of amplitudes or the impacts on system stability, or do not sustain long. In some specific cases, however, there could be more than one mode that sustain together for a long time before one of them becomes dominant while the rest are damped out, of which the impact on estimation accuracy needs to be studied. Later in the case studies, the scenario with two dominant modes are created and studied on the NPCC 140-bus system, by an excitation technique based on the concept of normal mode [68] which is proposed to specifically excite some modes for power system by initializing the system with linearly scaled mode shape of interest (for short, LSMS): the system is initialized with zero angular velocities and the rotor angles are initialized at the linearly scaled mode shape about the modes of interests.

An index for modal energy is defined to evaluate the modal energy over a sliding time window, such that the energy variation of each mode can be investigated. Similarly define another linear transformation $\mathbf{Y}^{\omega}_{osc} = \mathbf{L}^{\omega}_{osc}\,\Delta\omega$ like in (2-5). Then, it is real-valued as in (A-1). Note that the matrix **P** here is the same as the one in (2-7). Thus, z_i and $\tilde{z}_i$ correspond to the same pair λ_i and λ_i^* of mode i.

$$\tilde{\mathbf{Z}} = \mathbf{P}\mathbf{Y}^{\omega}_{osc} = \mathbf{P}\mathbf{L}^{\omega}_{osc}\Delta\boldsymbol{\omega} = \mathbf{T}_{\omega}\Delta\boldsymbol{\omega} \tag{A-1}$$

$$\tilde{\mathbf{Z}} = \left(\tilde{\mathbf{z}}_i\right)_{Nosc\times 1},\ \ \tilde{\mathbf{z}}_i = \left[\tilde{\delta}_{zi}, \tilde{\omega}_{zi}\right]^T \tag{A-2}$$

Then, the index of modal energy E_i of an oscillation mode i can be computed over a sliding time window on the corresponding pair $\tilde{z}_i$, as (A-3) and (A-4). The modal

energy ratio of one mode to the entire modes is defined by (A-5) to evaluate the dominance of a mode.

$$\tilde{\boldsymbol{\omega}}_{z-i} = \mathbf{T}_{\omega-i}^{-1}\tilde{\mathbf{z}}_i \tag{A-3}$$

$$E_i = \frac{1}{T_{sl}}\int_{t_0}^{t_0+T_{sl}} \mathbf{H}\tilde{\boldsymbol{\omega}}_{z-i} \tag{A-4}$$

$$ER_i = \frac{E_i}{\sum E_i} \tag{A-5}$$

where $\mathbf{T}_{\omega\text{-}i}$ contains the columns in $\mathbf{T}_{\omega}$ that correspond to $\tilde{z}_i$, and the superscript "-1" denotes the pseudoinverse. **H** is the row vector of the generator inertia. t_0 is the initial time of the sliding time window, and T_{sl} is the length of the window. A sustained oscillation mode with high amplitude would have a relatively large value of ER_i compared to the fast damped-out or low amplitude modes. Such a mode will be a candidate for a dominant mode to be considered.

A.2 Case Study: IEEE 9-Bus System

The performance of the proposed approach is tested on the IEEE 9-bus system and compared with the Prony's method and the RLS method. The measurements are obtained from time-domain simulations under both small and large disturbances. The true value of damping ratio from the linearized model based eigen-analysis is computed by (2-3) and denoted by "True DR" in the figures. The Prony's method is implemented by the Prony tool with the TSAT software by Powertech Labs. The RLS method is implemented via the MATLAB function *recursiveAR*(), setting a 101st-order autoregressive (AR) model and a forgetting factor of 0.999. The model of IEEE 9-bus system is from [57], with classical generator model and constant impedance load

considered. The system diagram is the same as in chapter 2. The sampling rate is 30 samples per second.

A temporary three-phase fault is added at bus 5 and cleared at the CCT with the line 5-7 being disconnected. The 0.97 Hz oscillation mode is largely excited and hence selected for damping estimation. The dominance of the 0.97 Hz mode can also be verified by the spectrums from the response of two relative rotor angle differences, as shown in Figure 33. The information related to this dominant mode from linearized model based small signal analysis is given in Table 12.

Different lengths of sliding time windows are selected, i.e. 2 s, 2.5 s, 3 s, 3.5 s, 4 s. Order L = 10 is selected for the nonlinear oscillator model since its result is close to that of L = 30. The results are compared with that from the Prony's and RLS methods as shown in Figure 34, which validates the proposed approach for providing accurate and robust damping estimation. Note that the initial time instant of each sliding time window is used as the timestamp for the corresponding estimation. The damping ratio of the dominant mode estimated from the proposed approach is much less sensitive to the length of the sliding time window, which indicates the true damping of the mode in the sense of both small and large disturbances. Hence, compared with the Prony's method and RLS method, the proposed approach is more reliable for the first several large-amplitude swings following the large disturbance. Moreover, it has a high accuracy even with short time windows. Thus, the proposed approach has obvious advantages for real-time applications.

Table 12. Dominant Mode of IEEE 9-bus System

Frequency (Hz)	Eigenvalue	Damping ratio (%)
0.97	-0.100 - 6.089*i*	1.642

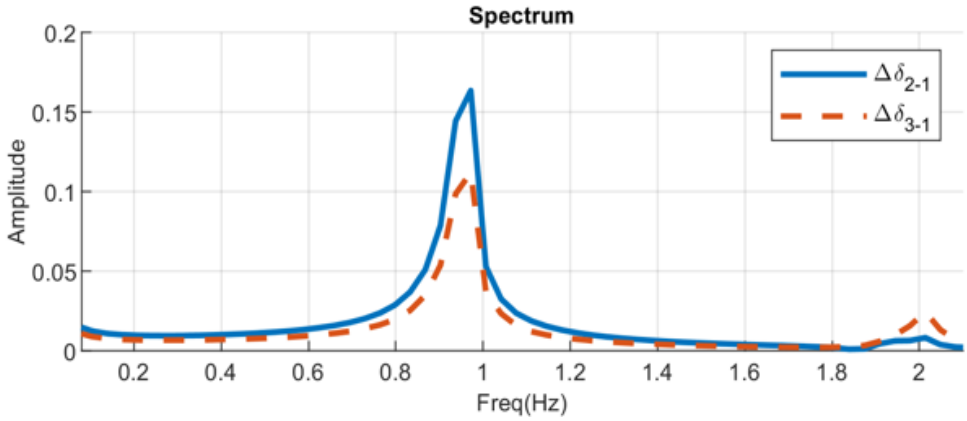

Figure 33. IEEE 9-bus system: spectrums when the fault cleared at CCT.

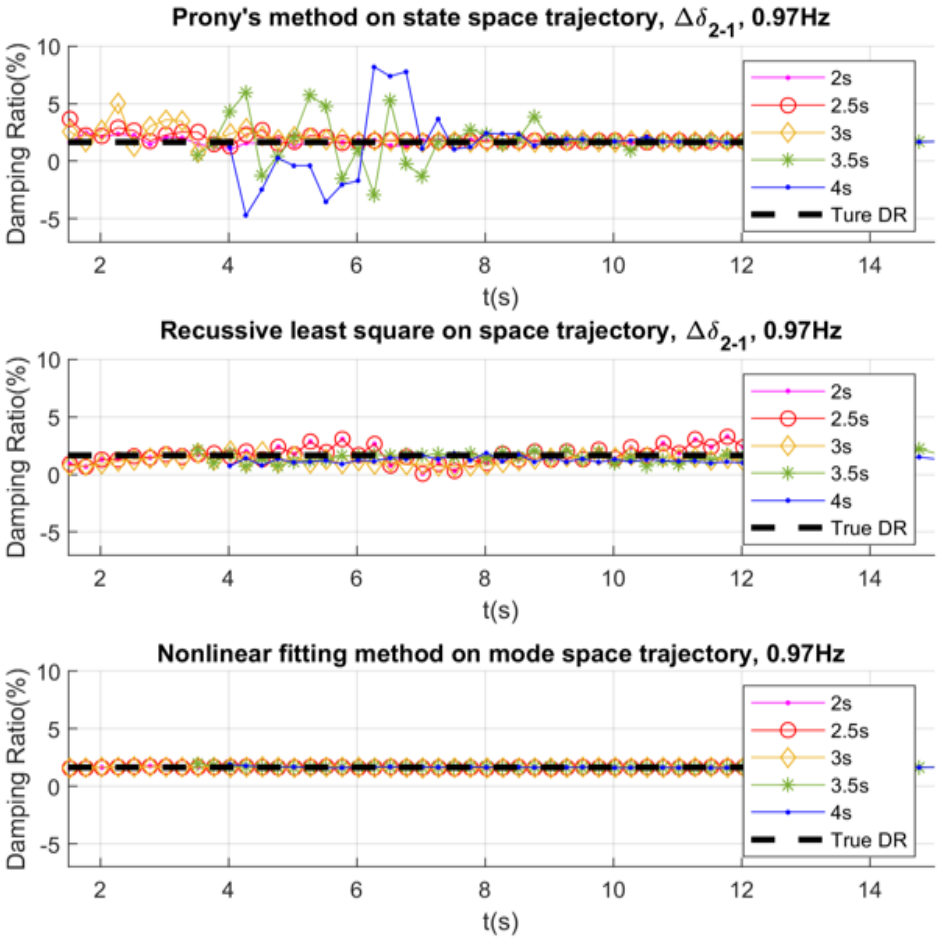

Figure 34. Comparison of different methods on the IEEE 9-bus system.

A.3 Case Study: NPCC 140-Bus System

The NPCC system has 27 of 48 generators modeled by detailed 4th order generator models with exciters [55] and is used as a more realistic scenario to illustrate the validity of the proposed approach. The sampling rate is 30 samples per second.

A temporary three-phase fault is added at bus 13 and cleared after a duration of (a) CCT, (b) 0.5 CCT, and (c) 0.25 CCT, respectively, without disconnecting any line. An oscillation mode at around 0.60 Hz is selected for damping estimation, which is a critical inter-area mode as shown in Figure 17.

Its mode shape indicates the partition of generators into two groups [69]. The dominance of the 0.60 Hz mode can also be verified by the spectrums from the responses of five rotor angles relative to generator 1, as in Figure 35. The information related to this dominant mode from linearized model based small signal analysis is given in Table 13.

Different lengths of the sliding time window as 3 s, 3.5 s, 4 s, 4.5 s, and 5 s are selected. L=30 is selected for the nonlinear oscillator model. The Prony's and RLS methods are performed on the rotor angle difference between generators 29 and 5, since the 0.60Hz mode is highly observable from the measurements of δ_{29} and δ_5, and δ_{29} and δ_5 are nearly out-of-phase. The results with fault durations of (a) CCT, (b) 0.5 CCT, and (c) 0.25 CCT are shown in Figure 36, Figure 37 and Figure 38, respectively. The length of the sliding time window. Therefore, the proposed approach can also be applied to a large power system if its model is provided.

Note that when the fault is cleared at CCT, the system nonlinearity is significantly excited and the result of the proposed approach in Figure 36 deviates away from the true

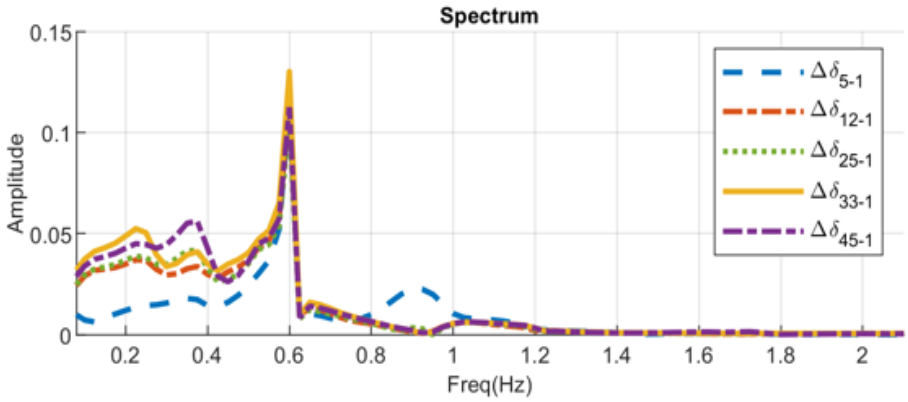

Figure 35. NPCC 140-bus system: Spectrums when the fault is cleared at CCT.

Table 13. Dominant Mode of NPCC 140-bus System

Frequency (Hz)	Eigenvalue	Damping ratio (%)
0.60	-0.037 $\pm$ 3.807i	0.983

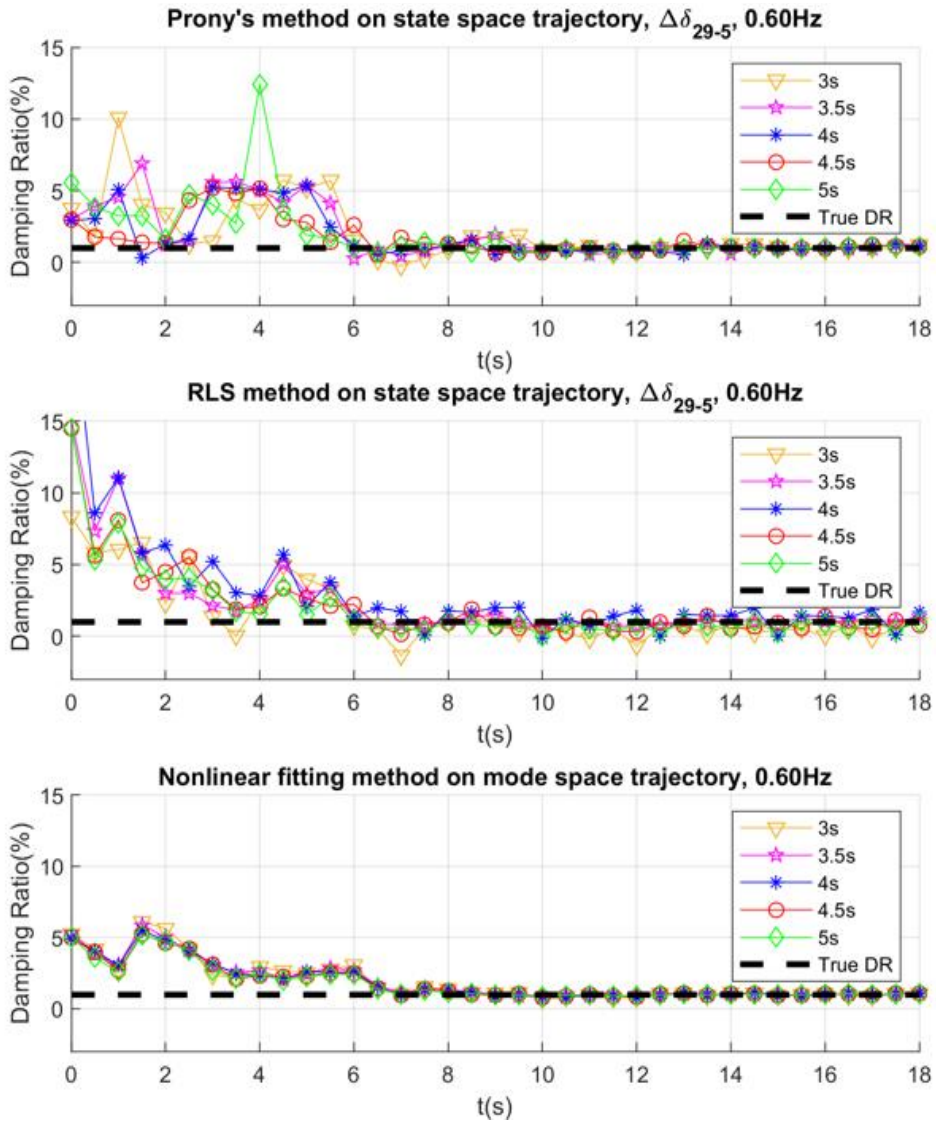

Figure 36. Comparison of different methods on the NPCC system with a fault cleared at CCT.

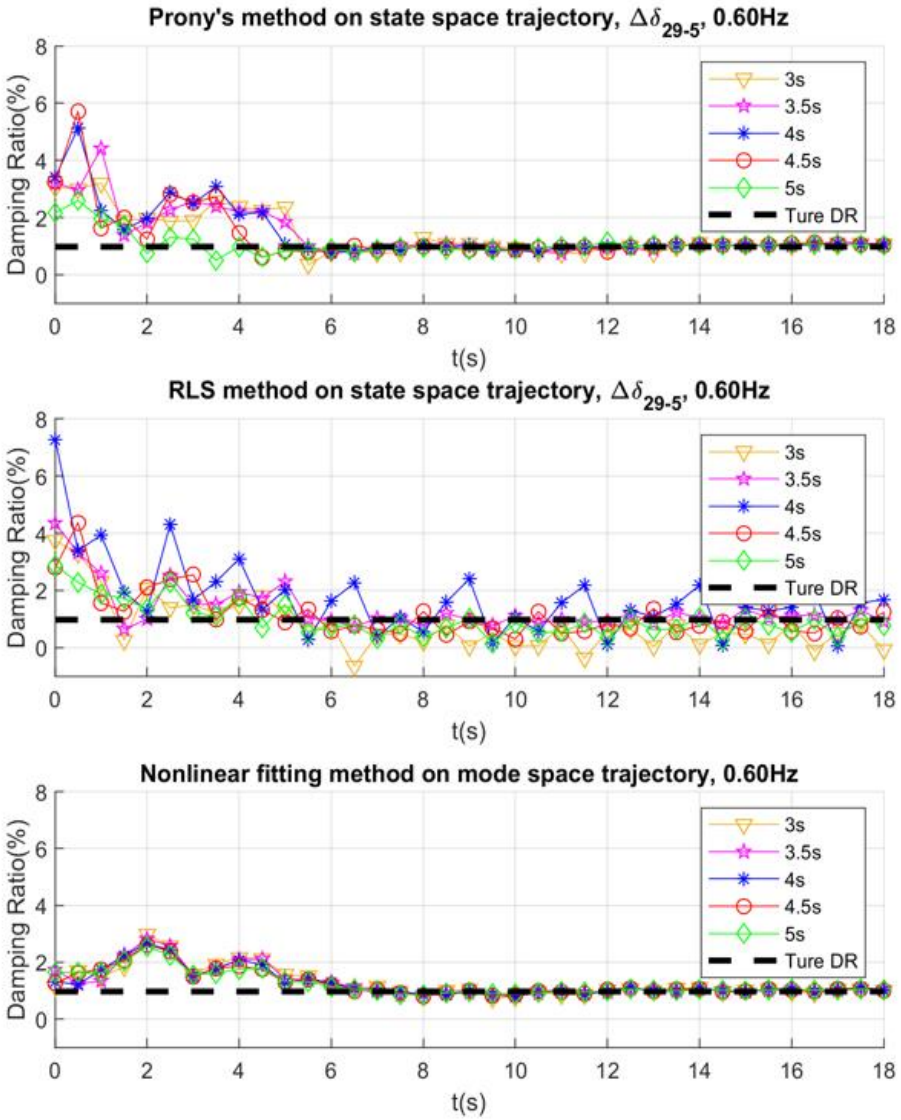

Figure 37. Comparison of different methods on the NPCC system with a fault cleared at 0.5×CCT.

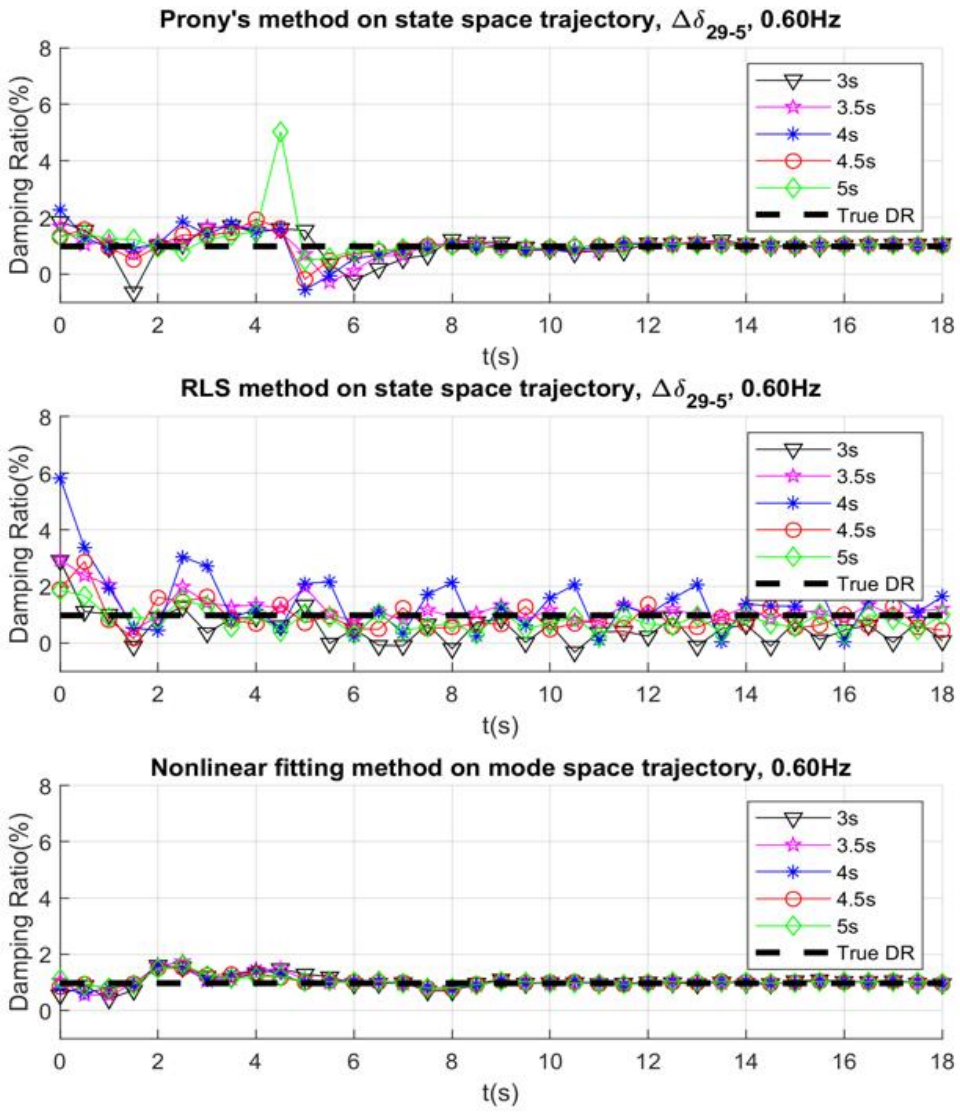

Figure 38. Comparison of different methods on the NPCC system with a fault cleared at 0.25×CCT.

proposed approach is much more robust than the Prony's and RLS methods. Moreover, the proposed approach can give more consistent damping estimation regardless of the damping ratio during the first 7 seconds. This phenomenon indicates that the proposed approach can obtain the "True DR" with the system nonlinearity manifested up to some extent. Therefore, there exists an accuracy region for the proposed approach in the state space, within which the proposed approach can provide a high-accuracy estimation. However, investigating the accuracy region is difficult and computationally intensive due to the high-dimensionality nature of the original state space. Instead, an indicator is defined in this paper to evaluate how close the estimation result is to the "True DR".

The experimental result shows that, when the estimation from the proposed approach is not close to the 'True DR', the coefficient of the 4th order term, c_4 in (2-8), is usually ten times larger than the coefficient of the 3rd order terms, c_3; otherwise, c_4 usually stays small. This indicates that the proposed approach might encounter considerable errors when the 4th or higher order monomials become unneglectable. Moreover, the post-fault trajectory shows more nonlinearity when the initial value is close to the stability boundary. Hence, an indicator is defined as (A-6) via the rotor angles and the type-1 UEP (unstable equilibrium point) whose unstable manifold would be intersected by the fault-on trajectory if the fault sustains. The type-1 controlling UEP is used since it characterizes the portion of the stability boundary near the fault-on trajectory [70]. It could be obtained by using the BCU method [71]. For the sake of convenience, in this paper, it is alternatively approximated by the point in the first swing

of the post-fault trajectory where the generators have the least rotor speed difference, since at the UEP the rotor speed difference among the generators should be zero.

$$Ind = \left\| \frac{\Delta\delta}{d_{uep}} \right\|^4 \tag{A-6}$$

where d_{uep} is the distance between the type-1 UEP and SEP; $\| \cdot \|$ is the operator to solve the 2-norm.

When Ind is smaller than a certain threshold, the nonlinearity caused by 4th and higher order terms are considered ignorable or limited. Based on the experimental results, it is suggested to set the threshold as 0.02, or equivalently $\|\Delta\delta/d_{UEP}\| < 0.376$, to obtain a good estimation of the accuracy region of the proposed approach. As shown Figure 39, the variation of $\|\Delta\delta/d_{UEP}\|$ is less than the threshold 0.376 after 7 seconds, after which the estimation become more close to the "True DR" as shown in Figure 36.

To investigate the phenomenon that the estimated damping ratio deviates from the 'True DR' during the first 7 seconds in , i.e. CCT case, the mode 'angle' $\Delta\delta_{zi}$ of the 0.60 Hz mode is investigated, of which the time series is shown in Figure 40. The two envelopes (in red) of the time series (in blue) tend to converge in a fast pace before the 7 seconds, while in a low pace afterwards. This shows that the 0.60 Hz mode undergoes a fast damped out process during the early transient stage where system nonlinearity is largely excited. This property could motivate a new type of stabilization control methods which not only consider the linear system responses, but also consider the nonlinear system responses to some extent. This will be investigated in the future works.

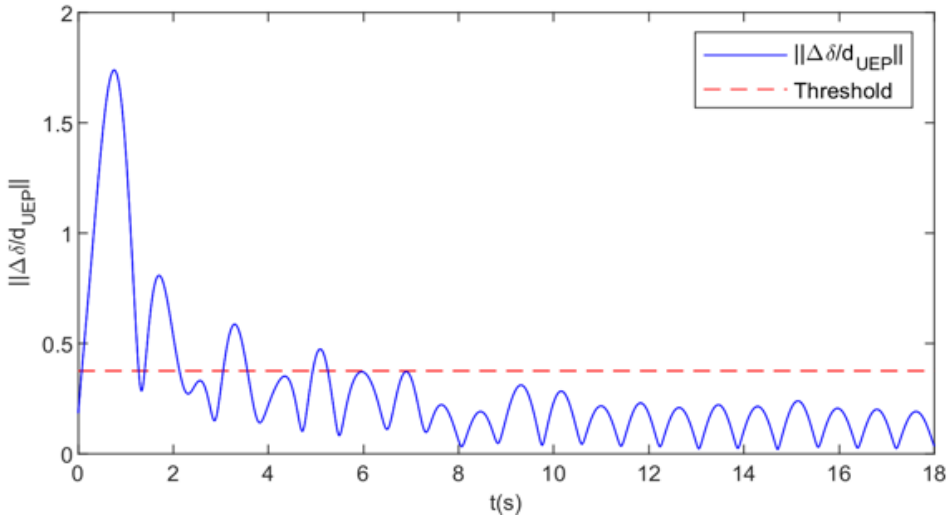

Figure 39. Variation of $||\Delta\delta/d_{uep}||$.

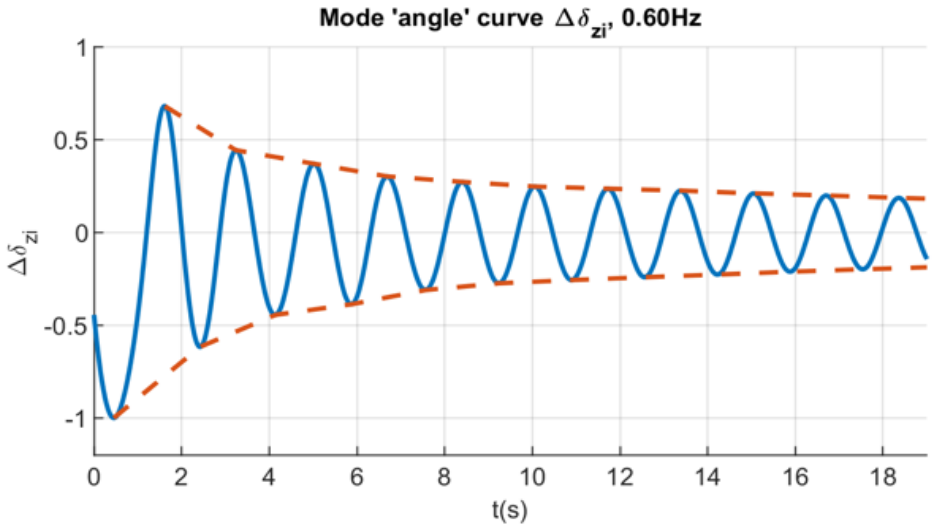

Figure 40. Mode 'angle' curve $\Delta\delta_{zi}$ of the 0.60 Hz mode.

A.4 Case Study: Three Factors

Influences of the aforementioned three factors on damping estimation are investigated on the NPCC 140-bus system.

Measurement Noises

Assume that the time series of rotor angle δ of the previous case contain a Gaussian noise with a variance of 0.005. Without screening out the noise, the proposed approach even cannot give an acceptable result. Then, the designed filter is applied to screen out the noise, and the proposed approach is applied to the filtered time series of rotor angles over a 5 seconds sliding time window. The estimation result is compared with that of "No noise" scenario, as illustrated in Figure 41. The comparison shows that with the designed filter, the damping estimation result is close to that with no noise.

Limited Coverage of PMU Measurements

The limited coverage of PMU measurements could influence the accuracy of damping estimation. Moreover, if the unavailable PMU measurements are from those generators with high observability of the dominant mode, it could have more severe influence on the accuracy of damping estimation. For the NPCC system, the 0.60 Hz mode is highly observable from generators 5, 28, and 29 based on their mode shapes. The accessibility of their PMU measurements is of great interests.

Consider three scenarios:

Scenario 1: the PMU measurements from 41 generators are available (85% coverage), and the PMU measurements for generators 5, 28 and 29 are not available;

Scenario 2: the PMU measurements from 41 generators are available, (85% coverage), and the PMU measurements for generators 5, 28 and 29 are available;

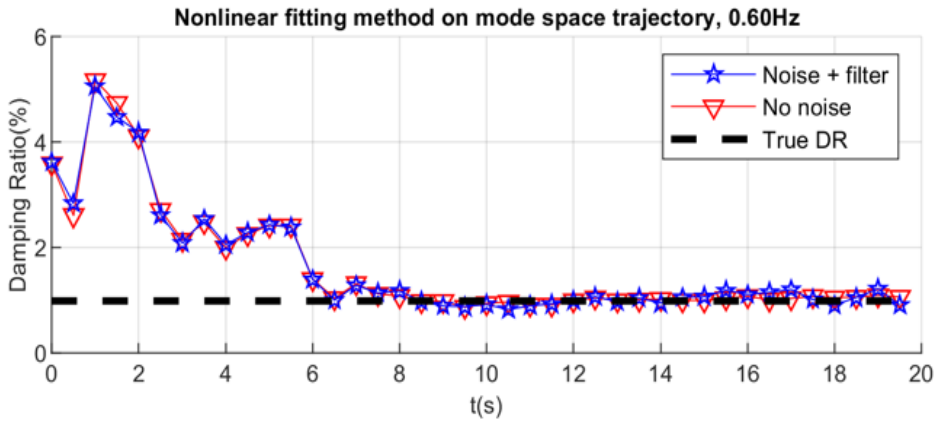

Figure 41. Damping ratio estimation with noise in time series.

Scenario 3: the PMU measurements for all the 48 generators are available (100% coverage).

The estimation results for the above three scenarios are compared in Figure 42. The results in Figure 42 shows that, if the measurements on those generators with high observability of the dominant mode are not available, the estimation accuracy will be worsen, as the comparison between **Scenario 1** and **Scenario 3**; otherwise, the estimation result would still remain accurate, as the comparison between **Scenario 2** and **Scenario 3**. Therefore, if a dominant mode is specified to be monitored during system oscillation, it is strongly recommended to guarantee the accessibility of PMU measurements on the generators which have high observability of that dominant mode in order to ensure the accuracy of damping estimation.

Scenario with Two Dominant Modes

In this subsection, a scenario with two dominant modes, the 0.46 Hz and 0.60 Hz modes, co-existing are studied. The two modes are intentionally excited using the linearly scaled mode shape (LSMS) technique introduced in [25]. The response of the relative rotor angles is given in Figure 43. The proposed approach is applied using a 5 seconds sliding time window. The modal energy ratio defined in (A-5) are calculated for both modes.

The estimated damping ratios and modal energy ratios of two modes are shown in Figure 44. During the early transient period of the first few seconds, the 0.46 Hz mode is more dominant since it has the highest energy ratio among all oscillation modes. The damping ratio estimation is more accurate for the 0.46 Hz mode than for the 0.60 Hz mode. Then, at 5.6 seconds, the 0.60 Hz mode raises its modal energy ratio to be the

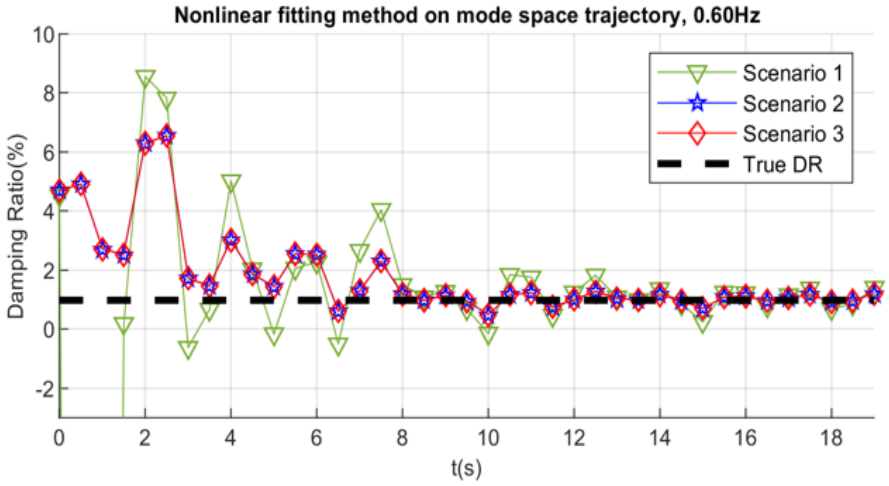

Figure 42. Damping ratio estimation with limited coverage of PMU measurements.

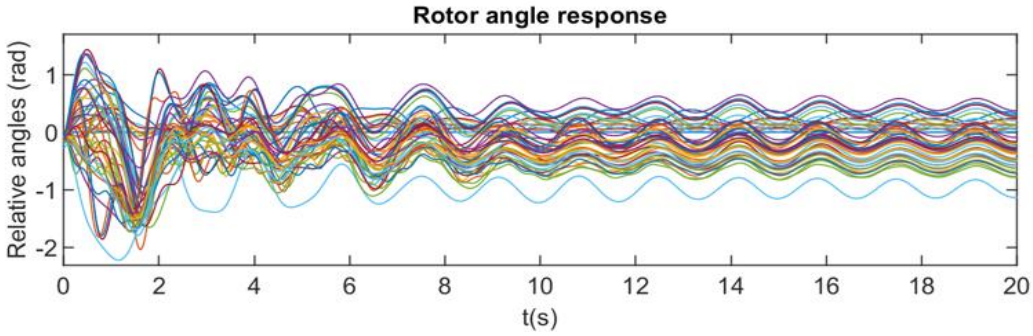

Figure 43. Rotor angle response.

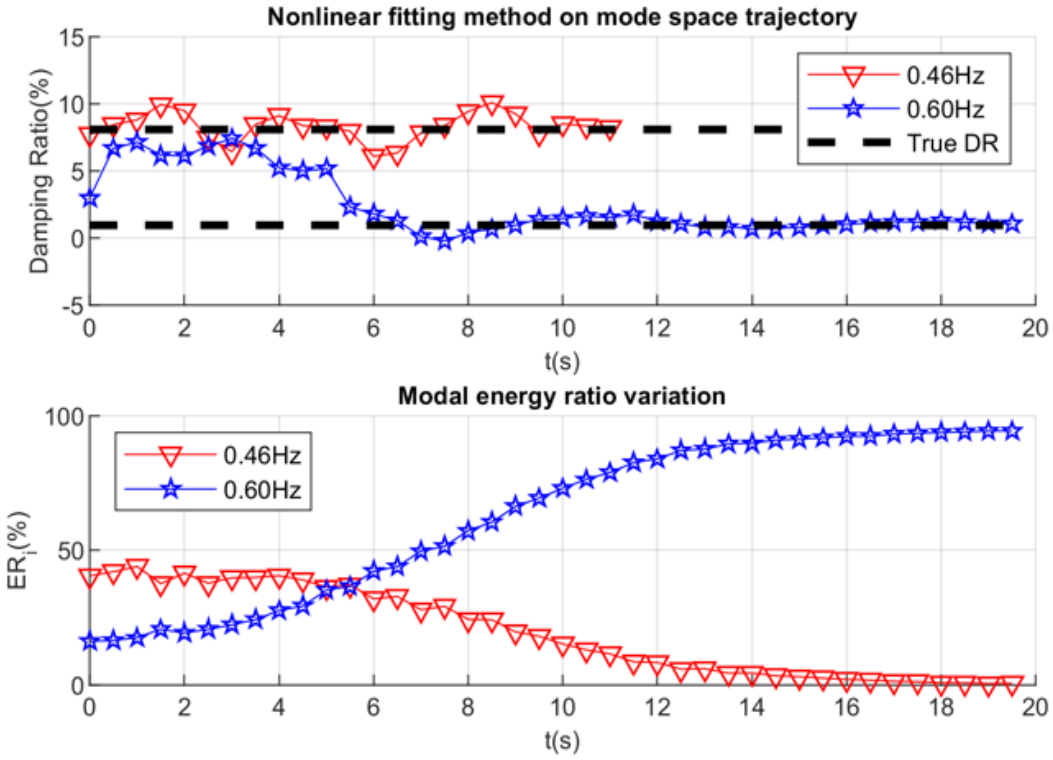

Figure 44. Damping ratio estimation and modal energy ratio variation.

same as the 0.46 Hz mode, and then becomes more dominant. Thereafter, the damping ratio of the 0.60Hz mode becomes more accurate while the 0.46 Hz is quickly damped with its modal energy ratio decreasing to <10% after t = 11 s, at which its damping estimation is terminated as in Figure 44.

From the analysis above, it shows that the proposed approach can give more accurate damping estimation for a more dominant mode in terms of the defined modal energy ratio, which could be used to determine the most dominant mode in online applications and as an indicator on if the damping estimation using the proposed approach is accurate. The energy ratio could also be utilized for designing TSA and control methods, which would be investigated in the future.

APPENDIX B – The Response of A Linear One-Degree-of-Freedom System to Principal Parametric Resonance

B.1 Problem Formulation and Method of Multiple Scales

Consider a linear 1-degree-of-freedom (1DOF) oscillator (B-1).

$$\ddot{x} + (2\zeta\omega_n + K\cos(\Omega t))\dot{x} + \omega_n^2 x = 0 \tag{B-1}$$

where x is the state. ζ and ω_n are the damping ratio and natural frequency of the oscillator, respectively. K and Ω are the amplitude and frequency of a periodic parameter $K\cos(\Omega t)$. Without the periodic parameter, the eigenvalue λ and the oscillation frequency f of the oscillator is calculated by:

$$\lambda_{1,2} = \sigma \pm jw = -\zeta\omega_n \pm j\omega_n\sqrt{1-\zeta^2}, \qquad f = \frac{w}{2\pi} \tag{B-2}$$

When $\Omega \approx 2w$, the principal parametric resonance can be observed in the response of x. For instance, let ζ = 0.0098, ω_n = 3.8072 rad/s, K = 0.5, and consequently, w = 3.8070 rad/s and f = 0.6059 Hz. Then, if let Ω = 6.9115 rad/s and let the initial value be [x, $\dot{x}$] = [1, 0], the response of x is shown in Figure 45 with the envelop being marked and the measured damping ratio is given in Figure 46. The periodic change in the measured damping ratio shows the parametric resonance due to $\Omega \approx 2w$.

The resonance can be investigated by finding an asymptotic solution via the method of multiple scales (MMS) for (B-1), through which some properties could be revealed. The basic idea of MMS is to find an asymptotic solution of a perturbed system considering different time scales. The use of MMS follows the methodology in [72]-[74].

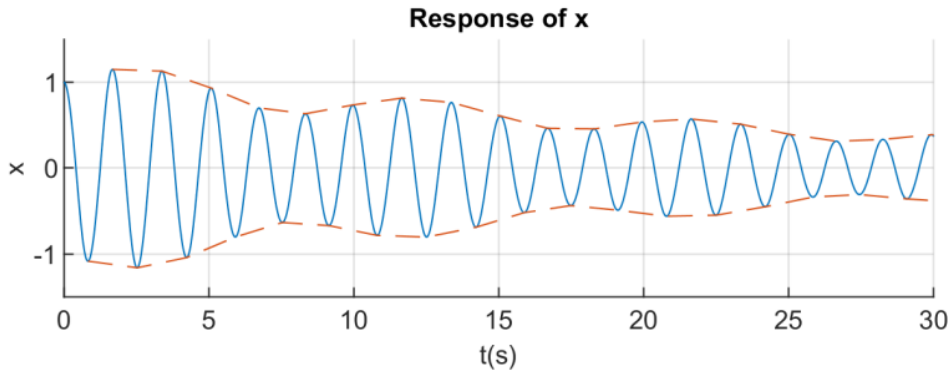

Figure 45. Principal parameter resonance: response of *x*

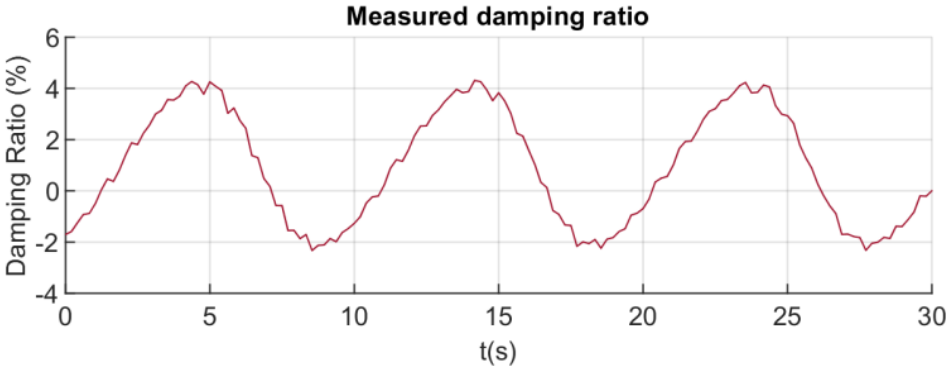

Figure 46. Principal parameter resonance: measured damping ratio

First, the periodic parameter $K\cos(\Omega t)$ is treated as a perturbation by inserting a small dimensionless parameter $\varepsilon > 0$ like in (B-3), where $K_\varepsilon = K/\varepsilon$.

$$\ddot{x} + (2\zeta\omega_n + \varepsilon K_\varepsilon \cos(\Omega t))\dot{x} + \omega_n^2 x = 0 \tag{B-3}$$

Then, a first order uniform solution of (B-3) is sought in the form of (B-4):

$$x(\varepsilon, T_0, T_1) = x_0(T_0, T_1) + \varepsilon x_1(T_0, T_1) + \ldots \tag{B-4}$$

$$T_0 = t, \qquad T_1 = \varepsilon t \tag{B-5}$$

where T_1 is introduced as a slow-scale time variable, such that (B-4) could consider the evolution of the solution over long time-scales of the order ε^{-1}. Note that x_0 is exactly the solution of (B-1) when $\varepsilon = 0$, and x_1 is the part caused by the perturbation. Substitute (B-4) into (B-3) and equate the coefficients of like powers of ε:

$$D_0^2 x_0 + 2\zeta\omega_n D_0 x_0 + \omega_n^2 x_0 = 0 \tag{B-6}$$

$$D_0^2 x_1 + 2\zeta\omega_n D_0 x_1 + \omega_n^2 x_1 = -2D_1 D_0 x_0 - K_\varepsilon \cos(\Omega T_0) D_0 x_0 - 2\zeta\omega_n D_1 x_0 \tag{B-7}$$

where $D_n = \partial/\partial T_n$.

The solution of (B-6) can be expressed in a complex form:

$$x_0(T_0, T_1) = A(T_1)e^{(\sigma + jw)T_0} + \bar{A}(T_1)e^{(\sigma - jw)T_0} \tag{B-8}$$

where the bar symbol denotes the conjugate. Substitute (B-8) into (B-7):

$$\begin{aligned} &D_0^2 x_1 + 2\zeta\omega_n D_0 x_1 + \omega_n^2 x_1 = \\ &\quad -2(\sigma + jw)e^{(\sigma + jw)T_0} D_1 A - 2\zeta\omega_n e^{(\sigma + jw)T_0} D_1 A \\ &\quad -\frac{K_\varepsilon}{2}\left[(\sigma + jw)e^{(\sigma + j(\Omega + w))T_0} A + (\sigma - jw)e^{(\sigma + j(\Omega - w))T_0} \bar{A}\right] + C.C. \end{aligned} \tag{B-9}$$

where *C.C.* denotes the complex conjugate of the former. If introduce a detuning parameter ξ such that $\Omega = 2w + \varepsilon\xi$, (B-9) can be converted to:

$$D_0^2 x_1 + 2\zeta\omega_n D_0 x_1 + \omega_n^2 x_1 = -\left[2(\sigma + jw) D_1 A + 2\zeta\omega_n D_1 A + \frac{K_\varepsilon}{2}(\sigma - jw) e^{j\varepsilon\xi T_0} \bar{A} \right] e^{(\sigma + jw)T_0} - \frac{K_\varepsilon}{2}(\sigma + jw) e^{(\sigma + j(\Omega + w))T_0} A + C.C. \quad \text{(B-10)}$$

It can be verified that the condition (B-11) should be met to avoid generating secular terms in the solution of *x*. The explanation of secular term can be found in [74]. In this problem it will be a term grows linearly in *t*, such that the identified solution will be unbounded, while in fact the true solution is bounded.

$$2(\sigma + jw) D_1 A + 2\zeta\omega_n D_1 A + \frac{K_\varepsilon}{2}(\sigma - jw) e^{j\varepsilon\xi T_0} \bar{A} = 0 \quad \text{(B-11)}$$

With the condition (B-11), the solution of (B-10) is given below.

$$x_1(T_0, T_1) = \frac{K_\varepsilon (\sigma + jw) A}{2} \left(\frac{e^{(\sigma + j(\Omega + w))T_0}}{\Omega(\Omega + 2w)} + \frac{e^{(\sigma - jw)T_0}}{2w(\Omega + 2w)} - \frac{e^{(\sigma + jw)T_0}}{2w\Omega} \right) + C.C. \quad \text{(B-12)}$$

x_1 could be ignored compared to x_0, since usually it is numerically small. Hence, assume $x(t) \approx x_0(t)$. $A(T_1)$ can be determined by solving (B-11). In the weakly-damped case, σ can be assumed to be zero and (B-11) can be converted to:

$$\frac{dA}{dT_1} = \frac{K_\varepsilon}{4} e^{j\varepsilon\xi T_1} \bar{A} \quad \text{(B-13)}$$

The analytical solutions of $A(T_1)$ and $x(t)$ can be found for three cases, *a*) $(\Omega - 2w)^2 - K^2/4 > 0$, *b*) $(\Omega - 2w)^2 - K^2/4 < 0$, and *c*) $(\Omega - 2w)^2 - K^2/4 = 0$. For the sake of convenience, define $w_K = \sqrt{\left|\xi^2 - K_\varepsilon^2/4\right|} = \sqrt{\left|(\Omega - 2w)^2 - K^2/4\right|}\Big/\varepsilon$, and let $A_0 = A_{re0} + jA_{im0}$ be the given initial value of $A(T_1)$.

B.2 $(\Omega - 2w)^2 - K^2/4 > 0$

The solution of $A(T_1)$ is:

$$A(T_1) = (C_1 e^{j(r_1 - w_K T_1)} + C_2 e^{jr_2}) e^{j\frac{\xi + w_K}{2} T_1} \tag{B-14}$$

$$\begin{cases} C_1 = \sqrt{\dfrac{\xi + w_K}{2w_K^2}} \sqrt{\xi(A_{re0}^2 + A_{im0}^2) + K_\varepsilon A_{re0} A_{im0}} \\ C_2 = -\sqrt{\dfrac{\xi - w_K}{2w_K^2}} \sqrt{\xi(A_{re0}^2 + A_{im0}^2) + K_\varepsilon A_{re0} A_{im0}} \\ r_1 = \arctan\left(\dfrac{2A_{im0}(\xi + w_K) + K_\varepsilon A_{re0}}{2A_{re0}(\xi + w_K) + K_\varepsilon A_{im0}} \right) \\ r_2 = \arctan\left(\dfrac{2A_{im0}(\xi - w_K) + KA_{re0}}{2A_{re0}(\xi - w_K) + KA_{im0}} \right) \end{cases} \tag{B-15}$$

The solution of $x(t)$ is obtained by substituting (B-14) and (B-5) into (B-4):

$$x(t) = 2C_1 e^{\sigma t} \cos(w_C t + r_1 - \varepsilon w_K t) + 2C_2 e^{\sigma t} \cos(w_C t + r_2) \tag{B-16}$$

$$w_C = w + \frac{\xi + w_K}{2} \varepsilon \tag{B-17}$$

The resulting $x(t)$ consists of two components. The magnitude of the first component is $2C_1$ and the frequency is $w_C - \varepsilon w_K$. The magnitude of the second component is $2C_2$ and the frequency is w_C. The validity of the approximated solution can be visualized by the case when $\Omega = 6.9115$ rad/s. The comparison of the true response of $x(t)$ and the approximated $x(t)$ from MMS is shown in Figure 47. The approximated $x(t)$ is almost the same at the true response.

The principal parametric resonance in this case can be interpreted as follows. Without loss of generality, only consider the case when C_2 is larger than C_1. The second component can be more dominant than the first component. Since εw_K is much smaller than w_C, the term $\varepsilon w_K t$ can be viewed as a slow change of phase of the first component. Then, the change of damping of $x(t)$ can be interpreted as the periodically phase shift between the two components. When $r_1 - \varepsilon w_K t \approx r_2 + 2m\pi$, $m = 0, \pm 1, \pm 2, \ldots$, the two

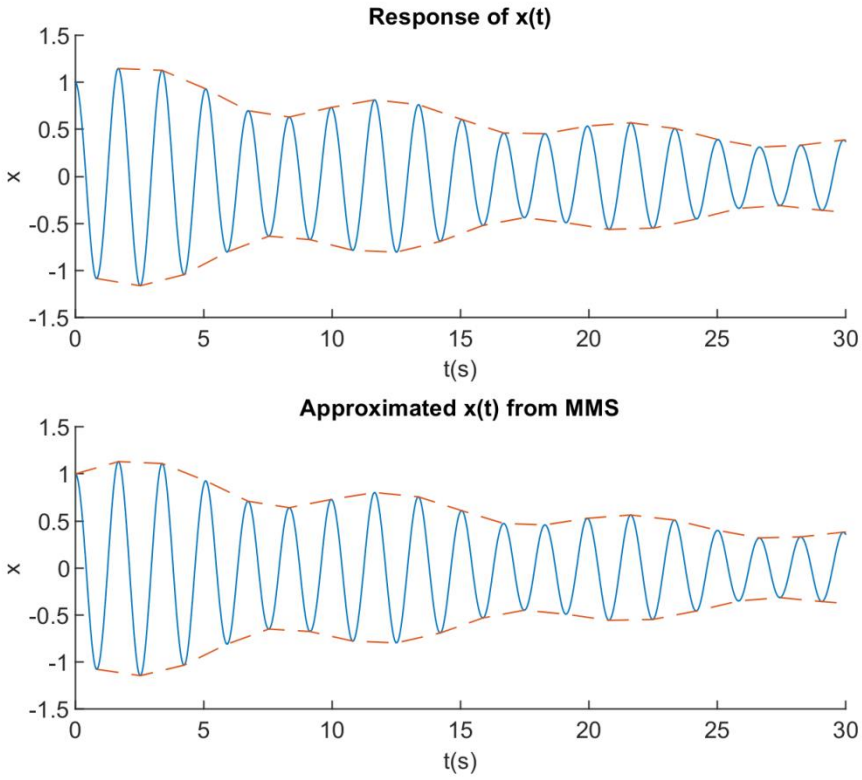

Figure 47. Comparison of true response and approximated solution: $(\Omega-2w)^2-K^2/4 > 0$.

components are in-phase and the magnitude of $x(t)$ is amplified. When $r_1 - \varepsilon w_K t \approx r_2 + 2m\pi + \pi$, $m = 0, \pm1, \pm2, \ldots$, the two components are out-of-phase and the magnitude of $x(t)$ is reduced. This change is periodic and the frequency of such periodicity is $\varepsilon w_K = \sqrt{(\Omega - 2w)^2 - K^2/4}$, and it makes the response of $x(t)$ to exhibit a periodically changed damping.

B.3 $(\Omega - 2w)^2 - K^2/4 < 0$

The solution of $A(T_1)$ is:

$$A(T_1) = (C_3 e^{jr_3} + C_4 e^{j(r_4 - w_K T_1)}) e^{j\frac{\xi + w_K}{2} T_1} \tag{B-18}$$

$$\begin{cases} C_3 = \sqrt{\dfrac{K_\varepsilon (2K_\varepsilon + w_K)}{w_K^2}} \left| A_{re0} + A_{im0} \dfrac{2\xi}{K_\varepsilon + 2w_K} \right| \\ C_4 = \sqrt{\dfrac{K_\varepsilon (2K_\varepsilon - w_K)}{w_K^2}} \left| A_{re0} + A_{im0} \dfrac{2\xi}{K_\varepsilon - 2w_K} \right| \\ r_3 = \arctan\left(\dfrac{-A_{im0}(K_\varepsilon - 2w_K) - 2\xi A_{re0}}{A_{re0}(K_\varepsilon + 2w_K) + 2\xi A_{im0}} \right) \\ r_4 = \arctan\left(\dfrac{A_{im0}(K_\varepsilon + 2w_K) + 2\xi A_{re0}}{-A_{re0}(K_\varepsilon - 2w_K) - 2\xi A_{im0}} \right) \end{cases} \tag{B-19}$$

The solution of $x(t)$ is obtained by substituting (B-18) and (B-5) into (B-4):

$$x(t) = 2C_3 e^{\left(\sigma + \varepsilon \frac{w_K}{2}\right)t} \cos\left((w + \frac{\Omega}{2})t + r_3 \right) + 2C_4 e^{\left(\sigma - \varepsilon \frac{w_K}{2}\right)t} \cos\left((w + \frac{\Omega}{2})t + r_4 \right) \tag{B-20}$$

The resulting $x(t)$ consists of two components. The magnitude of the first component is $2C_3$ and the magnitude of the second component is $2C_4$. The frequency of both components is $w + \Omega/2$. The two components of $x(t)$ have damping coefficient different from σ. This validity of the approximated solution can be verified by the case when Ω is changed to 7.5524 rad/s. The comparison of the true response of $x(t)$ and the approximated $x(t)$ from MMS is shown in Figure 48. The approximated $x(t)$ is almost the

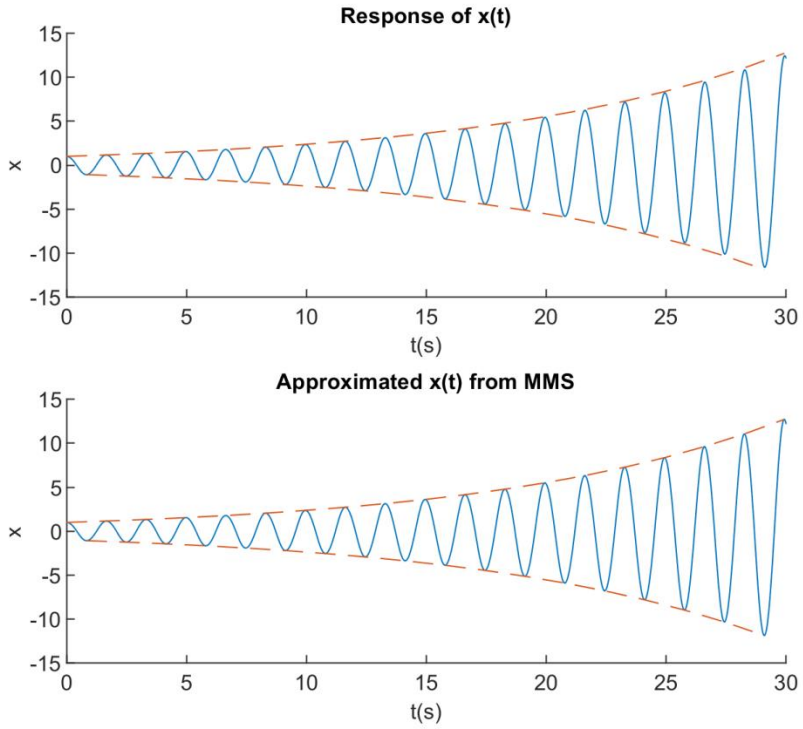

Figure 48. Comparison of true response and approximated solution: $(\Omega-2w)^2-K^2/4 < 0$.

same at the true response. Note that the response diverges since the damping part of the first component becomes positive.

In this case, the response of $x(t)$ will not exhibit a periodically changed damping, but might exhibit a time-variant damping. If C_3 is much larger than C_4, the first component will be dominant at the early stage and the response of $x(t)$ will be damped in a fast pace. Then, the first component will take the dominance after the second component is damped out, and the response of $x(t)$ will be damped in a slow pace.

B.4 $(\Omega-2w)^2-K^2/4 = 0$

The solution of $A(T_1)$ is:

$$A(T_1) = A_0 e^{jK_\varepsilon T_1} + K_\varepsilon(\bar{A}_0 - jA_0)T_1 e^{jK_\varepsilon T_1} \tag{B-21}$$

The solution of $x(t)$ is obtained by substituting (B-21) and (B-5) into (B-4):

$$x(t) = 2C_5 e^{\sigma t}\cos\left((w+\frac{\Omega}{2})t + r_5\right) + 2C_6 t e^{\sigma t}\cos\left((w+\frac{\Omega}{2})t + r_6\right) \tag{B-22}$$

$$\begin{cases} C_5 e^{jr_5} = A_0 \\ C_6 e^{jr6} = K_\varepsilon(\bar{A}_0 - jA_0) \end{cases} \tag{B-23}$$

The resulting $x(t)$ consists of two components. The magnitude of the first component is $2C_5$ and the magnitude of the second component is $2C_6$. The frequency of both components is $w + \Omega/2$. Note the second component also depends on t, which may cause a time-variant damping.

This validity of the approximated solution can be verified by the case when Ω is changed to 7.3639 rad/s. The comparison of the true response of $x(t)$ and the approximated $x(t)$ from MMS is shown in Figure 49. The approximated $x(t)$ is almost the same at the true response.

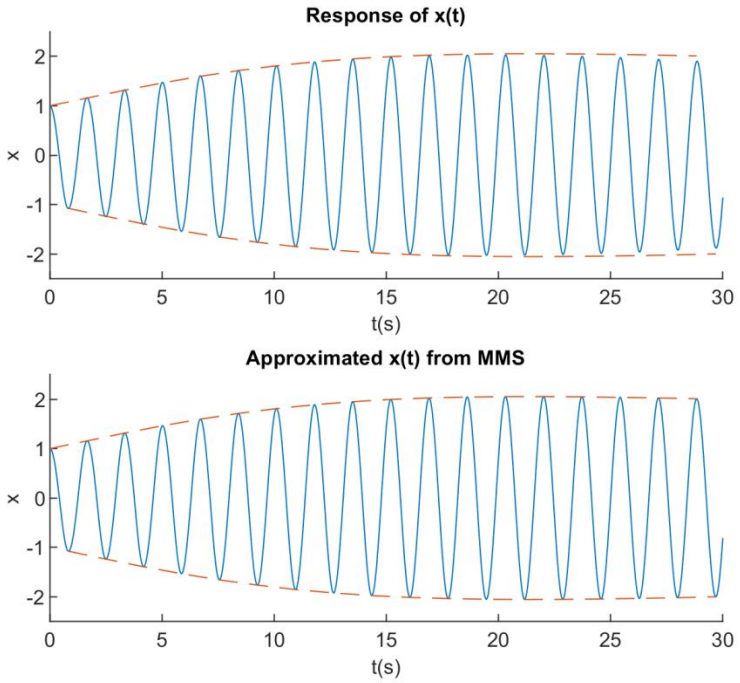

Figure 49. Comparison of true response and approximated solution: $(\Omega-2w)^2-K^2/4 = 0$.

Since the condition $(\Omega–2w)^2–K^2/4 = 0$ can hardly be met, this case is usually ignored for the industrial applications.

B.5 Summary

The principal parametric resonance in (B-1) can be classified into three cases depending on $(\Omega–2w)^2–K^2/4$. When $(\Omega–2w)^2–K^2/4 > 0$, periodically changed damping could appear in the response of x(t), and the frequency of this periodicity is close to $\sqrt{\left|(\Omega-2w)^2-K^2/4\right|}$. When $(\Omega–2w)^2–K^2/4 \leq 0$, it is a time-variant damping.

APPENDIX C – The Response of A Linear One-Degree-of-Freedom System to "Zeroth-Order" Parametric Resonance

Consider the same system as in (B-1). When $\Omega \approx 0$, parametric resonance can be observed in the response of x, which is named as "zeroth-order" parametric resonance here. For instance, let ζ = 0.0098, ω_n = 3.8072 rad/s, K = 0.5, and consequently, w = 3.8070 rad/s and f = 0.6059 Hz. Then, if let Ω = 0.6283 rad/s and let the initial value be [x, $\dot{x}$] = [1, 0], the response is shown in Figure 50 with the envelop being marked and the measured damping ratio is shown in Figure 51. The periodic change in the measured damping ratio shows the parametric resonance due to $\Omega \approx 0$.

Through MMS, some properties of such resonance could also be revealed. Again, consider a small dimensionless parameter ε like in (B-3), and take the same derivation as from (B-3) to (B-9). By introducing a detuning parameter ξ such that $\Omega = \varepsilon\xi$, (B-9) can be converted to (C-1).

$$\begin{aligned} & D_0^2 x_1 + 2\zeta\omega_n D_0 x_1 + \omega_n^2 x_1 = \\ & \quad -\left[2(\sigma + jw) D_1 A + 2\zeta\omega_n D_1 A + \frac{K_\varepsilon}{2}(\sigma + jw) e^{j\varepsilon\xi T_0} A \right] e^{(\sigma + jw)T_0} \\ & \quad -\frac{K_\varepsilon}{2}(\sigma - jw) e^{(\sigma + j(\varepsilon\xi - w))T_0} \bar{A} + C.C. \end{aligned} \tag{C-1}$$

It can be verified that the condition (C-2) should be met to avoid generating secular terms in the solution of x.

$$2(\sigma + jw) D_1 A + 2\zeta\omega_n D_1 A + \frac{K_\varepsilon}{2}(\sigma + jw) e^{j\varepsilon\xi T_0} A = 0 \tag{C-2}$$

Then, the solution of (C-1) is given below.

$$x_1(T_0, T_1) = \frac{K_\varepsilon(\sigma - jw)\bar{A}}{2}\left(\frac{e^{(\sigma + j(\Omega - w))T_0}}{\Omega(\Omega - 2w)} + \frac{e^{(\sigma - jw)T_0}}{2w\Omega} - \frac{e^{(\sigma + jw)T_0}}{2w(2w - \Omega)} \right) + C.C. \tag{C-3}$$

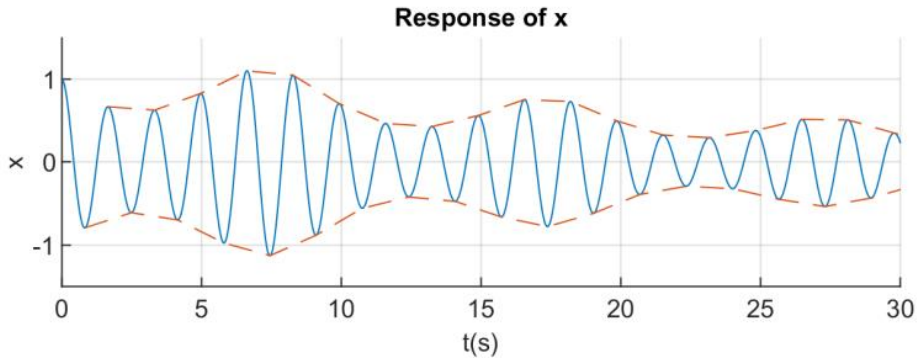

Figure 50. "Zeroth-order" parametric resonance: response of *x*

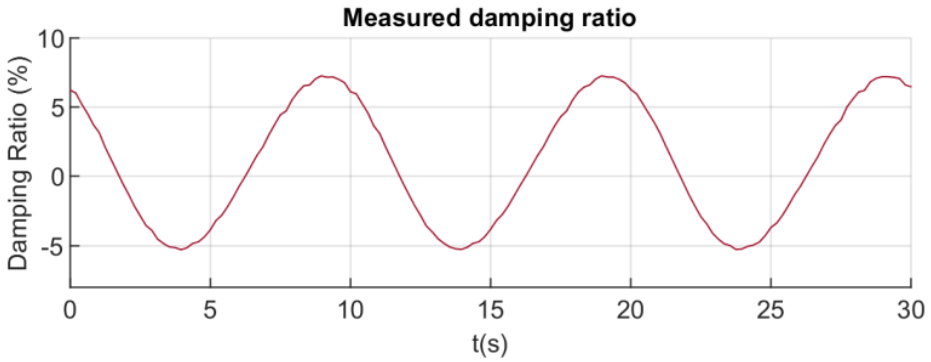

Figure 51. "Zeroth-order" parametric resonance: measured damping ratio

x_1 could be ignored compared to x_0, since usually it is numerically small. Hence, assume $x(t) \approx x_0(t)$. $A(T_1)$ can be determined by solving (C-2). In the weakly-damped case, σ can be assumed to be zero and (C-2) can be converted to (C-4). The analytical solutions of $A(T_1)$ shown in (C-5), where $A_0 = A_{re0} + jA_{im0}$ is the initial value of $A(T_1)$.

$$\frac{dA}{dT_1} = \frac{K_\varepsilon(-w + j\sigma)}{4w} e^{j\xi T_1} A \tag{C-4}$$

$$A(T_1) = e^{\frac{K_\varepsilon(\sigma+jw)}{4\xi w} e^{j\xi T_1}} + A_0 - e^{\frac{K_\varepsilon(\sigma+jw)}{4\xi w}} \tag{C-5}$$

Substitute (C-5) and (B-5) into (B-4) to obtain $x(t)$:

$$\begin{aligned} x(t) = {} & 2e^{\frac{K\omega_n}{4\Omega w}\cos(\Omega t+\theta)+\sigma t} \cos\left(\frac{K\omega_n}{4\Omega w}\sin(\Omega t+\theta) + wt\right) \\ & + 2e^{\sigma t}\left(A_{re0}\cos(wt) - A_{im0}\sin(wt) - e^{\frac{K\sigma}{4\Omega w}}\cos\left(wt + \frac{K}{4\Omega}\right)\right) \end{aligned} \tag{B-6}$$

$$\theta = \arctan(\frac{w}{\sigma}) \tag{B-7}$$

The solution includes two components. Note that the first component has a periodically changed parameter $\cos(\Omega t+\theta)$ being added to the original damping part σt, which could lead to a periodically changed damping in the response of $x(t)$. The $\sin(\Omega t+\theta)$ term in the first component can be viewed as a periodically changed phase of frequency Ω that leads to a periodic phase shift relative to the second component. Hence, the solution $x(t)$ will exhibit periodically changed damping ratio, and the frequency of such periodicity is close to Ω.

This validity of the approximated solution can be verified by the case when Ω is changed to 0.6283 rad/s. The comparison of the true response of $x(t)$ and the

approximated $x(t)$ from MMS is shown in Figure 52. The approximated $x(t)$ is almost the same at the true response.

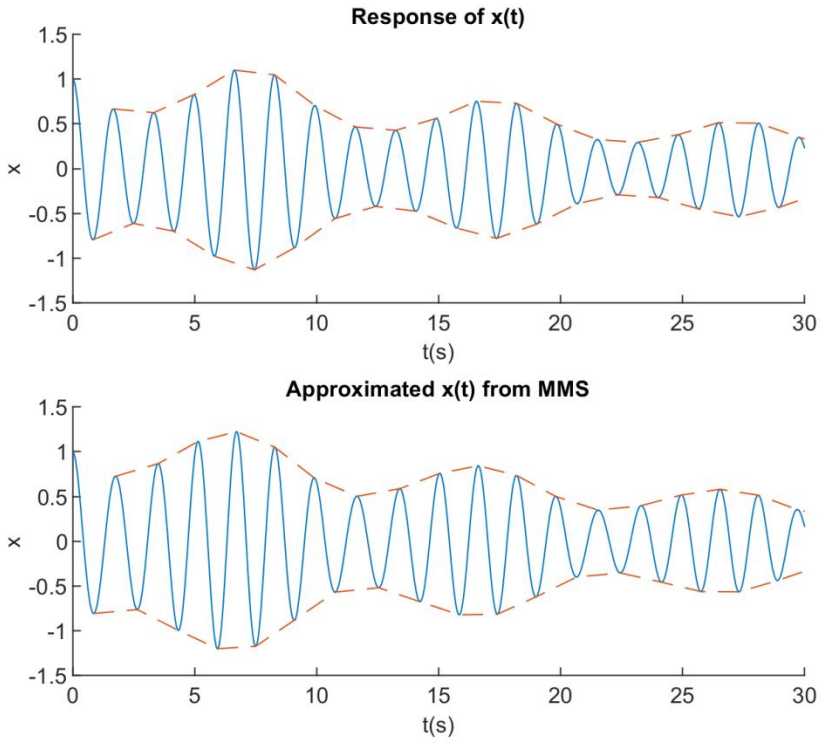

Figure 52. Comparison of true response and approximated solution: “zeroth-order” parameter resonance.

Publications during Ph.D. Study

Journal Papers

[J1] C. Liu, B. Wang, **X. Xu**, K. Sun, D. Shi, C. L. Bak, "A multi-dimensional holomorphic embedding method to solve AC power flows," *IEEE ACCESS*, vol. 5, pp. 25270-25285, Nov. 2017.

[J2] B. Wang, K. Sun, **X. Xu**, "Nonlinear modal decoupling based power system transient stability analysis," *IEEE Trans. Power Syst.*, vol. 34, no. 6, pp. 4889-4899, Jun. 2019.

[J4] Y. Xu, Z. Gu, K. Sun, **X. Xu**, "Understanding a Type of Forced Oscillation Caused by Steam-turbine Governors," *IEEE Trans. Energy Convers.*, vol. 25, no. 3, pp. 1719-1722, Sept. 2020.

[J5] **X. Xu**, W. Jun, B. Wang, K. Sun, "Real-time Damping Estimation on Nonlinear Electromechanical Oscillation," *IEEE Trans. Power Syst.* (Under review).

Conference Papers

[C1] **X. Xu**, C. Liu, K. Sun, "A holomorphic embedding method to solve unstable equilibrium points of power systems," in *Proc. of the 57th IEEE Conference on Decision and Control (CDC)*, Miami, FL, USA, Dec. 2018.

[C2] **X. Xu**, B. Wang and K. Sun, "Initial Study of the Power System Stability Boundary Estimated from Nonlinear Modal Decoupling," 2019 IEEE Milan PowerTech, Milan, Italy, 2019, pp. 1-5.

[C3] B. Wang, **X. Xu**, K. Sun, "Power system transient stability analysis using high-order Taylor expansion systems," *Texas Power and Energy Conference*, College Station, 2019

[C4] **X. Xu**, B. Wang, K. Sun, “Approximation of closest unstable equilibrium points via nonlinear modal decoupling,” 2019 IEEE PES General Meeting, Atlanta, GA, Aug. 2019.

VITA

Xin Xu received the B. S. and M.S. degrees in Electrical Engineering from Shandong University, China, in 2013 and 2016, respectively. He is currently pursuing the Ph.D. degree at the Department of Electrical Engineering and Computer Science, University of Tennessee in Knoxville. His research interests include power system nonlinear dynamics, stability and control.